

NASA/TM-2015-218686



# Numerical Calculations of 3-D High-Lift Flows and Comparison with Experiment

*William B. Compton III*  
*Langley Research Center, Hampton, Virginia*

---

February 2015

## NASA STI Program . . . in Profile

Since its founding, NASA has been dedicated to the advancement of aeronautics and space science. The NASA scientific and technical information (STI) program plays a key part in helping NASA maintain this important role.

The NASA STI program operates under the auspices of the Agency Chief Information Officer. It collects, organizes, provides for archiving, and disseminates NASA's STI. The NASA STI program provides access to the NTRS Registered and its public interface, the NASA Technical Reports Server, thus providing one of the largest collections of aeronautical and space science STI in the world. Results are published in both non-NASA channels and by NASA in the NASA STI Report Series, which includes the following report types:

- **TECHNICAL PUBLICATION.** Reports of completed research or a major significant phase of research that present the results of NASA Programs and include extensive data or theoretical analysis. Includes compilations of significant scientific and technical data and information deemed to be of continuing reference value. NASA counter-part of peer-reviewed formal professional papers but has less stringent limitations on manuscript length and extent of graphic presentations.
- **TECHNICAL MEMORANDUM.** Scientific and technical findings that are preliminary or of specialized interest, e.g., quick release reports, working papers, and bibliographies that contain minimal annotation. Does not contain extensive analysis.
- **CONTRACTOR REPORT.** Scientific and technical findings by NASA-sponsored contractors and grantees.

- **CONFERENCE PUBLICATION.** Collected papers from scientific and technical conferences, symposia, seminars, or other meetings sponsored or co-sponsored by NASA.
- **SPECIAL PUBLICATION.** Scientific, technical, or historical information from NASA programs, projects, and missions, often concerned with subjects having substantial public interest.
- **TECHNICAL TRANSLATION.** English-language translations of foreign scientific and technical material pertinent to NASA's mission.

Specialized services also include organizing and publishing research results, distributing specialized research announcements and feeds, providing information desk and personal search support, and enabling data exchange services.

For more information about the NASA STI program, see the following:

- Access the NASA STI program home page at <http://www.sti.nasa.gov>
- E-mail your question to [help@sti.nasa.gov](mailto:help@sti.nasa.gov)
- Phone the NASA STI Information Desk at 757-864-9658
- Write to:  
NASA STI Information Desk  
Mail Stop 148  
NASA Langley Research Center  
Hampton, VA 23681-2199

NASA/TM-2015-218686



# Numerical Calculations of 3-D High-Lift Flows and Comparison with Experiment

*William B. Compton III*  
*Langley Research Center, Hampton, Virginia*

National Aeronautics and  
Space Administration

Langley Research Center  
Hampton, Virginia 23681-2199

---

February 2015

## Acknowledgments

Many researchers have contributed to this paper. In addition to branch management's advocating for the research, the technical editing committee and others have reviewed the paper for technical errors, and have offered very helpful insights, suggestions, and information. One researcher in particular, Dr. Veer N. Vatsa, the founder of the Navier-Stokes code used for these calculations, stands out and deserves special recognition. Dr. Vatsa very generously spent considerable time and effort in helping to get the code set up and running for this problem, extensively reviewing the paper and making technical corrections to it, and making very useful suggestions. It would have been nearly impossible to complete the work without his help.

The use of trademarks or names of manufacturers in this report is for accurate reporting and does not constitute an official endorsement, either expressed or implied, of such products or manufacturers by the National Aeronautics and Space Administration.

Available from:

NASA STI Program / Mail Stop 148  
NASA Langley Research Center  
Hampton, VA 23681-2199  
Fax: 757-864-6500

## Forward

The high-lift calculations for this paper were made on the NASA Origin Super Computer in the year 2000 to 2004 time frame. Other obligations prevented publishing the results immediately. At the time, the NASA Origin Computer was the most powerful computer at NASA. Since then, other researchers have made high-lift calculations on far more powerful computers, and have advanced the art and science of numerically predicting high lift flows. Still, the high-lift computations of this paper compare to wind-tunnel data at least as well as many of the calculations published at a later date. In addition, many of this study's findings have been corroborated by later research (examples of which will be cited in the discussion). Hence, these calculations have stood the test of time.

This paper is published now to document the work, since it contains a broader analysis (particularly of the flow field) than many other papers, and since it has stood the test of time. Thus this paper adds to the volume of work that sheds light onto, and gives confidence in, the basic technology for solving these types of high-lift flows.

THIS PAGE INTENTIONALLY LEFT BLANK

## Abstract

*Solutions were obtained with the Navier-Stokes CFD code TLNS3D to predict the flow about The NASA Trapezoidal Wing, a high-lift wing composed of three elements: the main-wing element, a deployed leading-edge slat, and a deployed trailing-edge flap. Turbulence was modeled by the Spalart-Allmaras one-equation turbulence model. One case with massive separation was repeated using Menter's two-equation SST  $k-\omega$  turbulence model in an attempt to improve the agreement with experiment. The investigation was conducted at a free stream Mach number of 0.2, and at angles of attack ranging from  $10.004^\circ$  to  $34.858^\circ$ . The Reynolds number based on the mean aerodynamic chord of the wing was  $4.3 \times 10^6$ . Compared to experiment, the numerical procedure predicted the surface pressures very well at angles of attack in the linear range of the lift. However, computed maximum lift was 5% low. Drag was mainly under predicted. The procedure correctly predicted several well-known trends and features of high-lift flows, such as off-body separation. The two turbulence models yielded significantly different solutions for the repeated case.*

## Introduction

As computational fluid dynamics (CFD) has matured, it has become increasingly useful in aircraft design (refs. 1 to 3). For instance, CFD is now widely employed in designing two-dimensional airfoils for cruise. Significant progress has also been made in the challenging area of drag prediction of aircraft configurations (refs. 4 to 6). Progress is even being made in modeling the complex aerodynamics of fully three-dimensional wings configured for the high lift that is demanded at takeoff and landing.

When configured for high lift, wings typical of those on current transports usually have multiple elements and are at relatively high angles of attack. As a result, strong, mutually interacting circulation regions exist around each of the elements. Interaction between the boundary layers and wakes of the elements, the possibility of transonic flow with shocks on the leading-edge slat, boundary layer transition on each element, and the influence of three-dimensional effects, all complicate the flow. The possibilities of laminar separation bubbles on the forward elements, massive separation at the higher angles of attack, and relaminarization of the flow in regions of strong acceleration add even more complexity.

Because of the difficulties of modeling these intricacies, early numerical studies of such high-lift problems were limited to two-dimensional flows. (Three-dimensional flows were usually handled by semi-empirical techniques. See refs. 7 to 9.) The two-dimensional numerical calculations often over predicted the maximum lift compared to wind-tunnel measurements. As advances in grid generation, numerical solution techniques, and computer capacity enabled the analysis of high-lift flows in three dimensions, three-dimensional Navier-Stokes investigations were conducted initially for un-swept wings mounted on wind-tunnel walls. (See refs. 10 to 12.) These studies indicated that the over prediction of lift indicated by the two-dimensional solutions was at least partly due to an experimental loss of lift due to three-dimensional flow, which developed at the juncture of the wing and the wind-tunnel walls during the two-dimensional tests.

As a result, a series of joint computational and experimental investigations of a high-lift wing was initiated for code validation and development. The configuration chosen for the project had a swept trapezoidal wing mounted on a body pod. It has become known as the NASA Trapezoidal Wing. The wing was composed of three elements: the main-wing element, a deployed leading-edge slat, and a deployed trailing-edge flap. The investigations were conducted at a free stream Mach number of 0.2. Experimental measurements included force and moment data, surface pressure data, off-body data, boundary-layer transition data, pressure sensitive paint data, PIV laser data, and acoustic data. These data were taken during several entries in the NASA Langley 14x22 Wind Tunnel, and one entry in the NASA Ames 12-Foot Wind Tunnel. See references 13 to 18. Reference 18 gives an account of the various investigations and the primary data sought for each one.

Refs. 13 and 16 report the comparison of numerical calculations with aerodynamic force-and-moment and surface pressure data from mainly the NASA Ames 12-Foot Wind Tunnel test. These calculations were made with the implicit finite-volume Navier-Stokes code OVERFLOW, and with turbulent viscosity simulated with the Spalart-Allmaras turbulence model. Calculations were made for both free-air and in-tunnel boundary conditions. There was good agreement between the calculated and experimental lift coefficient values at low angles of attack, but large discrepancies between them were observed near the angle of attack for maximum lift. These results also showed that for the most accurate simulation of the wind-tunnel data with large tunnel-wall interference, the numerical calculations needed to simulate the wind-tunnel walls. Reference 19 contains a comprehensive listing and review of CFD subsonic high lift work between the years 1988 and 2002.

More recently (circa 2010), the American Institute of Aeronautics and Astronautics (AIAA) held an international workshop, AIAA HiLiftPW-1, on calculating the flow for the NASA Trapezoidal Wing. Compared to the previous calculations, many of those presented at the workshop showed significant improvements on the agreement with the wind tunnel data. They illustrated the importance of strategically refining the grid, modeling the attachment brackets for the various elements of the wing, modeling boundary layer transition, and

including the cross-derivative diffusion terms for high-lift Navier-Stokes calculations. See references 18, and 20 to 22 for a summary of the results.

The present paper presents the comparison of numerical calculations<sup>1</sup> with the original set of the NASA Langley 14x22 Wind Tunnel data, data that was corrected for wall-interference effects using classical methods and is considered largely wall-interference free (refs. 13 and 23). The numerical computations for the present paper were made with the finite-volume Navier-Stokes code TLNS3D (refs. 24 to 28). Turbulence was modeled by the Spalart-Allmaras one-equation turbulence model (ref. 29). For comparison, one solution at a high angle of attack was repeated with Menter's two-equation  $k-\omega$  Shear-Stress-Transport (SST) turbulence model (ref. 30) since it has predicted more accurate results in separated regions for several configurations (refs. 28 and 30). The numerical calculations for the present paper were made at a free stream Mach number of 0.2, and at eight angles of attack ranging from  $10.004^\circ$  to  $34.858^\circ$ . The Reynolds number based on the mean aerodynamic chord of the wing was  $4.3 \times 10^6$ .

Comparisons are made between the numerical and experimental results for force and moment data, and for the surface pressure coefficients. The results obtained with the two turbulence models are also compared for one case. In addition, trends of the numerical results are compared with other investigations. Since the purpose of the paper was to evaluate the "off-the-shelf" performance of the code and turbulence models, no attempt was made to calibrate the code or turbulence models by adjusting parameters to improve the agreements between

---

<sup>1</sup> These calculations were made in the 2000 to 2004 time frame. Obligations on more pressing research prevented publishing them at that time. This paper is published now to document the work, since it contains a broader analysis (particularly of the flow field) than many other papers, and since many of its findings have been corroborated by later research (examples of which will be cited in the discussion). Thus this paper adds to the volume of work that sheds light onto, and gives confidence in, the basic technology for solving these types of high-lift flows.

the numerical predictions and the experimental data. Finally, the general characteristics of the flow field are discussed.

## Nomenclature

Unless otherwise noted, all variables are normalized by appropriate combinations of the free-stream parameters, the reference length,  $\bar{c}$ , and the reference area,  $S$ .

$b / 2$	wing semi-span, inches
$C_L$	lift coefficient, $\frac{L}{q_\infty S}$
$C_D$	drag coefficient, $\frac{D}{q_\infty S}$
$C_m$	pitching moment coefficient, $\frac{m}{q_\infty S \bar{c}}$
$C_p$	pressure coefficient, $\frac{p - p_\infty}{q_\infty}$
CFD	computational fluid dynamics
constrained streamlines	computed streamlines that have been numerically constrained to a plane
$\bar{c}$	mean aerodynamic chord, inches
$c_{local}$	local chord of the wing in the cruise (stowed) configuration, inches
$D$	drag, pounds
$g_s$	slat gap, inches (see table 1)
$g_f$	flap gap, inches (see table 1)
$h_s$	slat height, inches (see table 1)
IGES	Initial Graphics Exchange Specification format
$L$	lift, pounds
$M$	Mach number
$m$	pitching moment, inch pounds

$O_f$	flap overhang, inches
$p$	pressure, pounds/inch <sup>2</sup>
$q_\infty$	free-stream dynamic pressure, $\frac{\rho_\infty(u_\infty^2 + v_\infty^2 + w_\infty^2)}{2}$ , pounds/inch <sup>2</sup>
Re	Reynolds number based on the mean aerodynamic chord
$r_{\text{norm}}$	perpendicular distance above the model surface divided by the local chord of the wing in the cruise configuration
S	semi-span wing area (i.e., reference area), inches <sup>2</sup>
SA	Spalart-Allmaras turbulence model
SST	Menter's two-equation k- $\omega$ Shear-Stress-Transport turbulence model
TLNS3D	the Navier-Stokes code TLNS3D
t	local wing thickness, inches
tm	turbulence model
URL	universal resource locator
$u, v, w$	velocities in the physical coordinate x, y, and z directions, respectively, inches/second
V	velocity magnitude, $\sqrt{u^2 + v^2 + w^2}$ , inches/second
$V_\infty$	free-stream velocity magnitude, $\sqrt{u_\infty^2 + v_\infty^2 + w_\infty^2}$ , inches/second
$x, y, z$	physical (Cartesian) coordinates in the axial, spanwise, and vertical directions, respectively (origin at the intersection of the wing leading edge and the reflection

	plane with the wing in the cruise configuration), inches
$\tilde{x}$	axial distance from the leading edge of the main wing element divided by the local chord of the wing in the cruise configuration
$x_m, z_m$	distances in the x and z directions, respectively from the (0, 0, 0) reference point to the pitching moment center, (see table 3), inches
$\alpha$	angle of attack, degrees
$\delta$	deflection angle of leading-edge slat or trailing-edge flap, degrees
$\eta$	wing span station, $\frac{-y}{b/2}$
$\eta_{\text{norm}}$	normal distance to the wall, inches
$\eta^+$	law-of-the-wall coordinate, $\frac{\eta_{\text{norm}} \sqrt{\rho \tau_{\text{wall}}}}{\mu}$
$\Lambda$	sweep angle, degrees
$\mu$	absolute viscosity, $\frac{\text{slugs}}{\text{inch second}}$
$\tau_{\text{wall}}$	local shear stress at wall, pounds/inch <sup>2</sup>
$\rho$	density, slugs/inch <sup>3</sup>
Subscripts:	
c/4	wing quarter chord
D	drag
f	flap
L	lift
le	wing leading edge
m	pitching moment
norm	perpendicular to the model surface
s	slat

v	viscous
wall	model surface
wing	wing
$\infty$	infinity, i.e., free stream conditions

## Multi-Element High-Lift Basics

High-lift systems basically consist of trailing-edge devices that increase the turning angle of the flow over the wing, and thus increase lift. Slotted flaps and leading-edge slats additionally energize the boundary layer, and thus assist the flow in negotiating the greater turning angle without separating (see refs. 31 to 34). Reference 31 briefly describes the milestones of their evolution from the aileron that Henry Farman was the first to use in 1908.

Figure 1 depicts most of the well-known features of the flow about a well-configured multi-element wing at a low subsonic speed and a very high angle of attack.<sup>2</sup> Part (a) shows the overall flow; part (b) shows a detail of the flow in the vicinity of the leading-edge slat. Although very complex, much has been learned about its aerodynamic principles (see, for example, refs. 3, 7 to 18, 24, and 31 to 36). Reference 35 gives a theoretical explanation of the effect of gaps, or slots, in multi-element airfoils for conditions at which the Reynolds numbers are sufficiently high to ensure that the boundary layers are turbulent by the time adverse pressure gradients appear. It lists the following primary effects for a properly designed and spaced combination of a leading-edge slat and other airfoil elements:

---

<sup>2</sup> Figure 1 presents a chordwise cut of a Navier-Stokes solution for a multi-element wing at a low subsonic speed and an angle of attack slightly greater than the angle for maximum lift. The lines illustrating the pattern of the flow are computed streamlines that have been numerically constrained to the plane presented. Throughout the paper, lines of this type will be referred to as “constrained streamlines”.

- (1) Slat effect: The circulation on the leading-edge slat opposes the circulation on the downstream elements. It hence reduces the negative pressure peaks on the downstream elements and in doing so relieves the pressure rises required of the boundary layer of the downstream elements.
- (2) Circulation effect: At the same time, the circulation on the downstream element increases the velocity at the trailing edge of the slat, which is inclined to the wing chord. This, therefore, increases the circulation on the slat.
- (3) Dumping effect: The trailing edge of a forward element, such as a slat or a main wing element, is in a region of higher velocity and hence lower pressure than free stream. This relieves the pressure rise required of the boundary layer of the forward element and thus reduces the chance of separation.
- (4) Off-the-surface pressure recovery: The boundary layer emanating from a forward element is dumped at higher velocities than free stream and is dumped away from the wall of the downstream element. Deceleration out of contact with a wall is much more efficient than deceleration in contact with a wall.
- (5) Fresh-boundary-layer effect: The boundary layer of each wing element starts out fresh at the leading edge. Hence the boundary layer on each element is relatively thin and can take a more adverse pressure gradient without separating than if it were thick.<sup>3</sup>

As stated previously, these effects can result in very complex flows, especially at high angles of attack (see refs. 3, 7, and 36; figure 1). First, the

---

<sup>3</sup> It should be reiterated that in reference 35, the boundary layers are considered to be turbulent by the time adverse pressure gradients appear. When a boundary layer starts fresh, it starts at a low Reynolds number and is thin. In discussing effect no. 5, reference 35 uses Stratford's turbulent separation criteria to show that a thin boundary layer can sustain a more adverse pressure gradient than a thick one.

constrained streamlines indicate that strong streamline curvature exists at the leading edge of each element of the wing. At the leading edge of the slat, the yellow-orange-red color in the figure indicates that transonic flow can develop. Each element of the wing develops its own boundary layer under the influence of the local stream; and, on the top surface of the wing the boundary layers grow, shed, overlap, diffuse, and finally merge.

The figure also depicts separation of the flow from the surface in the slat cove, the wing cove, and at the trailing edge of the slat. (At lower angles of attack, the flow on the trailing edge of the flap is usually separated and the flow on the trailing edge of the slat is attached (ref. 27)). Off-body separation, or flow reversal, above and downstream of the airfoil is indicated, a phenomena that occurs at very high angles of attack. Note that a layer of attached flow remains underneath the off-body separation. These complexities plus boundary layer transition from laminar to turbulent flow, the possibility of relaminarization of the flow in regions of rapidly expanding flow, and attachment-line transition effects (see ref. 2), pose a strong challenge for a CFD code to accurately model.

## **High-Lift Configuration**

The configuration selected for the joint computational and experimental project referred to in the introduction was dictated by a desire for one that was relatively simple, yet one that still produced the complex high-lift flows of current transport aircraft (reference 13). These requirements plus experimental considerations led to a semi-span, low-aspect-ratio, swept, trapezoidal wing mounted on a body pod. The wing was composed of three elements: the main-wing element, a leading-edge slat, and a trailing-edge flap. It was untwisted and had no dihedral. It has become known as the NASA Trapezoidal Wing.

Figure 2 depicts the computational rendition of the model together with the grid topology and the computational domain for this study. The wind tunnel walls were not modeled. Figure 3, photographs of the experimental model installed in the Langley 14x22 Foot Wind Tunnel (ref. 13), shows the

configuration in greater detail. Part (a) of the figure shows a top view of the complete wing-body, whereas part (b) shows a bottom view at the wing-body juncture. In part (b), some of the brackets that attach the slat and flap to the main wing element can be seen. The brackets were not simulated in the numerical computations for this paper.

Figure 4 presents sketches of a typical airfoil section of the wing with the slat and flap in both stowed (cruise) and deployed (high-lift) positions. It also lists dimensions of the wing<sup>4</sup>. The high-lift configuration (i.e., with the slat and flap deployed) was the only one considered in this paper; the cruise configuration is used only to report the dimensions of the wing. For the present investigation, the leading-edge slat was deployed at 30.0°, and the full-span trailing-edge flap was deployed at 25.0°. These settings are typical of a landing configuration. The width of the leading-edge slat is constant. The ratio of its chord (measured normal to its leading edge) to the mean aerodynamic chord of the complete wing is 0.126. The ratio of the flap's local chord to the local chord of the complete wing is constant at 0.3 throughout the span of the wing. The positions of the slat and flap relative to the main wing element for the present study are given in table 1. Sketches of airfoils at selected span stations for this configuration are given in figure 5. The sketches illustrate that since the chord of the leading-edge slat is constant, the slat comprises a larger percentage of the chord of the wing at the wing tip than it does at the wing root.

Reference 22 gives more details of the configuration and the experimental model. A complete description of the model is given at the NASA Trapezoidal Wing Web Site (see the appendix for the URL of the site).

---

<sup>4</sup> Since the wing was designed so that the slat and flap could be mounted at various settings, the dimensions of the wing are given with the slat and flap in the cruise position, i.e., with the leading-edge slat and the trailing-edge flap stowed.

## Numerical Procedure

### Computational Domain and Grid

As stated previously, figure 2 illustrates the computational domain and the general topology of the grid. The directions of the physical coordinates of the grid are included. The domain and grid were configured as a collection of C-grids wrapped around the body pod and the elements of the wing (i.e., C-grids in the x-z plane). In the plane perpendicular to the x axis (i.e., the y-z plane) the grid assumed a pseudo-H topology. Symmetry was assumed about the  $y = 0$  plane. The origin of the coordinate system was defined as the intersection of the leading edge of the wing in the cruise configuration with the  $y = 0$  plane.

The domain extended 6.44 mean-aerodynamic-chord (MAC) lengths in front of the origin, 8.55 MAC lengths behind it, 6.35 MAC lengths above and below it, and 5.17 MAC lengths (2.5 wing semi-span lengths) normal to the reflection plane. For comparison, the body pod is 3.00 MAC lengths long. In retrospect, the extent of this domain may be too small for the 3-D high-lift flow field being investigated here. Grids used for more recent NASA Trapezoidal Wing computations extended about 100 MAC lengths from the wing. The total domain is subdivided into 46 grid blocks to facilitate a body-fitted grid around this configuration. Block-to-block connections consisted of both point-to-point matching and patched block surfaces.

Three different grids were investigated: one with a total of  $12.0 \times 10^6$  nodes (fine grid), one with a total of  $6.0 \times 10^6$  nodes (medium grid), and another one with a total of  $1.5 \times 10^6$  nodes (coarse grid). Each grid has the same fundamental topology. The grids are body fitted (i.e., grid lines coincide with the model surface and other boundaries) to facilitate implementation of the boundary conditions. Grid lines are clustered in the vicinity of the model, normal to its surface, in the vicinity of each element of the wing, and near the wing tip. For the medium and fine grids, the number of grid planes in each computational

direction of each block supports three levels of multi-grid. The coarse ( $1.5 \times 10^6$ -point) grid was created from the fine grid by dropping every other grid plane in each of the three computational directions. Therefore, it can support only two multi-grid levels.

The fine grid was created to address problems (to be discussed subsequently) with the  $6.0 \times 10^6$ -point grid by judiciously refining it in regions of high flow gradients. The mesh density in the circumferential direction (i.e., around the airfoil) for each element of the wing was increased in order to better resolve the gradients in the nominal direction of the flow. The density in the spanwise direction near the wing tips was increased to better capture the wing tip vortices. The density normal to the model surfaces was also increased with grid points clustered much closer to the surfaces to better resolve the boundary layers. As a result, for this fine grid, the first grid point off the surface was approximately 0.00002 inches normal to the surface, which resulted in a calculated law-of-the-wall coordinate,  $\eta^+$ , of approximately 0.5 over most of the surface of the wing with attached flow. The fine grid also had significantly lower stretching factors than the medium grid. It was eventually chosen as the baseline grid for the present study. It should be noted that the “fine” grid used for these older computations (circa 2004) would be considered “coarse” by the standards of today (circa 2014).

Table 2 and figs. 6 and 7 present some details of the fine grid. The grid is composed of 46 grid blocks containing a total of 11,971,510 grid points and 11,188,288 cells (See table 2.). Fig. 6 depicts the model surface grid with every other grid line deleted for clarity. Fig. 7 (a), (b), and (c) respectively illustrate the overall grid topology in a vertical cut through the wing, and depict the details of the mesh in the coves of the leading-edge slat and the main wing element. Parts (b) and (c) of the figure show that the small bases at the trailing edges of the leading-edge slat and the main wing element were computationally simulated. The base at the end of the trailing-edge flap was not simulated since it was much smaller than the other two bases.

## Numerical Algorithm

Numerical calculations for the present investigation were made with the three-dimensional thin-layer Navier-Stokes code TLNS3D (refs. 24 to 28). As a generalized thin-layer code, TLNS3D retains the diffusion terms along all principal directions, neglecting only the cross-diffusion terms. To advance the solution in time to a steady-state solution, TLNS3D utilizes a semi-discrete cell-centered finite-volume scheme based on a Runge-Kutta time stepping scheme. The code employs grid sequencing and multi-grid. Linear, fourth-difference and nonlinear, second-difference artificial dissipation terms are added to respectively suppress odd-even decoupling and oscillations in the vicinity of shock waves and stagnation points. Implicit residual smoothing is used to increase the allowable time step. TLNS3D models the effects of turbulence through an eddy-viscosity computed by either the one-equation Spalart-Allmaras or by Menter's two-equation Shear-Stress Transport (SST) turbulence model.

## Turbulence Models

For all the conditions of this investigation, turbulent dissipation was modeled by the Spalart-Allmaras one-equation turbulence model (ref. 29). That model was chosen because it is well established, gives very good results over a wide range of flow conditions, and is available in most modern Navier-Stokes codes. For one angle of attack,  $\alpha = 29.877^\circ$ , Menter's shear-stress-transport (SST) turbulence model (ref. 30) was also employed. It is a two-equation, blended  $k-\epsilon$  and  $k-\omega$  model. It also has a limiter that allows it to more accurately account for the transport of the principal shear stresses in adverse pressure gradients than the Spalart-Allmaras model. The Menter's SST model has been shown to produce more accurate results than the Spalart-Allmaras model for some configurations with reverse flow regions (see refs. 9 and 28). Thus it was thought that it would possibly improve the solution in regions of incipient separation, in separated regions, or in highly vortical regions.

## Boundary Conditions

Because the free stream is subsonic, Riemann invariants for a one-dimensional flow were used to calculate the flow variables at the inflow, outflow, and far-field boundaries of the computational domain (see fig. 2). Reflection boundary conditions were imposed on the  $y = 0$  surface of the computational domain<sup>5</sup>. Finally, a no-slip boundary condition was imposed on all the surfaces of the model.

Since a cell-centered finite-volume algorithm is used in the code, these boundary conditions are employed on a layer of ghost cells (auxiliary cells) that surround the physical boundaries of the faces of the grid blocks. At grid block interfaces, a second layer of ghost cells is also added to facilitate the evaluation of the fourth-difference artificial-dissipation terms across these boundaries.

## Numerical Solution Strategy

In the current work, a 5-stage Runge-Kutta scheme was chosen as the primary solver in the TLNS3D code. Grid sequencing and multigrid with a V-type cycle were also utilized. All solutions were started with the entire flow field set at free stream conditions. Implicit residual smoothing was used for enhancing the stability bounds of the numerical scheme.

The solutions were obtained in single precision mode. However, the interpolation coefficients that transfer information between adjacent patched grid block boundaries were computed in double precision. As a check on the accuracy of the single-precision-solver mode, one double-precision solution was obtained at an angle of attack of  $29.877^\circ$ . The two modes of precision gave nearly identical results for lift, total drag, and skin-friction drag. The double-precision mode, however, resulted in a more negative pitching moment that agreed better with experiment than the single-precision mode.

---

<sup>5</sup> A reflection boundary condition was imposed since the calculations are compared to experimental data that was obtained with semi-span experimental test techniques that minimized the effect of the tunnel wall boundary layer on the model, and closely simulated full-span flow (refs. 13 and 37).

Typically, in obtaining a solution with three levels of multigrid, 150 time steps on the coarse grid were run. This was followed by 150 multigrid cycles on the intermediate grid using two grid levels. The remaining multigrid cycles required for the solution to converge to a steady state were then run on the fine grid using three grid levels.

## Origin Computer Resources Required

The numerical solutions were obtained on the NASA Ames Research Center's SGI Origin computer<sup>6</sup>. For the fine ( $12 \times 10^6$ -point) grid, running in the multigrid mode with three grid levels required the following resources.

Type resource	Amount of resource required	
	Single precision	Double precision
Number of CPUs	20	38
Number of nodes	10	19
Memory/grid point (kb)	0.355040	0.753503
CPU time/grid point/multigrid cycle (sec)	0.000188	0.000298
Wall-clock time/grid point/multigrid cycle (sec)	0.00000949	0.00000945

Hence a single-precision solution required 4.25 gigabytes of memory, and took between 564 and 1112 CPU hours depending on the number of multigrid cycles required for the solution to converge to a steady state. The equivalent wall-clock time took between 28.4 and 60 hours. However, since the solutions were not obtained in one continuous computer run, but were broken into several computer runs of approximately 150 multigrid cycles each, the typical solution took one to two weeks to obtain due to scheduling policies.

---

<sup>6</sup> At the time the numerical calculations were made, 2001 to 2004, the Origin computer was one of the most powerful at NASA Ames Research Center.

## Experimental Data

The experimental data presented in this paper is from the NASA Trapezoidal Wing website. It is listed in table 3. The data consists of that portion from the initial (1998) NASA Langley 14x22 Wind Tunnel investigation of the NASA Trapezoidal Wing. That investigation was originally reported in reference 13. Since then, references 18, 22, and 38 have added valuable information about the model, the experiment, and the repeatability of the data. For completeness, the appendix very briefly describes the aspects of that investigation that are most helpful in assessing the comparison of the present numerical results with that experiment.

## Results

Solutions were obtained with the Navier-Stokes code TLNS3D for the NASA Trapezoidal Wing, a high-lift, three-element wing similar to a transport wing at takeoff and landing. For this study, the leading-edge slat and trailing-edge flap of the wing were deployed at  $30.0^\circ$  and  $25.0^\circ$  respectively. The brackets that attach the leading-edge slat and the trailing-edge flap to the main wing element were not simulated. The study was conducted at a nominal free-stream Mach number of 0.20, and at eight angles of attack ranging from  $10.004^\circ$  to  $34.858^\circ$ . The Reynolds number based on the mean aerodynamic chord of the wing was  $4.3 \times 10^6$ . All calculations were made for free air. The resulting solutions were compared with experimental (i.e., wind-tunnel) data.

### Vetting the Solutions

Reference 39 defines “code verification”, “code validation”, and “code calibration” as:

Code verification: solving the equations correctly

Code validation: solving the correct equations

Code calibration: adjustment of constants and parameters needed to fit experimental data

Reference 37 states that, based on these definitions, code validation is an engineering problem whereas code verification is a mathematical problem.

In the past, TLNS3D has given excellent results on a large variety of problems (see, for instance, refs. 8 and 24 to 28). Although this does not verify that the code solves every detail of the equations correctly in all cases, verification in the present paper will be limited to a discussion of the numerical convergence of the solutions. Validation of the code and turbulence models that were tested will inherently be assessed for the present problem as the numerical solutions are discussed and compared with the experimental data. Since the purpose of the present investigation was to evaluate the “off-the-shelf” performance of the code and turbulence models, there has been no attempt to calibrate the code by adjusting constants or parameters to fit the solutions to experimental data

**Numerical convergence.** Tables 4 and 5 and figure 8 illustrate the numerical, or iterative, convergence for the calculations presented in this paper. The numerical solutions were deemed converged to engineering accuracy when the residual dropped at least two orders of magnitude and the values of the lift and drag coefficients changed one tenth of one percent or less in the last 100 multigrid cycles. Table 4 lists all the cases run. It includes the numerical precision and the number of multigrid cycles run. Table 5 lists the lift, drag, and pitching moment coefficient values, and the percentage change in these coefficients in the last 100 multigrid cycles for all the cases. As the table shows, the changes of the lift, drag, and pitching moment coefficient values are equal to or less than 0.1% in almost all the cases. The exception was at the combination of 10.852° angle of attack and the medium grid. The pitching moment also failed to reach these criteria at 14.000° angle of attack.

Figure 8 illustrates a problem that only showed up for the combination of the medium grid and an angle of attack of 14.000°. The figure compares the numerical convergence for both the medium and fine grids at this condition. The residual for the solution with the medium grid dropped almost four orders of

magnitude. However, the solution never actually settled out.<sup>7</sup> Figure 8 also shows that although the residual for the fine grid only dropped approximately two orders of magnitude, the lift and drag coefficients settled out to a relatively constant value. These coefficients were monitored for all the solutions for each of the three grids and all angles of attack, and they settled out to a relatively constant value in all cases except the one just discussed.

**Grid convergence.** Reference 40 states that for a mathematically formal grid convergence study of a multidimensional problem with a single grid size measure, all the grids must belong to the same family, i.e., the aspect ratio of each successive grid has to remain constant. In addition, the solutions on each grid must be sufficiently converged, preferably with residuals reduced several orders of magnitude.

Due to the computer resources available and time constraints for the present investigation, strictly meeting the previous requirements was not possible. However, solutions obtained on the three grids, the fine grid, the medium grid, and the coarse grid, were compared in an attempt to assess grid convergence. See the section, "Computational Domain and Grid", for a detailed description of the grids.

Table 6 presents the force-and-moment results for these solutions at four angles of attack:  $10.004^\circ$ ,  $10.852^\circ$ ,  $14.000^\circ$ , and  $29.877^\circ$ . Initially, the medium grid was created, and solutions were obtained at three angles of attack,  $10.852^\circ$ ,  $14.000^\circ$  and  $29.877^\circ$ . The first angle of attack,  $10.852^\circ$ , was mistakenly run instead of  $10.004^\circ$ . A comparison of these three solutions with the experimental data indicated that the grid should be improved. Thus the  $\alpha=10.852^\circ$  solution was not repeated at the correct angle of attack. It is, however, presented in table 6 to help assess grid convergence.

Table 6 shows that the lift coefficients are very close for the fine and medium grids. In addition, the lift coefficient for the coarse grid is relatively close to lift coefficient of the other two grids at an angle of attack of  $10.000^\circ$ . It does not agree as closely at an angle attack of  $29.877^\circ$ , a result that might be

---

<sup>7</sup> This numerical iteration was terminated at 2000 multigrid cycles to conserve computer resources.

expected considering the strong flow gradients encountered at this condition and the coarseness of the lowest grid density.

Based on the results presented in table 6, the  $12 \times 10^6$  node, or fine, grid was **selected as the baseline grid** for this study. The subsequent comparison of the numerical calculations with experimental data, and the discussion of the predicted flow characteristics of the problem are all based on solutions obtained with the  $12.0 \times 10^6$  node, or fine, grid.

## Forces and Moments

Figure 9 and table 7 present a comparison of the computed and experimental lift, drag, and pitching moment coefficients. The values of the experimental data listed in table 7 are linearly interpolated (for either  $\alpha$  or  $C_L$  as the independent variable) from the experimental data given in table 3.

**Lift coefficient.** Figure 9(a) presents the computed and experimental lift coefficients versus angle of attack. At  $10.004^\circ$  angle of attack, the lift coefficients agree within 0.99%. At  $19.937^\circ$ , they agree within 2.11%. See table 7 for the exact values. These values, in this linear range, yield slopes of the lift curves of 0.065 for the computations, a slope that is within 4% of the experimental value. At maximum lift, traditionally one of the most difficult parameters to determine accurately (ref. 30), the calculated lift coefficient is approximately 5.40% low. See the following values taken from table 7 at constant  $\alpha$ .

$\alpha$	$(C_{L, \text{numerical}} - C_{L, \text{experimental}}) / C_{L, \text{experimental}}$
10.004	-0.99%
14.000	-1.28%
19.937	-2.11%
27.908	-3.41%
28.120	-4.80%
29.877	-4.80%
32.993	-5.40%

The predicted or calculated angle of attack for maximum lift is about  $32.993^\circ$ . This is close to the experimental value of  $33.7^\circ$ . The lack of additional solutions at angles of attack near  $33^\circ$  prevents a more exact assessment of the computed angle of attack for maximum lift, or for stall. At angles of attack

greater than the angle for maximum lift, the computed lift drops as it should, but not as abruptly as the experimental data. Similar results were reported in ref. 11.

Attempts were made to get better agreement between the numerical calculations and the experimental data at  $29.877^\circ$  angle of attack. As stated previously in the section on the numerical procedure, the solutions were obtained in single precision on the NASA Ames Origin computer complex. A double precision solution was tried but showed no improvement. Substituting Menter's SST turbulence model for the Spalart-Allmaras model also failed to improve the agreement. As will be discussed subsequently, the prediction of maximum lift possibly may be improved by increasing the spanwise density of the grid near the wing tip. Another possibility may be by modeling the test section of the wind tunnel (ref. 11). However, as previously stated, in the Langley 14x22 Foot Tunnel, the wall interference is believed to be relatively small and the corrections to free air accurate. Even though the computed maximum lift is low, it is at least a reasonable estimate of the experimental value.

The present high-lift problem has recently been the subject of many other investigations. Reference 41, for example, reports a very careful study of grid resolution for it, and of modeling the brackets that attach the slat and flap to the main wing element. By strategically refining the grid, it greatly improved the agreement between experiment and computations at high angles of attack. This was confirmed in reference 42 which included even finer grids. Including the attachment brackets decreased the computed  $C_L$  and increased  $C_D$ . Also see references 18, and 20 to 22 that summarize the results of the First AIAA CFD High-Lift Prediction Workshop. Examples of additional studies of this problem are: effects of grid resolution, references 43 to 45; effects of modeling the brackets, references 46 and 47; effects of modeling transition, references 47 to 50; effects of thin-layer versus full Navier-Stokes solvers, reference 46; and the effects of hysteresis, reference 51. A complete list of publications directly related to the First High-Lift Workshop can be accessed at the URL for the workshop. See the appendix.

**Drag coefficient.** Figure 9(b) presents drag coefficient versus angle of attack. Again, the major discrepancy between the computations and experiment is at the higher angles. However, the discrepancy at angles of attack of  $19.937^\circ$

and below is now on the order of  $-6.11\%$  to  $-7.97\%$ , and about  $10\%$  at the higher angles. At maximum lift, it is  $-8.58\%$ . As with lift coefficient, the drag coefficient is under predicted at all angles of attack. See the values below taken from table 7. It is well known that drag is more difficult to predict accurately than lift (see ref. 6).

$\alpha$	$(C_{D, \text{numerical}} - C_{D, \text{experimental}}) / C_{D, \text{experimental}}$
10.004	$-6.11\%$
14.000	$-7.08\%$
19.937	$-7.97\%$
27.908	$-10.06\%$
28.120	$-10.09\%$
29.877	$-9.57\%$
32.993	$-8.58\%$

Part (c) of figure 9 presents a plot of drag coefficient as a function of lift coefficient. It shows, as does the following comparison from table 7 at constant values of  $C_L$ , an overall improvement over the comparison versus constant  $\alpha$ . Versus constant  $C_L$ , the computed drag coefficient is under-predicted by  $-4.06\%$  to  $-5.45\%$  at the lower values of lift, and up to  $+8.59\%$  near the maximum value of  $C_L$ .

$C_L$	$(C_{D, \text{numerical}} - C_{D, \text{experimental}}) / C_{D, \text{experimental}}$
1.806	$-4.55\%$
2.078	$-5.45\%$
2.447	$-4.06\%$
2.790	$0.62\%$
2.796	$0.72\%$
2.845	$2.32\%$
2.867	$8.59\%$

That the numerical computations were made with the boundary layers fully turbulent leads one to question how this might effect the agreement between the computations and experiment. The fact that skin friction drag is such a minor part of the total drag (see table 5), suggests that skin friction, in this case, is of secondary importance. More importantly, modeling boundary layer transition would insure that the boundary layers on each element were in the correct state

as they mutually interacted. Transition also has a major influence on reducing flap separation (see refs 43, and 47 to 49) which affects the overall solution, including the drag.

In addition to not precisely modeling the state of the boundary layer over the entire surface, the brackets that attach the slat and flap to the main wing element were not modeled for the computations. One would expect that including the brackets in the computations would increase the computed drag and thus the agreement with experiment. Again, reference 41 indicates that including the brackets in the computations significantly increased the drag but decreased the lift except at the very low angles of attack (see also refs. 20, 46, and 47).

**Pitching moment coefficient.** The calculated pitching moment coefficient, fig. 9(d), follows the correct trends with angle of attack. Similar to the lift coefficient, it agrees best with experiment for the angles of attack that fall within the linear range of the lift curve ( $\alpha = 19.937^\circ$  or less). At the higher angles of attack, the pitching moment coefficient fails to compare well with the data (see table 7). This would be expected since both the lift and drag coefficients also fail to match the experimental data well at these angles. Reference 46 indicates that including the full viscous flux operator in Navier-Stokes solutions can significantly increase lift and reduce pitching moment.

$\alpha$	$(C_{m, \text{numerical}} - C_{m, \text{experimental}}) / C_{m, \text{experimental}}$
10.004	-4.31%
14.000	-5.24%
19.937	-7.22%
27.908	-13.20%
28.120	-13.24%
29.877	-13.16%
32.993	-15.50%

**Force-and-moment summary.** The present numerical study gave results similar to many of the entries submitted to the first AIAA CFD High-Lift Prediction Workshop, AIAA HiLiftPW-1 (ref. 20). The numerically computed lift, drag, and pitching moment of the present study exhibit the correct trends with angle of attack. The computed lift agrees relatively well with experiment in the

linear range ( $\alpha = 19.937^\circ$  or less) of the lift curve. In addition, the computations give reasonable estimates of the maximum lift and of the angle of attack at maximum lift. These are all very important parameters in aircraft design that affect the efficiency, range, takeoff characteristics, and maximum payload of the airplane (refs. 2 and 30). Thus, the present study adds to the volume of work that helps confirm, and sheds insight into, the basic technology for calculating complex high-lift flows.

Based on this basic technology, and with the help of more powerful computers, significant progress in predicting wind tunnel results has been made since the present calculations were completed. Again, see reference 20. Improvements due to modeling transition, improved grid resolution, modeling the brackets that attach the slat and flap to the main wing element, and including a full viscous flux operator (i.e., not thin-layer) in Navier-Stokes solvers have already been noted in the previous sections. These newer results imply that much of the disagreement between calculations and experiment for high-lift flows that has traditionally been attributed to turbulence modeling can be overcome by using sufficiently fine grids and by including these other details.

## Surface Pressures

Figure 10 presents a comparison of the computed and experimental pressure coefficient distributions at several span stations of the wing. The computations presented in this figure were all made with the basic grid and turbulence model for the investigation (the fine grid and the Spalart-Allmaras turbulence model). The sketches in the figure depict the locations of the numerical and experimental pressures. The pressure distributions are presented at each angle of attack for which solutions were obtained (i.e., angles of attack ranging from  $10.004^\circ$  to  $34.858^\circ$ ).

Figure 10 illustrates that, over most of the span of the wing, there is generally very good agreement between the computed pressure distributions and experiment. For the leading-edge slat and the main wing element, the agreement is excellent at all angles of attack through the angle for maximum lift,  $32.993^\circ$ . At the outermost span station of  $\eta = 0.95$ , the agreement between the

numerical computations and experiment is not as good. This exception will be discussed subsequently.

Figure 10 further shows that the numerical computations correctly predict several trends that are indicated by the experimental data. First, as angle of attack is increased up to the angle for maximum lift, the slat and the main wing element become more heavily loaded, resulting in the negative pressure peaks on these elements increasing dramatically. In contrast, the negative pressure peak on the trailing-edge flap at first remains relatively constant with an increase in angle of attack, and then decreases at the higher angles. Also, as the angle of attack increases beyond the angle for maximum lift and the main element unloads, the unloading effect starts at the wing tip and progresses inboard. The calculations correctly capture this trend. However, the calculations predict that the trend starts at the slightly lower angle of attack of  $\sim 34.0^\circ$  vs.  $35.5^\circ$  for the experiment.

## Flow-Field Observations

**Conceptual illustration.** Figure 11 conceptually illustrates simulated oil flows on the model surface as well as details of the flow in a vertical plane cutting the wing with the model at a very high angle of attack ( $\sim 35^\circ$ ). Similar details of the computed flow immediately above the model surface and in this plane are respectively presented for each of the angles of attack investigated. See figures 12 to 19. These figures help illustrate the interaction of the boundary layers and wakes emanating from each of the three elements of the wing.

**Separation and correlation with surface pressures.** Except at the outermost span station of  $\eta = 0.95$ , neither the computed nor experimental pressure coefficient distributions (figure 10) indicate much evidence of separation.<sup>8</sup> In contrast to the pressure coefficients, at  $\alpha = 10.004^\circ$ , the computed streamlines that

---

<sup>8</sup> The separation indicated by the experimental pressures at span stations of 0.50 and 0.65 and at angles of attack above  $28.120^\circ$  is probably strongly influenced by the slat and flap attachment brackets that are located at  $\eta=0.47$  and  $\eta=0.61$  respectively.

are constrained very close to the surface of the trailing-edge flap show a small separated region at the trailing edge of the flap. The computations further predict that this separated region grows with angle of attack, reaches a maximum at about  $\alpha = 19.937^\circ$ , diminishes, and disappears altogether at  $\alpha = 34.858^\circ$ . Figure 20 summarizes this effect. The computations also predict that as the flow on the flaps evolves from separated to attached flow, the flow on the leading-edge slat evolves from attached to separated flow. These trends are typical of multi-element high-lift systems that have been optimized for maximum lift (refs. 5 and 27). Further examination of figs. 12 to 19 shows that this separation on the flap is limited to a very thin region close to the surface. (See the Mach number contours, the constrained streamline patterns, velocity vectors, and boundary layer profiles presented in parts (b), (c), and (d) of these figures.) Because the separation is so thin, it is not readily evident by examining the pressure distributions. At the very high angles of attack there is massive off-body separation that will be discussed subsequently.

**Shear layers and velocity profiles.** The computed velocity vectors and velocity profiles close to the model surface also illustrate the various shear layers trailing from the different elements of the wing. (At the time when the present calculations were made, no experimental boundary layer profiles were available for comparison. Experimental velocity profiles for this configuration are now published in reference 38.) Below an angle of attack of  $19.937^\circ$ , the velocity vectors and profiles on the main wing element, parts (c) and (d) respectively of figures 12 to 19, do not show a significant velocity defect from the leading-edge slat. (The imaginary rakes depicted on the figure are to only show the location of the velocity profile. No physical rake was simulated for this numerical investigation.) However at  $\alpha = 19.937^\circ$ , the boundary layer on the main wing element (i.e., at  $\tilde{x} = 0.50$ ) begins to show a defect that is probably the shear layer from the leading-edge slat. At angles of attack of  $28.120^\circ$  to  $32.993^\circ$ , the shear layer emanating from the slat is quite evident in the profiles on the main wing element.

In contrast to the profiles on the main wing element, the boundary layer profiles on the trailing-edge flap clearly show the shear layer emanating from the

main wing element at all angles of attack. In addition, at angles of attack of  $28.120^\circ$  to  $32.993^\circ$ , the shear layer from the slat, although it has largely dissipated, still appears to be evident in the profiles on the flap (at  $x_{\text{bar}} = 0.85$ ). Above  $\alpha = 32.993^\circ$ , the profiles at both axial stations illustrate off-body separation with a thin underlying layer of attached flow.

An examination of the details of the shear and boundary layers associated with each element of the wing suggests that each layer must be well resolved to accurately predict the aerodynamic force and moments. Reference 39 and 42 confirm this speculation. Reference 39 showed that as angle of attack increases, properly resolving the boundary and shear layers emanating from the forward elements becomes increasingly important, especially at angles of attack near stall. Reference 48, for example, further showed that transition location and including rotation and curvature effects in turbulence modeling significantly affected the accuracy of predicting the forces and moments. References 43, 47, and 49 to 50 also illustrate that transition has a major influence on flap separation. The complexity implies that automatic grid refinement could be very useful in adequately resolving the flow.

**Stagnation points.** The computations show an interesting change in the stagnation line as angle of attack increases. As would be expected, and as figs. 12 through 19 show, the stagnation line on the leading-edge slat moves aft as angle of attack is increased. It moves from approximately the leading edge of the slat to the corner of the slat cove where it appears to set up a saddle point just off the surface. Also, as would be expected, the stagnation line of the main wing element moves aft with increasing angle of attack. However, for the main wing element, the location of the stagnation points near the wing root and tip remain relatively constant with increasing angle of attack. This results in a rearward bowing of the stagnation line in the middle of the wing. In contrast, the stagnation line on the leading-edge slat remains relatively straight. Figure 21 shows computed oil flows (actually streamlines constrained immediately above the model surface) for the bottom view of the juncture of the leading edge of the wing with the fuselage. Unlike the slat and main wing element, the stagnation line for the trailing-edge flap moves very little with changes in angles of attack (refer to figs. 12 to 19).

**Off-body separation.** Figures 17 to 19 show that for the computations, at the angle of attack of maximum lift,  $\alpha = 32.993^\circ$ , the flow begins to separate at the outboard section of the leading-edge slat. In addition, the flow develops a massive low velocity region off the body that is centered just downstream and above the trailing-edge flap. As the angle of attack increases, the separation on the leading-edge slat progresses inboard. Simultaneously, the low velocity region moves forward, off-body separation develops, and the accompanying vortices develop in the huge separated region. Underneath this huge separated region, a thin layer of attached flow remains next to the upper surfaces of the main wing element and the trailing-edge flap. See the velocity vectors and the boundary layer profiles, parts (c) and (d) of the figures.

**Wing-tip vortices.** Figure 22, which presents plots of the wing vortices at several angles of attack, also shows these trends of separation with angle of attack. At  $\alpha = 10.004^\circ$ , the wing tip vortex and the vortex sheet behind the trailing edge of the wing are well defined. At  $\alpha = 29.877^\circ$ , the tip vortex and vortex sheet begin to dissipate. At  $\alpha = 32.993^\circ$ , vortex dissipation increases, and separation at the tip of the leading-edge slat can be detected. (Note the streamline that originates on the slat and the flow pattern depicted in fig. 17(a).) At  $\alpha = 34.858^\circ$ , massive separation occurs and the tip vortex is well dissipated. As one would expect, this complex flow at the wing tip is extremely difficult to predict. Other research as reported in at the First AIAA HiLift Prediction Workshop (ref. 40) confirms this difficulty. As a matter of interest, a vortex forming at the juncture of the wing and body, another well-known phenomena (ref. 27), can be seen to develop and become well defined as angle of attack increases.

These phenomena are reflected in the computed pressure coefficients (compare fig. 10 parts (e), (f), (g), and (h)). As angle of attack increases beyond the angle for maximum lift ( $\alpha \approx 33.0^\circ$ ), the peak expansions progressively become less severe. Correspondingly, the recompressions that occur over the latter part of the airfoil progressively become flatter and less negative. These effects start at the wing tip and progress inboard as angle of attack increases. The experimental data tend to exhibit the same pattern, although its onset is delayed. In addition,

near the tip of the wing, the levels of the pressure coefficients on the leading-edge slat also drop and flatten out, thus indicating separation on the slat. Again, the fact that the numerical procedure correctly predicts these data and known trends (refs. 5 and 24) reflects very positively on its ability to handle very complex flows of this nature.

At the outermost span station,  $\eta = 0.95$ , the computed pressure coefficients on the trailing-edge flap are less negative than experiment (see fig. 10). This discrepancy between computations and experiment increases with increasing angle of attack. The increase in the discrepancy eventually works its way forward onto the main wing element and even onto the leading-edge slat at  $\alpha = 33.980^\circ$  and  $34.858^\circ$ . Since this span station is in the vicinity of the wing tip vortex (see fig. 23), the discrepancy is probably due to the failure of the computations to accurately model the wing-tip vortex.

As this low velocity region is moving forward with increasing angle of attack, the influence of the wing tip vortex and off-body separation is progressing from the wing tip inboard. Therefore, it is possible that these phenomena, which are simultaneously changing with angle of attack, were changing at slightly different rates or conditions for the computed and experimental flows. Under these circumstances, precisely matching the experimental results with numerical calculations would almost be fortuitous.

Other possible sources of error include inadequate grid density (see refs. 20, 41, and 42). Since the locations of the tip vortex and the shear layers trailing from the individual wing elements change with angle of attack (see figs. 12 to 19, and 22), the areas of the grid that are refined to capture these features should track them as angle of attack changes. Modeling the leading-edge slat and trailing-edge flap brackets, and modeling boundary layer transition may also help in pinpointing the source of these differences near the wing tip. Later research (ref. 46) suggests that Navier-Stokes algorithms that include the cross derivative diffusion terms, terms not included in the present thin-layer computations, can significantly reduce separation at the wing tip and improve agreement with experiment. As always, one wonders if the turbulence model is performing adequately in this particularly complex flow.

## Effect of the Turbulence Model

A very limited investigation was conducted on the effect of the turbulence model on the solution. At the angle of attack of  $29.877^\circ$ , in addition to the Spalart-Allmaras one-equation turbulence model, Menter's two-equation SST turbulence model was investigated. Menter's SST model is a blended  $k-\epsilon$   $k-\omega$  model. It utilizes a limiter that allows it to more accurately account for the transport of the principal shear stresses in adverse pressure gradients than the Spalart-Allmaras model. Hence, the author thought that Menter's model might capture the physics better in regions of pending separation, separation, or maybe even strong vortical flow than the Spalart-Allmaras model. However, as table 4 and figure 9 show, Menter's model yielded a two percent lower lift coefficient value than the Spalart-Allmaras yielded, and therefore did not improve the correlation of the computations with the experimental data.

Figure 23 presents the pressure distributions for the two turbulence models at span stations of  $\eta = 0.70$  and  $\eta = 0.95$ . Little difference exists between the distributions for the two turbulence models except for a slight difference on the trailing-edge flap. However, these seemingly insignificant differences in pressures can integrate into significant differences in forces as they have in the present case. See figure 9 and tables 4 and 5 (cases 7 and 7-SST).

Figure 24 presents the effect of the turbulence model on details of the computed flow. There is relatively little difference in the constrained streamlines immediately above the surface (part (a)) between the two turbulence models except in a small region near the trailing edge of the trailing-edge flap at the wing tip. This might lead one to conclude that the turbulence model makes relatively little difference in the solution. However, an examination of the large region of low velocity flow downstream of the trailing-edge flap shows that the constrained streamlines and velocity vectors for the two models (parts (b) & (c)) exhibit a significant difference in the solutions in this region.

This difference is further illustrated by the velocity profiles presented in figure 25. At the span station  $\eta = 0.70$ , which is typical of all inboard span stations, there is little difference between the velocity profiles predicted by the

two turbulence models on the main wing element. The profile immediately next to the surface of the trailing-edge flap is approximately the same for the two turbulence models also. However, the shear layer emanating from the main wing element is slightly thicker and at a lower velocity for Menter's SST model than for the Spalart-Allmaras model.

At the outermost span station,  $\eta = 0.95$ , the profiles indicate a huge low-velocity region over both the main wing element and the trailing-edge flap. As mentioned before, there is an underlying high-velocity layer of attached flow next to the surface. In this case, Menter's SST turbulence model gave a higher velocity than the Spalart-Allmaras model. In addition, the underlying high-velocity layer of attached flow on the flap is thicker and has a decidedly different profile. Perhaps these differences are an indication of a significantly different wing-tip vortex generated by the two models. See figure 26, which illustrates the effect of the turbulence models on the wing vortices.

Figure 26 shows that the Menter two-equation SST turbulence model gives a slightly better developed wing tip vortex than the Spalart-Allmaras one-equation turbulence model. Also the vortex sheet immediately behind the wing appears to be stronger for Menter's model. These results indicate that the turbulence model can have a significant effect on the solution of three-dimensional multi-element high-lift flows. Reference 48, an investigation of transition and advanced turbulence modeling for this problem, tends to confirm this hypothesis. It shows that including transition and rotation/curvature effects usually improved correlation with experiment. Again, see reference 46 which indicates that including the full viscous flux operator in Navier-Stokes solutions can significantly increase lift and reduce pitching moment.

## **Concluding Remarks**

Solutions were obtained with the Navier-Stokes CFD code TLNS3D to predict the flow about the NASA Trapezoidal Wing, a high-lift wing composed of three elements: the main-wing element, a deployed leading-edge slat, and a

deployed trailing-edge flap. The brackets joining the wing elements were not modeled. Turbulence was modeled by the Spalart-Allmaras one-equation turbulence model. For comparison, one solution at  $29.877^\circ$  angle of attack was repeated with Menter's two-equation  $k-\omega$  Shear-Stress-Transport (SST) turbulence model. All calculations were made with the assumption that the boundary layers were fully turbulent. The investigation was conducted at a free stream Mach number of 0.2, and at angles of attack ranging from  $10.004^\circ$  to  $34.858^\circ$ .

The numerical results predicted the correct trends of lift, drag, and pitching moment with angle of attack. In the linear range of the lift curve,  $\alpha = 10.004^\circ$  to  $19.937^\circ$ , the computed and experimental lift coefficients agree well. At  $10.004^\circ$  angle of attack, the computations are 0.99% low, and at  $19.937^\circ$ , 2.11% low. This results in a predicted lift curve slope that is within 4% of the experimental value. At maximum lift, the calculated lift coefficient is approximately 5.40% low. The predicted or calculated angle of attack for maximum lift is about  $33.0^\circ$  versus an experimental angle of  $33.7^\circ$ . Versus angle of attack, the computed drag coefficient is between 6.11% and 7.97% lower than experiment in the linear range of the lift curve, and 8.58% lower at maximum lift. Versus  $C_L$ , the drag coefficient is 4.55% to 4.06% lower in the linear range, and 8.59% higher at maximum lift. The predicted pitching moment, largely driven by the lift, is 4.31% to 7.22% lower experimentally at angles of attack within the linear range of the lift curve, and 15.50% at the angle for maximum lift. As one might expect, at angles of attack beyond the angle for stall, all three of the predicted aerodynamic parameters fail to match the experimental data well. These force and moment results are similar to many other calculations for this problem.

Over most of the span of the wing, there is generally very good agreement between the values of the computed and experimental pressure coefficients. For the leading-edge slat and the main wing element, the agreement is excellent at all angles of attack through the angle for maximum lift,  $33.0^\circ$ . At the outermost span station of  $\eta = 0.95$ , which is heavily influenced by the wing-tip vortex, the agreement between the computations and experiment is not as good.

The numerical computations correctly predict several trends and features of the flow that are typical of multi-element systems optimized for maximum lift. First, as angle of attack is increased up to the angle for maximum lift, the slat and the main wing element become more heavily loaded, with the negative pressure peaks on these elements increasing dramatically. In contrast, the negative pressure peak on the trailing-edge flap at first remains relatively constant with an increase in angle of attack, and then decreases at the higher angles. The computations predict that there is a separated region on the trailing-edge flap at low angles of attack. The separated region disappears at the higher angles. In contrast, the predicted flow on the slat is at first attached, and then separates as angle off attack is increased through the same range. Experimental data confirm these trends. The numerical procedure also predicts that at the angle of attack of maximum lift, the flow develops a massive low velocity region off the body. As the angle of attack increases, the low velocity region moves forward, off-body separation develops, and the accompanying vortices develop in the huge separated region. Underneath this huge separated region, a layer of attached flow remains next to the upper surfaces of the main wing element and the trailing-edge flap. These trends and features of the flow start at the wing tip and progress inboard with increasing angle of attack.

At  $29.877^\circ$  angle of attack, Menter's SST turbulence model yielded a 2% lower lift than the Spalart-Allmaras model. It also gave a slightly better developed wing tip vortex than the Spalart-Allmaras model. In addition, the constrained streamlines and velocity vectors for the two models are significantly different in the large region of low velocity downstream of the trailing-edge flap.

The overall good prediction of the lift parameters and surface pressures coupled with the correct prediction of many flow features and trends favorably reflects on the ability of present Navier-Stokes procedures to solve this complex high-lift problem. Since the present computations were made, many other strides (largely made possible by more powerful computers) have been made in this area. Using finer grids, a more detailed modeling of the configuration (such as modeling attachment brackets), including boundary layer transition, and including the cross-derivative diffusion terms (full Navier-Stokes) have all significantly improved the agreement between calculations and experiment. The

success of these later techniques suggests that their application can overcome much of the traditional discrepancy between computations and experiment, a discrepancy that has often been attributed to the turbulence model. However, progress is still necessary before numerical results can routinely replace wind tunnel data for high-lift flows.

## Appendix

### Experimental Apparatus and Procedure

The experimental data presented in the present paper is from the NASA Trapezoidal Wing Web Site. The force, moment, and pressure data presented is from the initial (1998) NASA Langley 14x22 Wind Tunnel portion of the investigation of the NASA Trapezoidal Wing. That investigation was originally reported in reference 13. Since then, references 18, 22, and 38 have added valuable information about the model, the experiment, and the repeatability of the experimental data. The “original” trap wing web site (i.e., the data for this paper) can be accessed from a link to the 1st Workshop (HiLiftPW-1) Website Home Page. The link is listed in the new HiLiftPW Home Page:

<http://hiliftpw.larc.nasa.gov>

For completeness, this appendix briefly describes the aspects of that investigation that are most pertinent in helping assess the comparison of that experimental data with the present computational results.

#### Wind Tunnel

The Langley 14x22 Subsonic Tunnel is a closed-circuit, single-return, atmospheric wind tunnel with a maximum speed of about 338 ft/sec. The maximum unit Reynolds number is  $2.1 \times 10^6$  per foot. Low levels of test section turbulence are achieved through the combined effects of a fan diffuser grid, a flow-straightening honeycomb, four anti-turbulence screens, and a 9-to-1 contraction ratio. To minimize test-section-wall interference on the flow over research models, the test section can be operated in a variety of configurations – closed, slotted, partially open, and open. The tunnel may also be configured with a floor boundary-layer removal system at the entrance to the test section. For the present investigation, the test section and slots were both closed. Reference 23 gives a through description of the wind tunnel.

## **Model**

For the experimental portion of the combined project referred to in the introduction, a large model with a high Reynolds number and a thick boundary layer that could be measured with pneumatic instrumentation was highly desired (ref. 13). These requirements led to a semi-span, low-aspect-ratio, swept, trapezoidal wing mounted on a body pod. The wing was composed of three elements: the main-wing element, a leading-edge slat, and a trailing-edge flap. It was untwisted and had no dihedral. The wing of the experimental model had a semi span of 85.1 inches, and a mean aerodynamic chord of the wing of 39.6 inches. Since the wing was designed so that the slat and flap could be mounted at various settings, the dimensions of the wing are given with the slat and flap in the cruise position, i.e., with the leading-edge slat and the trailing-edge flap stowed. Note that the high-lift configuration (i.e., with the slat and flap deployed) was the only one investigated in the present numerical study; the cruise configuration is used only to report the dimensions of the wing.

The model was mounted from the floor of the wind tunnel as shown in figure 3. Mounted in this way, its wing tip extended to within approximately 6 inches of the tunnel centerline. Figure 3 shows that the wing was outfitted with the full-span flap for this investigation (ref. 13). References 18, 22, and 38 list more information about the model, and a complete description of it is given at the NASA Trapezoidal Wing Web Site. The site contains files that provide the model surfaces in Initial Graphics Exchange Specification (IGES) format, and gives detailed instructions for transforming the slat and flap between their stowed and deployed positions.

## **Instrumentation**

Force and moment data were obtained with a strain-gage balance that was accurate to within  $\pm 3.0$  pounds normal force,  $\pm 2.2$  pounds axial force, and  $\pm 47.0$  inch-pounds pitching moment (these are a 2-sigma level). The nominal free-stream dynamic pressure for this test was 58.3 pounds per square foot. Hence, based on the model reference area, etc. (figure 4), the typical balance

accuracies stated in terms of aerodynamic coefficients are approximately: +/- 0.0024 in its normal direction, +/- 0.0017 in its axial direction, and +/- 0.00095 in pitching moment. The pressures were measured with electronic pressure scanning modules of 1.0, 2.5, 5.0, and 15.0 pounds per square inch full scale. Each pressure module was accurate to within 0.05 percent of full scale.

## **Procedure**

The wind tunnel investigation (reference 13) was conducted at a free stream Mach number of 0.2, and at angles of attack ranging from  $-4.0^\circ$  to  $36.0^\circ$ . To obtain a relatively thin tunnel-wall boundary layer in the vicinity of the model, the tunnel-floor boundary layer was removed at the entrance to the test section. (see ref. 37 for semi-span testing techniques.) In addition, the model was mounted with the  $y = 0$  surface of the body pod slightly above the tunnel floor. Reference 37 states that for semi-span testing, a standoff distance of two times the wall boundary layer displacement thickness resulted in the closest simulation of full-span results. These techniques were followed to closely simulate a reflection condition at  $y = 0$ .

The experimental force and moment data corrected for wind-tunnel wall interference by classical wall corrections are used in the present paper. Table 3 lists the data. These Langley wind-tunnel data are considered largely interference free, and the corrections to free air are considered accurate (see refs. 13, 23, and 38). The Trapezoidal Wing Web Site described previously gives detailed information for the experimental data and investigation. References 18, 22, and 38 give a thorough description of the model, the investigation, and analysis of the data. They describe the repeatability of the data including the effect of hysteresis with increasing and decreasing angle of attack and the effect of tunnel entries.

## References

1. Campbell, Richard L.: Efficient Viscous Design of Realistic Aircraft Configurations. AIAA Paper 98-25389, 1998.
2. Vos, J. B.; Rizzi, A.; Darracq, D.; and Hirschel, E. H.: Navier-Stokes Solvers in European Aircraft Design. Pergamon, Progress in Aerospace Sciences 38, pp. 601-697, 2002.
3. van Dam, C. P.: The Aerodynamic Design of Multi-Element High-Lift Systems for Transport Airplanes. Pergamon, Progress in Aerospace Sciences 38, pp. 101-144, 2002.
4. Lee-Rausch, E.M., Frink, N.T., Mavriplis, D.J., Rausch, R.D., Milholen, W.E.: "Transonic Drag Prediction on a DLR-F6 Transport Configuration Using Unstructured Grid Solvers", AIAA 2004-0554, January 2004.
5. Rumsey, Christopher L.; Rivers, S. Melissa; and Morrison, Joseph H.: Study of CFD Variation on Transport Configurations from the Second Drag-Prediction Workshop. AIAA Paper 2004-0394, January 2004.
6. Hensch, M. J.; and Morrison, J. H.: Statistical Analysis of CFD Solutions from the 2nd Drag Prediction Workshop. AIAA Paper 2004-0556.
7. Valarezo, Walter O.: Topics in High-Lift Aerodynamics. AIAA Paper 93-3136, July, 1993.
8. Klausmeyer, Steven M.; and Lin, John C.: Comparative Results From a CFD Challenge Over a 2D Three-Element High-Lift Airfoil. NASA TM-112858, May 1997.
9. Lindblad, I. A. A.; and de Cock, K. M. J.: CFD Prediction of Maximum Lift of a 2D High Lift Configuration. AIAA Paper 99-3180, June, 1999.
10. Jones, Kenneth M.; Biedron, Robert T.; and Whitlock; Mark: Application of a Navier-Stokes Solver to the Analysis of

- Multielement Airfoils and Wings Using Multizonal Grid Techniques. AIAA Paper 95-1855, June 1995.
11. Rumsey, C. L.; Gatski, S. X.; Ying, S. X.; and Bertelrud, A.: Prediction of High-Lift Flows Using Turbulent Closure Models. AIAA Journal, vol 36, no. 5, pp. 765-774, May 1998.
  12. Rumsey, Christopher L.; Lee-Rausch, Elizabeth M.; and Watson, Ralph D.: Three-Dimensional Effects on Multi-Element High Lift Computations. AIAA Paper 2002-0845, January 2002.
  13. Johnson, Paul L.; Jones, Kenneth M.; Madson, Michael D.: Experimental Investigation of a Simplified 3D High Lift Configuration in Support of CFD Validation. AIAA Paper 2000-4217; August 2000.
  14. Khorrami, Mehdi R.; Berkman, Mert E.; Li, Fei; and Singer, Bart A.: Computational Simulation of a Three-Dimensional High-Lift Wing. AIAA Paper 2002-2804; June 2002.
  15. McGinley, Catherine B.; Jenkins, Luther N.; and Watson, Ralph D.: 3-D High-Lift Flow-Physics Experiment – Transition Measurements. AIAA Paper 2005-5148; June 2005.
  16. Rogers, Stuart E.; Roth Karlin; and Nash, Steven M.: Validation of Computed High-Lift Flows with Significant Wind-Tunnel Effects. AIAA Journal, vol.39, pp 1884 - 1892; October 2001.
  17. Streett, Craig L.; Casper, Jay H.; Lockard, David P.; Khorrami, Mehdi R.; Stoker, Robert W.; Elkoby, Ronen; Wenneman, Wayne F.; and Underbrink, James R.: Aerodynamic Noise Reduction for High-Lift Devices on a Swept Wing Model. AIAA Paper 2006-212, January 2006.
  18. Slotnick, Jeffery P.; Hannon, Judith A.; and Chaffin, Mark: Overview of the First AIAA CFD High Lift Prediction Workshop (Invited). AIAA Paper 2011-862, January 2011.
  19. Rumsey, Christopher L.; Ying, Susan X.: Prediction of high lift: review of present CFD capability. Progress in Aeronautical Sciences, 2002, pp. 145-180.

20. Rumsey, C.; Long, M.; Stuever, R.; and Wayman, T.: Summary of the First AIAA CFD High Lift Prediction Workshop. AIAA Paper 2011-939, January 2011.
21. Rumsey, C. L.; Slotnick, J. P.; Long M.; Stuever, R. A.; and Wayman, T. R.: Summary of the First AIAA CFD High-Lift Prediction Workshop. *Journal of Aircraft*, Vol. 48, No. 6, November-December 2011, pp. 2068-2079.
22. Hannon, Judith A.; Trap Wing Experimental Summary, Geometry, and Repeatability. AIAA Presentation, AIAA 1<sup>st</sup> CFD High Lift Prediction Workshop, Chicago Illinois. June 2010.
23. Gentry, Carl L., Jr.; Quinto, P. Frank; Gatlin, Gregory M.; and Applin, Zachary T.: The Langley 14-by-22-Foot Subsonic Tunnel: Description, Flow Characteristics, and Guide for Users. NASA TP-3008, September 1990.
24. Vatsa, V. N.; Sanetrik, M. D.; and Parlette, E. B.: A Multigrid-Based Multiblock Flow Solver for Practical Aerodynamic Configurations. *Frontiers of Computational Fluid Dynamics*, Eds. D. A. Caughey and M. Hafez; Wiley and Sons, 1994, pp. 413-448.
25. Turkel, E.; and Vatsa, V. N.: Effect of Artificial Viscosity on Three-Dimensional Flow Solutions. *AIAA J.*, vol. 32, no. 1, January 1994, pp. 39-45.
26. Vatsa, V. N. and Wedan, B. W.: Development of a Multigrid Code for 3-D Navier-Stokes Equations and Its Application to a Grid-Refinement Study. *Computers and Fluids*, vol. 18, no. 4, 1990, pp. 391-403.
27. Rumsey, C. L. and Vatsa, V. N.: Comparison of Predictive Capabilities of Several Turbulence Models. *J. of Aircraft*, vol. 32, no. 3, May-June 1995, pp. 510-514.
28. Vatsa, V. N. and Wedan, B. W.: Effect of Sidewall Boundary Layer on a Wing in a Wind Tunnel. *Journal of Aircraft*, vol. 26, no. 2, February 1989, pp. 157-161.

29. Spalart, P. A. and Allmaras, S. R.: A One-Equation Turbulence Model for Aerodynamic Flows. AIAA Paper 92-439, January 1992.
30. Menter, F. R.: Zonal Two Equation K-W Turbulence Models for Aerodynamic Flows. AIAA Paper 93-2906, 1993.
31. Anderson, John D., Jr.: A History of Aerodynamics. Cambridge University Press, 1998, pp. 361 to 367.
32. Abbott, Ira H. and von DoenHoff, Albert E.: Theory of Wing Sections, Including a Summary of Airfoil Data. Dover Publications, Inc., 1959, pp. 188 to 246.
33. Loftin, Lawrence K.: Quest for Performance, The Evolution of Modern Aircraft. NASA Special Publication 468, pp. 271-275, 1985.
34. Raymer, Daniel P.: Aircraft Design: A Conceptual Approach. American Institute of Aeronautics and Astronautics, Inc., 1999, pp. 315-378.
35. Smith, A. M. O.: High-Lift Aerodynamics. J. of Aircraft, vol. 12, no. 6, June 1975, pp. 501-530.
36. Valarezo, Walter O.; Dominik, C. J.; McGhee, R. H.; Goodman, W. L.; and Paschal, K. B.: Multi-Element Airfoil Optimization for Maximum Lift at High Reynolds Numbers. AIAA Paper 91-3332, September 1991.
37. Milholen, William E. II; and Chokani, Ndaona: Computational Analysis of Simi-Span Model Test Techniques. NASA CR-4709, March 1996.
38. Hannon, Judith A.; Washburn, Anthony E.; Jenkins, Luther N.; and Watson, Ralph D.: Trapezoidal Wing Experimental Repeatability and Velocity Profiles in the 14- by 22-Foot Subsonic Tunnel (Invited). AIAA Paper 2012-0706, January 2012.
39. Roache, Patrick J.: Verification and Validation in Computational Science and Engineering. Hermosa Publishers, 1998, pp. 107-141.

40. Salas, Manuel D. and Atkins, Harold L.: On Problems Associated with Grid Convergence of Functionals. *Computers & Fluids*, Volume 8, Issue7, August 2009, pp. 1445-1454.
41. Chaffin, Mark S. and Pirzadeh, Shahyar: Unstructured Navier-Stokes High-Lift Computations on a Trapezoidal Wing. AIAA Paper 2005-5084, June, 2005.
42. Pandya, Mohagna J.; and Abdol-Hamid, Khaled S.: CFD Computations for a Generic High-Lift Configuration Using TetrUSS. AIAA Paper 2011-3008, June 2011.
43. Murayama, Mitsuhiro; Ito, Yasushi; and Tanaka, Kentaro; and Yamamoto, Kazoumi: Computational Studies of the NASA High-Lift Trap Wing Using Structured and Unstructured Grid Solvers. AIAA Paper 2012-2844, June 2012.
44. Cavallo, Peter A. and Feldman, Gregory M.: Quantification of Grid Refinement Effects for NASA High Lift Trap Wing Using Error Transport Model. AIAA Paper 2012-2847, June 2012.
45. Wiart, Ludovic and Moens, Frederic: Numerical Simulation of the NASA High-Lift Trap Wing with the elsA CFD Software. AIAA Paper 2012-2918, June 2012.
46. Eliasson, Peter; Peng, Shia-Hui, Hanifi, Ardeshir: Improving the Prediction for the NASA High-Lift Trap Wing Model. AIAA Paper 2011-867, January 2011.
47. Sclafani, Anthony J.; Slotnick, Jeffery P.; Vassberg, John C.; and Pulliam, Thomas H.: Extended OVERFLOW Analysis of the NASA Trap Wing Wind Tunnel Model. AIAA Paper 2012-2919, June 2012.
48. Rumsey, C. L. and Lee-Rausch, E. M.: NASA Trapezoidal Wing Computations Including Transition and Advanced Turbulence Modeling. AIAA Paper 2012-2843, June 2012.
49. Eliasson, Peter; Hanifi, Ardeshir; and Peng, Shia-Hui: Influence of Transition on High-Lift Prediction with the NASA Trap Wing Model. AIAA Paper 2011-3009, June 2011.

50. Steed, Robin G.F.: High-Lift CFD Simulations with an SST-Based Predictive Laminar to Turbulent Transition Model. AIAA Paper 2011-864, January 2011.
51. Fabiano, Enrico; Fares, Ehab; and Nolting, Swen: Unsteady Flow Simulation of Hi-Lift stall Hysteresis using a Lattice Boltzmann Approach. AIAA Paper 2012-2922, June 2012.

Table 1. Settings for the Leading-edge slat and Trailing-edge flap

Leading-edge slat	$\delta_s$	$g/c_{local}$	$h/c_{local}$
	30°	0.015	0.015
Trailing-edge flap	$\delta_f$	$g_f/c_{local}$	$o_f/c_{local}$
	25°	0.015	0.005

**Notes:**

Slat:

- Slat settings are specified in a vertical plane normal to the wing leading edge
- Slat height ( $h_s$ ) is measured relative to the surface hilite of the main wing element
- Slat gap ( $g_s$ ) is defined as the distance between the slat trailing edge and the surface of the main wing element
- For a point on the trailing edge of the slat, the chord used to normalize the slat gap and height is the local stream-wise chord of the cruise planform passing through the identical point on the trailing edge of the slat with the slat and flap in the cruise (stowed) position

Flap:

- Flap setting are specified in a plane aligned with the free-stream (the x-z plane)
- Flap gap ( $g_f$ ) is specified as the distance from the trailing edge of the wing cove to the nearest point on the flap
- Flap overlap ( $o_f$ ) is specified as the steam-wise distance from the leading edge of the flap to the trailing edge of the cove

Table 2. Grid blocks, points, and cells for the fine grid.

Grid Block	Dimension			No. Points	No. Cells
	I	J	K		
1	177	9	169	269217	236544
2	89	65	25	144625	135168
3	277	85	13	306085	278208
4	113	17	9	17289	14336
5	169	21	17	60333	53760
6	521	13	21	142233	124800
7	189	29	73	400113	379008
8	189	29	61	334341	315840
9	189	29	61	334341	315840
10	21	45	201	189945	176000
11	65	53	81	279045	266240
12	65	53	61	210145	199680
13	65	53	61	210145	199680
14	129	29	97	362877	344064
15	129	29	97	362877	344064
16	129	29	97	362877	344064
17	129	29	97	362877	344064
18	89	21	121	226149	211200
19	85	21	121	215985	201600
20	113	17	121	232441	215040
21	29	69	121	242121	228480
22	9	25	121	27225	23040
23	145	29	97	407885	387072
24	141	29	97	396633	376320
25	141	29	97	396633	376320
26	145	29	97	407885	387072

Grid Block	Dimension			No. Points	No. Cells
	I	J	K		
27	21	57	193	231021	215040
28	29	21	193	117537	107520
29	65	29	193	363805	344064
30	109	29	73	230753	217728
31	109	29	61	192821	181440
32	109	29	61	192821	181440
33	85	21	77	137445	127680
34	33	33	77	83853	77824
35	9	49	77	33957	29184
36	21	81	77	130977	121600
37	245	21	77	396165	370880
38	129	29	97	362877	344064
39	125	29	97	351625	333312
40	125	29	97	351625	333312
41	129	29	97	362877	344064
42	201	25	37	185925	172800
43	473	13	57	350493	317184
44	473	13	61	375089	339840
45	473	13	61	375089	339840
46	369	73	9	242433	211968
TOTAL				11971510	11188288

Table 3. Wind-Tunnel Force-and-Moment Data

$\alpha$ , degrees	$M_\infty$	$C_L$	$C_D$	$C_m$	$x_m$ , inches	$z_m$ , inches
-3.936	0.2038	0.2838	0.1139	-0.2200	34.342	0.000
-2.085	0.2033	0.4873	0.1089	-0.2665	34.342	0.000
-0.096	0.2021	0.8223	0.1182	-0.3695	34.342	0.000
2.084	0.2022	1.1944	0.1442	-0.4687	34.342	0.000
4.009	0.2027	1.3578	0.1741	-0.4828	34.342	0.000
6.029	0.2018	1.5261	0.2075	-0.4964	34.342	0.000
8.026	0.2013	1.6804	0.2420	-0.5013	34.342	0.000
10.004	0.2019	1.8240	0.2783	-0.5035	34.342	0.000
12.020	0.2016	1.9701	0.3187	-0.5044	34.342	0.000
13.969	0.2017	2.1027	0.3614	-0.5042	34.342	0.000
15.928	0.2022	2.2416	0.4071	-0.5061	34.342	0.000
17.970	0.2015	2.3744	0.4549	-0.5056	34.342	0.000
18.916	0.2025	2.4347	0.4777	-0.5053	34.342	0.000
19.937	0.2029	2.4997	0.5030	-0.5056	34.342	0.000
20.925	0.2016	2.5603	0.5275	-0.5055	34.342	0.000
21.999	0.2023	2.6243	0.5543	-0.5028	34.342	0.000
22.914	0.2029	2.6789	0.5769	-0.4993	34.342	0.000
24.014	0.2031	2.7460	0.6062	-0.4960	34.342	0.000
25.005	0.2025	2.7986	0.6313	-0.4916	34.342	0.000
25.977	0.2028	2.8460	0.6546	-0.4866	34.342	0.000
26.941	0.2025	2.8885	0.6788	-0.4811	34.342	0.000
27.908	0.2022	2.9310	0.7017	-0.4759	34.342	0.000
28.970	0.2023	2.9652	0.7225	-0.4645	34.342	0.000
29.877	0.2027	2.9884	0.7401	-0.4528	34.342	0.000
30.910	0.2029	3.0096	0.7585	-0.4388	34.342	0.000
31.319	0.2028	3.0161	0.7654	-0.4325	34.342	0.000
31.922	0.2034	3.0242	0.7767	-0.4225	34.342	0.000
32.587	0.2028	3.0284	0.7855	-0.4112	34.342	0.000
32.993	0.2029	3.0306	0.7917	-0.4031	34.342	0.000
33.665	0.2031	3.0283	0.7982	-0.3856	34.342	0.000
33.894	0.2029	3.0259	0.7994	-0.3793	34.342	0.000
34.452	0.2033	3.0143	0.8054	-0.3606	34.342	0.000
34.858	0.2034	2.9884	0.8112	-0.3411	34.342	0.000
35.401	0.2060	2.2707	0.8210	-0.2463	34.342	0.000
35.996	0.2054	2.2482	0.8302	-0.2324	34.342	0.000

Note: These data from the TrapWing web site have been corrected to free-air conditions. The values of  $C_D$  on the site were updated on July 1, 2009. Previously, they were incorrect due to an error in applying wind-tunnel-boundary corrections. See reference 18.

Table 4. Computational Cases Run

Case	$\alpha$ , degrees	Grid (No. of Points)	Turbulence Model	Numerical Precision (BITS)	No. of Multigrid Cycles Run
1	10.004	12.0M	S-A 1-equa.	32	900
2	10.050	12.0M	S-A 1-equa.	32	900
3	14.000	12.0M	S-A 1-equa.	32	1135
4	19.937	12.0M	S-A 1-equa.	32	1150
5	27.908	12.0M	S-A 1-equa.	32	1425
6	28.120	12.0M	S-A 1-equa.	32	1325
7	29.877	12.0M	S-A 1-equa.	32	1325
8	32.993	12.0M	S-A 1-equa.	32	1485
9	33.980	12.0M	S-A 1-equa.	32	1775
10	34.858	12.0M	S-A 1-equa.	32	1625
7-DP	29.877	12.0M	S-A 1-equa.	64	1305
7-SST	29.877	12.0M	SST 2-equa.	32	1600
1-CG	10.004	1.5M	S-A 1-equa.	32	2000
7-CG	29.877	1.5M	S-A 1-equa.	32	2000
1a-MG	10.852	6.0M	S-A 1-equa.	64	900
3-MG	14.000	6.0M	S-A 1-equa.	64	2000
7-MG	29.877	6.0M	S-A 1-equa.	64	1700

Note:

S-A 1-equa. = Spalart-Allmaras 1-equation turbulence model

SST 2-equa. = Mentor's SST 2-equation turbulence model

Table 5. Calculated Forces and Moments with Numerical Convergence

Case	$\alpha$ , degrees	Calculated Values of $C_L$ , $C_{D,v}$ , $C_D$ , and $C_m$ & The Change in $C_L$ , $C_D$ , and $C_m$ in the Last 100 Multigrid Cycles						
		$C_L$	$\Delta C_L$	$C_{D,v}$	$C_D$	$\Delta C_D$	$C_m$	$\Delta C_m$
1	10.004	1.806	0.055%	0.0124	0.2613	0.078%	-0.4818	0.124%
2	10.050	1.810	0.000%	0.0124	0.2622	0.076%	-0.4819	0.083%
3	14.000	2.078	0.000%	0.0126	0.3365	0.030%	-0.4778	0.042%
4	19.937	2.447	0.041%	0.0127	0.4629	0.022%	-0.4691	0.064%
5	27.908	2.790	0.036%	0.0124	0.6311	0.000%	-0.4131	0.097%
6	28.120	2.796	0.071%	0.0124	0.6346	0.047%	-0.4109	0.024%
7	29.877	2.845	0.000%	0.0122	0.6693	0.000%	-0.3932	0.127%
8	32.993	2.867	0.000%	0.0116	0.7238	0.028%	-0.3406	0.088%
9	33.980	2.664	0.075%	0.0110	0.7593	0.026%	-0.2669	0.262%
10	34.858	2.537	0.118%	0.0106	0.7870	0.063%	-0.2359	0.297%
7-DP	29.877	2.845	0.035%	0.0122	0.6693	0.090%	-0.3937	0.025%
7-SST	29.877	2.788	0.036%	0.0118	0.6483	0.015%	-0.3733	0.000%
1-CG	10.004	1.730	0.058%	0.0131	0.2666	0.000%	-0.4668	-0.021%
7-CG	29.877	2.542	0.000%	0.0118	0.6457	0.002%	-0.3362	0.000%
1a-MG	10.852	1.803	0.222%	0.0127	0.2687	0.186%	data lost	data lost
3-MG	14.000	2.038	0.098%	0.0130	0.3399	0.088%	data lost	data lost
7-MG	29.877	2.845	0.035%	0.0122	0.6811	0.029%	data lost	data lost

Table 6. Grid Convergence Study

Grid, no. of cells	Angle of attack, $\alpha$							
	10.004°		10.852°		14.000°		29.877°	
	$C_L$	$C_D$	$C_L$	$C_D$	$C_L$	$C_D$	$C_L$	$C_D$
1.5x10 <sup>6</sup>	1.730	0.2666	no data	no data	no data	no data	2.542	0.6457
6.0x10 <sup>6</sup>	no data	no data	1.803	0.2687	2.038	0.3399	2.845	0.6811
12.0x10 <sup>6</sup>	1.806	0.2613	no data	no data	2.078	0.3365	2.845	0.6693
<p>Note: Due to the resources available, a mathematically formal grid study could not be conducted. These cases were run in order to make an engineering assessment of grid convergence. Refer to the section “Grid convergence” under “Results” in the text.</p>								

Table 7. Comparison of Computed and Experimental Forces & Moments.

$C_L$ versus $\alpha$				
$\alpha$ , degrees	$C_{L,numerical}$	$C_{L,experimental}$	$\Delta C_L =$ $C_{L,numerical} - C_{L,experimental}$	$\Delta C_L / C_{L,experimental}$
10.004	1.806	1.824	-0.018	-0.99%
14.000	2.078	2.104	-0.027	-1.28%
19.937	2.447	2.500	-0.053	-2.11%
27.908	2.790	2.889	-0.099	-3.41%
28.120	2.796	2.938	-0.142	-4.83%
29.877	2.845	2.988	-0.143	-4.80%
32.993	2.867	3.031	-0.164	-5.40%

Note:  $C_{L,experimental}$  linearly interpolated from Table 3 (experimental data) for constant  $\alpha$ .

$C_D$ versus $\alpha$				
$\alpha$ , degrees	$C_{D,numericalD}$	$C_{D,experimental}$	$\Delta C_D =$ $C_{D,numerical} - C_{D,experimental}$	$\Delta C_D / C_{D,experimental}$
10.004	0.2613	0.2783	-0.0170	-6.11%
14.000	0.3365	0.3621	-0.0256	-7.08%
19.937	0.4629	0.5030	-0.0401	-7.97%
27.908	0.6310	0.7017	-0.0706	-10.06%
28.120	0.6346	0.7058	-0.0712	-10.09%
29.877	0.6693	0.7401	-0.0708	-9.57%
32.993	0.7238	0.7917	-0.0679	-8.58%

Note:  $C_{D,experimental}$  linearly interpolated from Table 3 (experimental data) for constant  $\alpha$ .

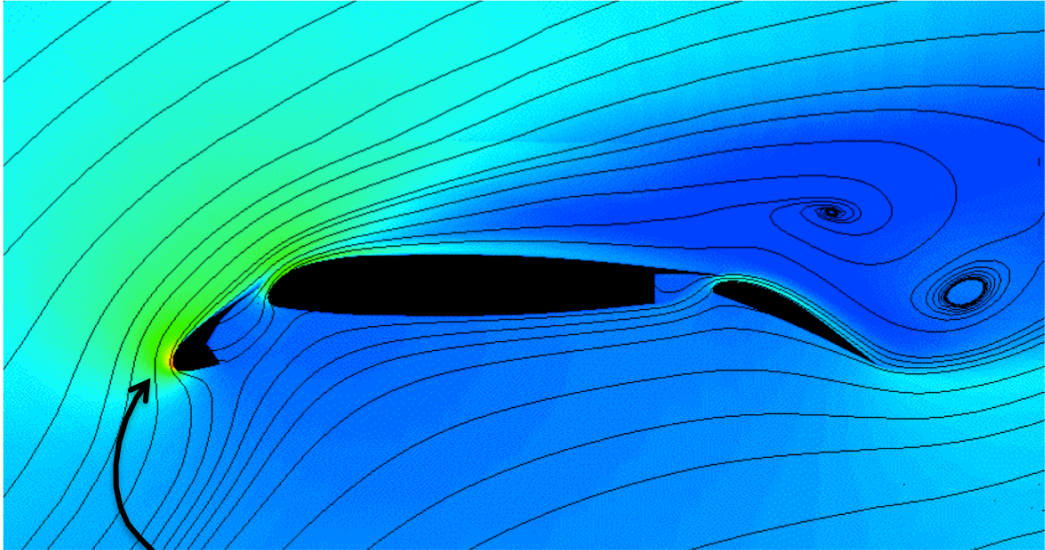
Table 7. Concluded.

$C_D$ versus $C_L$				
$C_L$	$C_{D,numerical}$	$C_{D,experimental}$	$\Delta C_D =$ $C_{D, numerical} - C_{D, experimental}$	$\Delta C_D / C_{D,experimental}$
1.806	0.2613	0.2737	-0.0124	-4.55%
2.078	0.3365	0.3559	-0.0194	-5.45%
2.447	0.4629	0.4825	-0.0196	-4.06%
2.790	0.6311	0.6272	0.0039	0.62%
2.796	0.6346	0.6301	0.0045	0.72%
2.845	0.6693	0.6541	0.0152	2.32%
2.867	0.7238	0.6666	0.0572	8.59%

Note:  $C_{D, experimental}$  linearly interpolated from Table 3 (experimental data) for constant  $C_L$ .

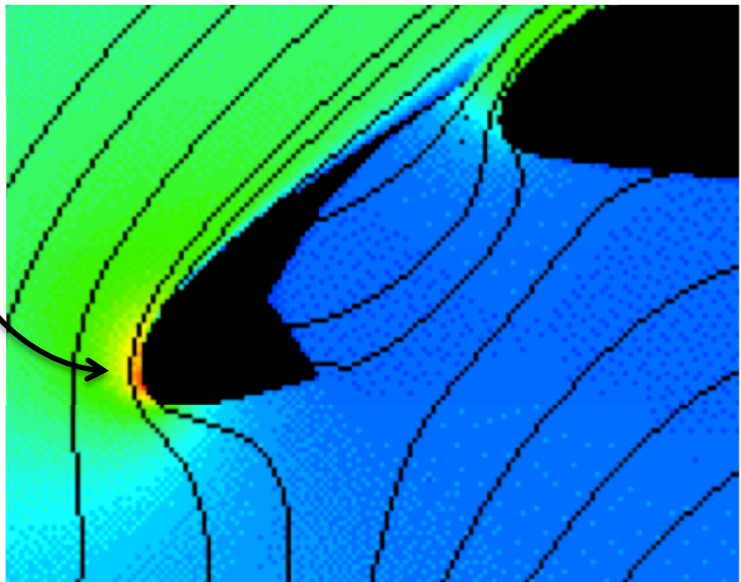
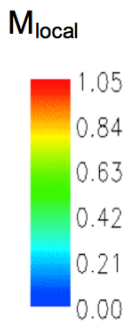
$C_m$ versus $\alpha$				
$\alpha,$ degrees	$C_{m,numerical}$	$C_{m,experimental}$	$\Delta C_m =$ $C_{m, numerical} - C_{m, experimental}$	$\Delta C_m / C_{m,experimental}$
10.004	-0.4818	-0.5035	0.0217	-4.31%
14.000	-0.4778	-0.5042	0.0264	-5.24%
19.937	-0.4691	-0.5056	0.0365	-7.22%
27.908	-0.4130	-0.4759	0.0628	-13.20%
28.120	-0.4109	-0.4736	0.0627	-13.24%
29.877	-0.3932	-0.4528	0.0596	-13.16%
32.993	-0.3406	-0.4031	0.0625	-15.50%

Note:  $C_{m, experimental}$  linearly interpolated from Table 3 (experimental data) for constant  $\alpha$ .



(a) Overall features

Possible transonic flow



(b) Details at the leading-edge slat

Figure 1. Features of multi-element high-lift flows. ( $M_\infty = 0.2$ ,  $\alpha \approx 34^\circ$ )

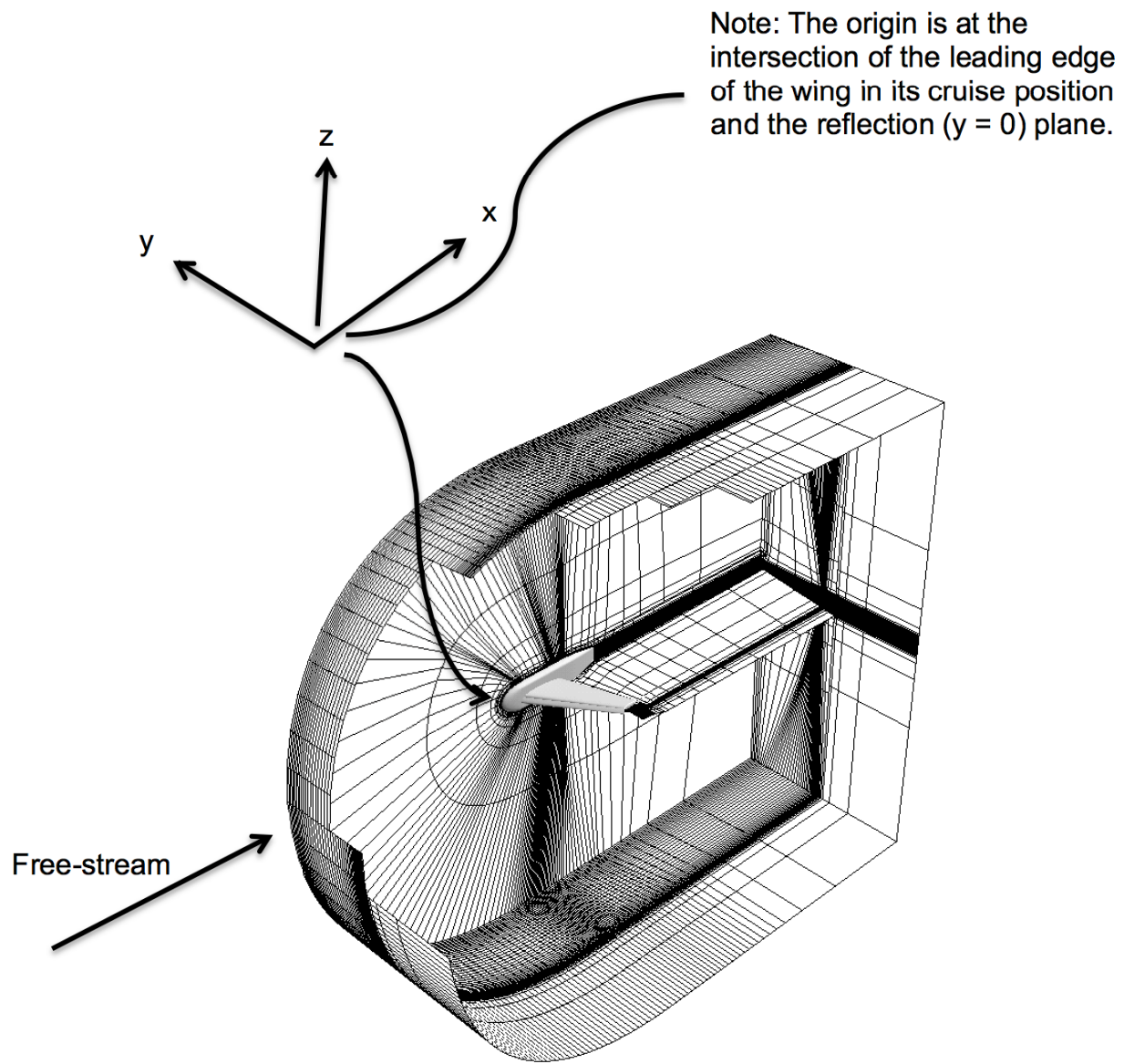
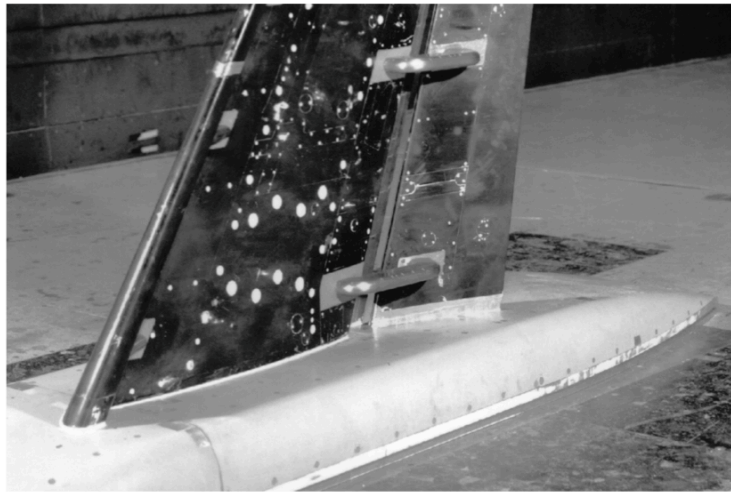


Figure 2. Cutaway view of the computational domain and grid.  
(Selected mesh planes deleted for clarity.)



(a) Full wing-body (top view)



(b) Wing-body juncture (bottom view)

Figure 3. Experimental model installed in the NASA Langley 14x22 Foot Wind Tunnel.



Slat and flap in stowed (cruise) positions

( Note: This configuration not investigated, for reporting wing dimensions only)



Slat and flap in deployed (high-lift landing) positions

Configuration Dimensions (Quoted with the slat and flap in the stowed (cruise) positions)	
Wing semi-span: $b/2$	85.1 inches
Mean aerodynamic chord: $\bar{c}$	39.6 inches
Semi-span wing area: $S$	3172.03 inches <sup>2</sup>
Aspect ratio: $AR = b/\bar{c}$	4.56
Leading edge sweep	33.0°
Quarter chord sweep	30.0°
Wing taper ratio	0.4
Slat chord	5.0 inches
Flap chord ratio: $c_f/c_{local}$	0.3
Wing-root thickness ratio: $(t/c)$ at root	0.121
Wing-tip thickness ratio: $(t/c)$ at tip	0.1
Body pod length (x direction)	118.72 inches
Body pod height (z direction)	27.961 inches
Body pod thickness (y direction)	5.95 inches
Leading edge of body pod (x,y,z)	-17.70, 0.0, 0.0 (all in inches)
Moment center (x,y,z)	34.342, 0.0, 0.0 (all in inches)
Slat bracket locations (experimental model only): $y/(b/2)$	0.13, 0.33, 0.47, 0.64, 0.77, 0.94 (all in inches)
Flap bracket locations (experimental model only): $y/(b/2)$	0.13, 0.37, 0.61, 0.80 (all in inches)

Note: The zero reference point for the configuration is defined as the intersection of the leading edge of the wing in the cruise configuration with the  $y = 0$  plane.

Figure 4. Model dimensions with sketches of a typical airfoil in both the cruise (stowed) and landing (deployed) configurations.

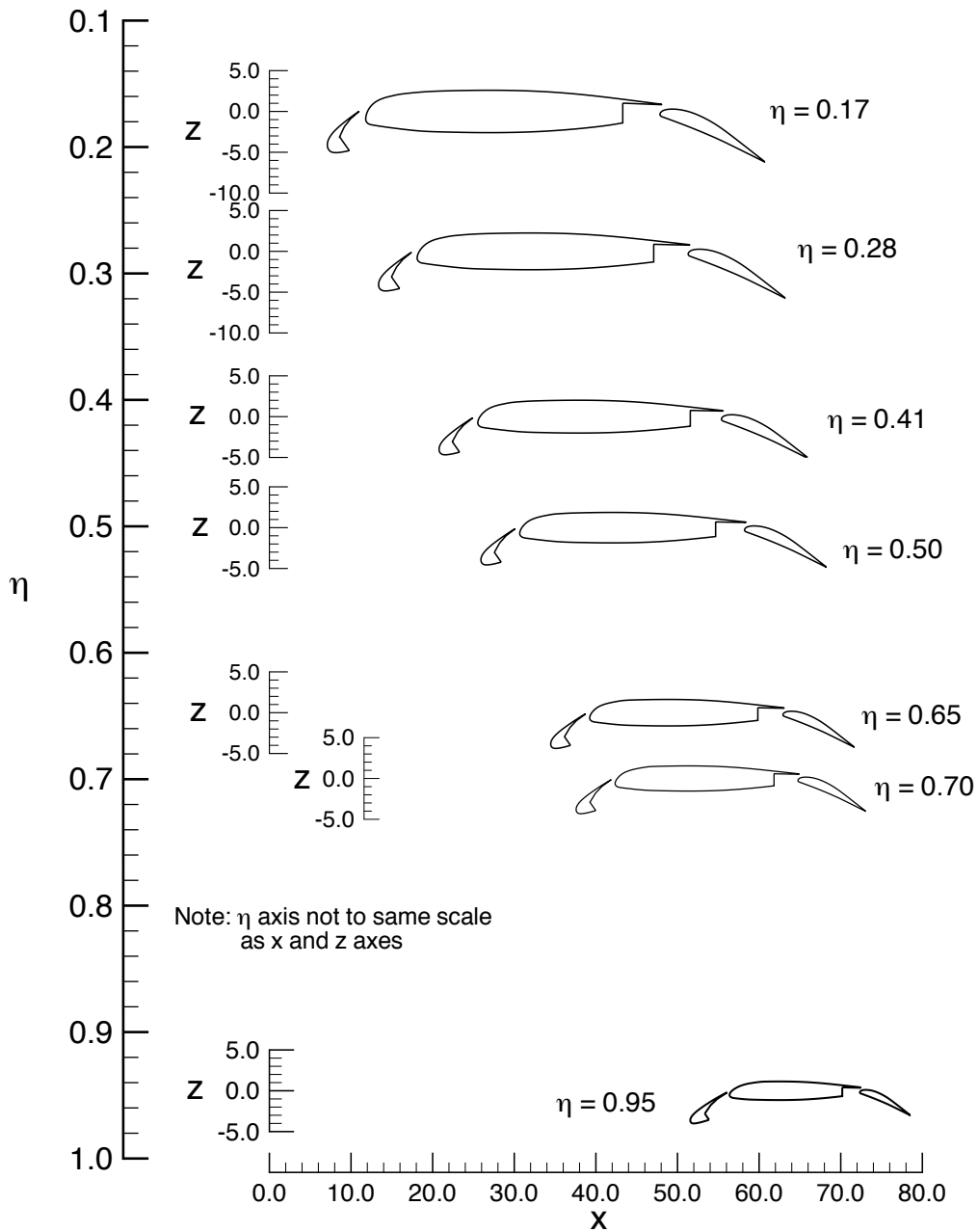


Figure 5. Airfoils at selected span stations with the slat and flap deployed (i.e., with the wing in the configuration for the present investigation).

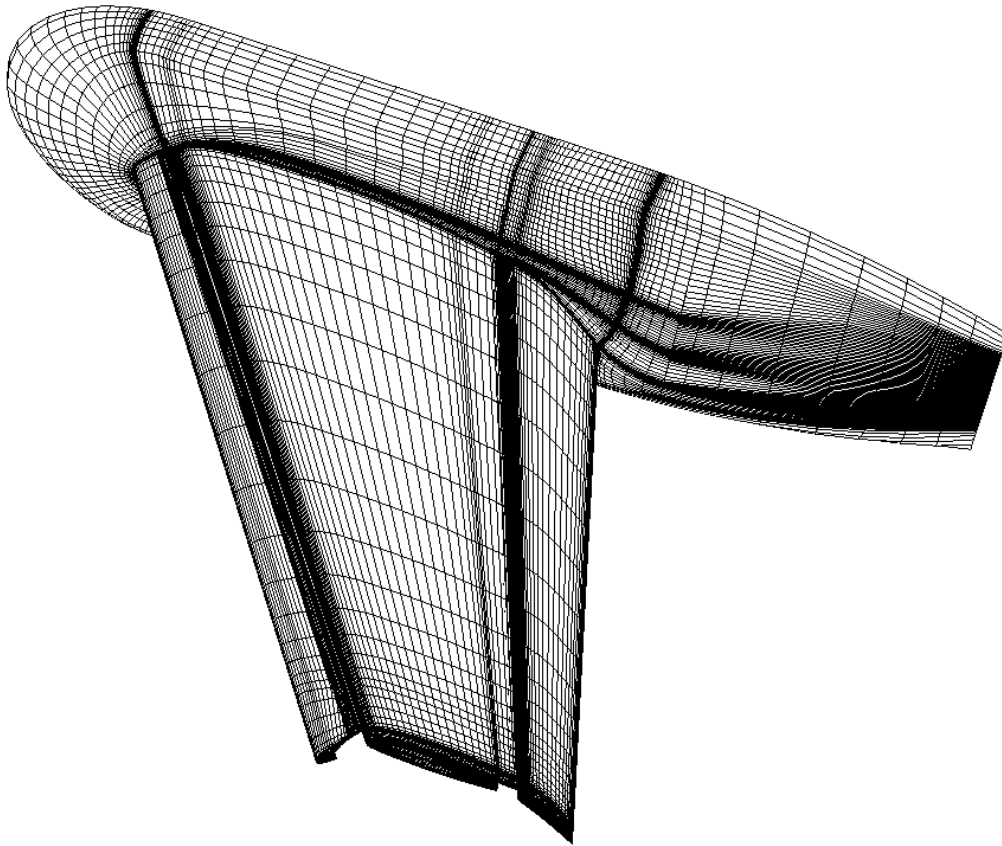
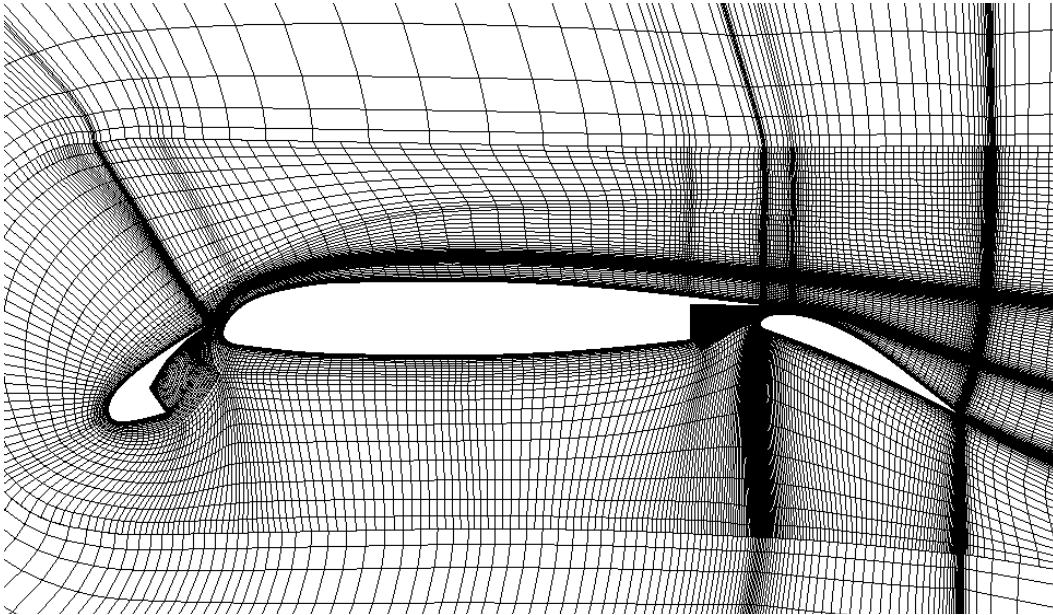
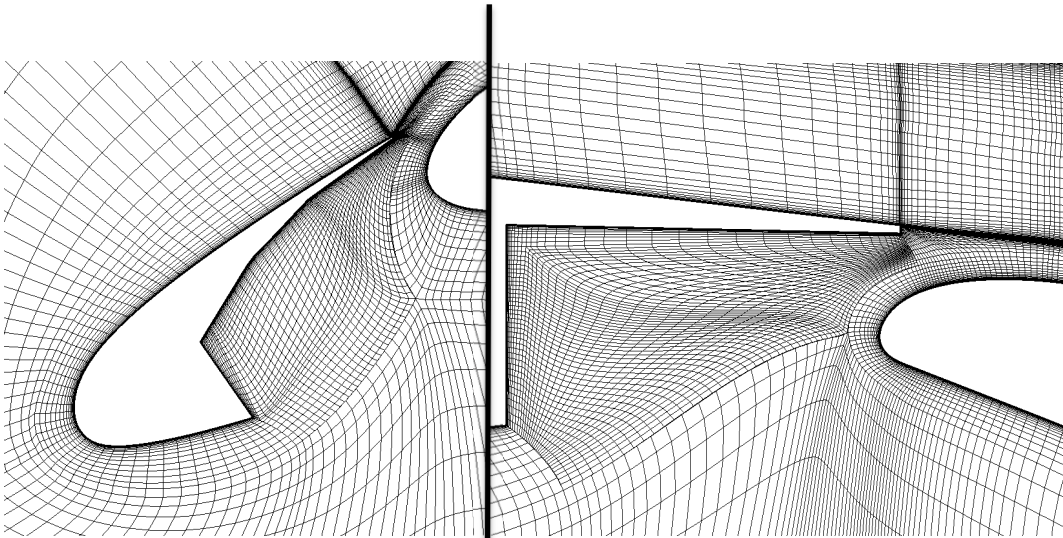


Figure 6. Surface grid mesh. (Every other line deleted for clarity.)



(a) Complete wing.



(b) Details in the vicinity of the leading-edge slat.

(c) Details in the vicinity of the wing cove.

Figure 7. Typical grid mesh in the vicinity of the wing. (Vertical cut)

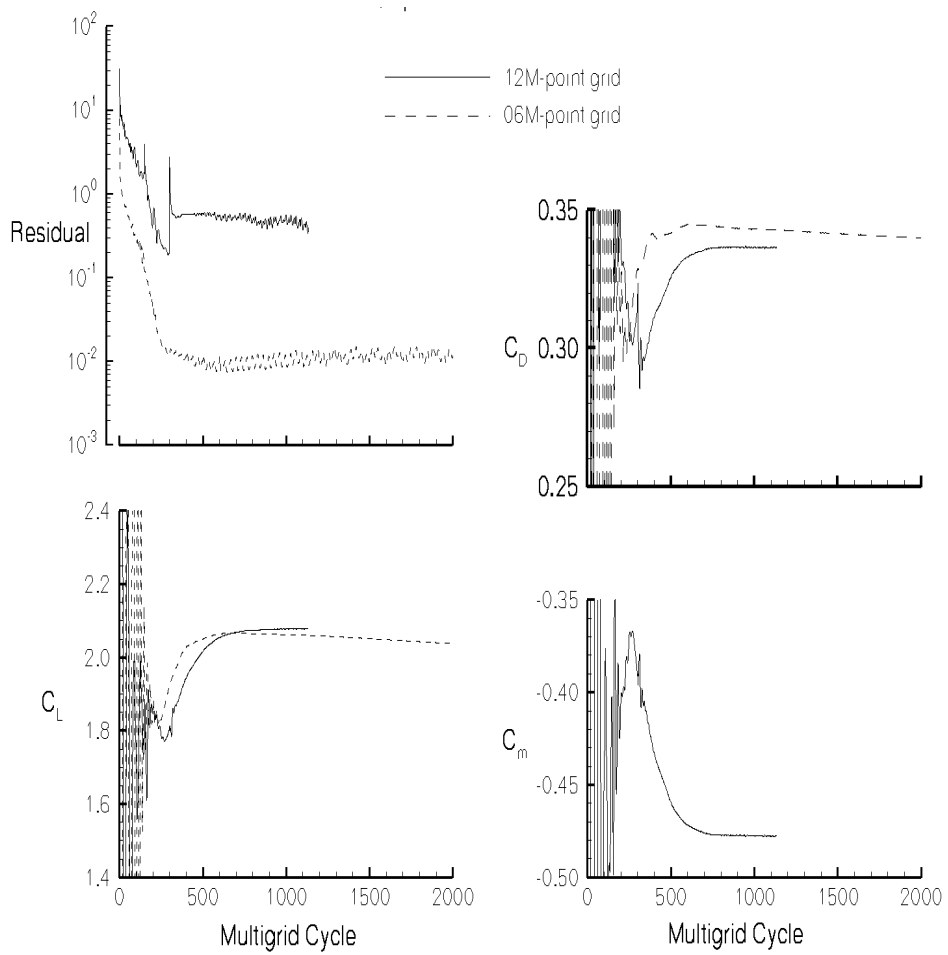
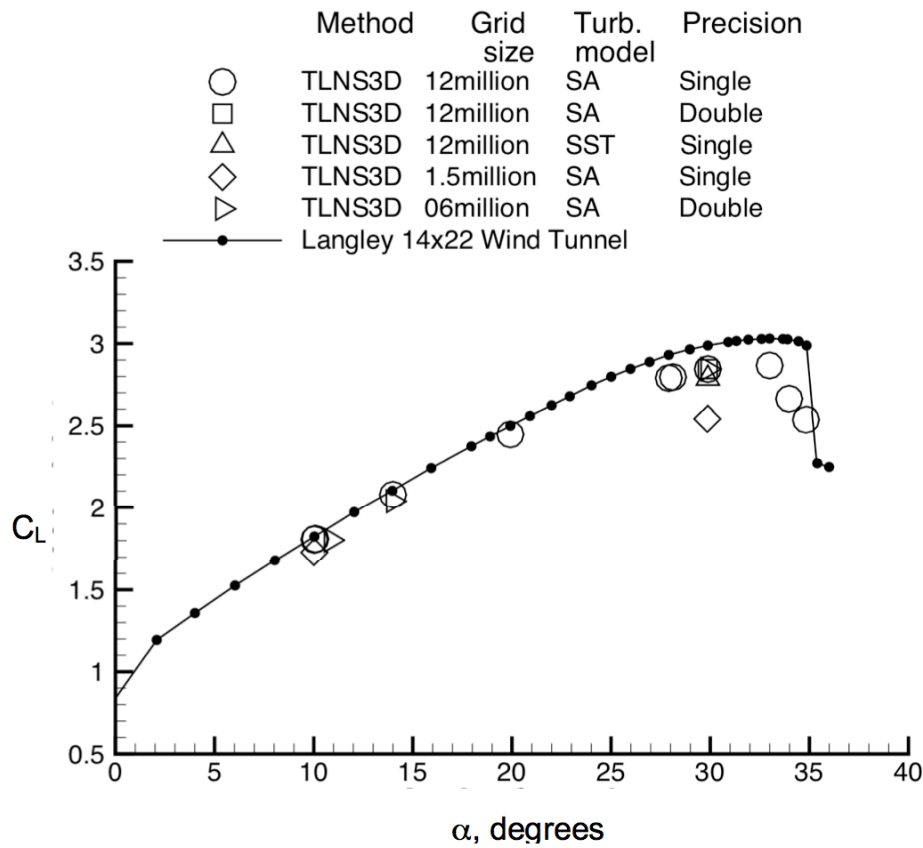
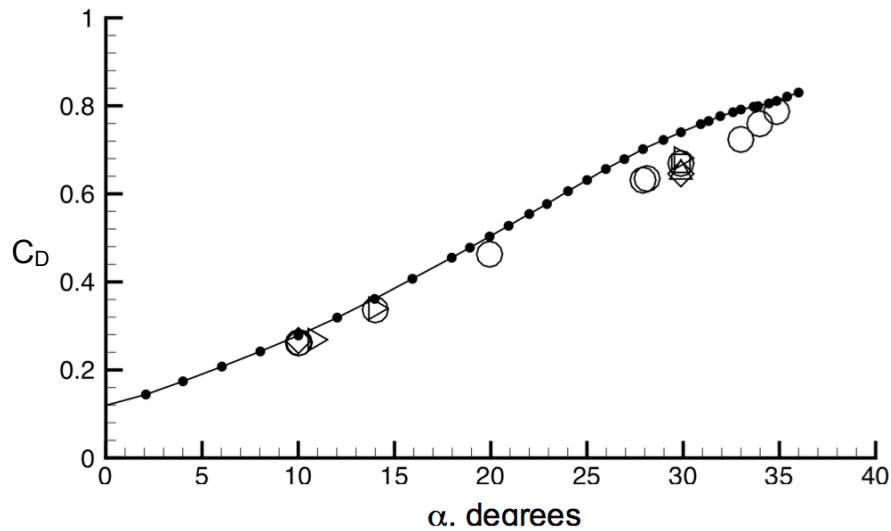


Figure 8. Sample convergence history. ( $\alpha = 14.000^\circ$ )



(a)  $C_L$  versus  $\alpha$



(b)  $C_D$  versus  $\alpha$

Figure 9. Force and moment plots. (For the experimental data, the balance accuracies in terms of aerodynamic coefficients were approximately: normal direction,  $\pm 0.0024$ ; axial direction,  $\pm 0.0017$ ; and pitching moment,  $\pm 0.00095$ .)

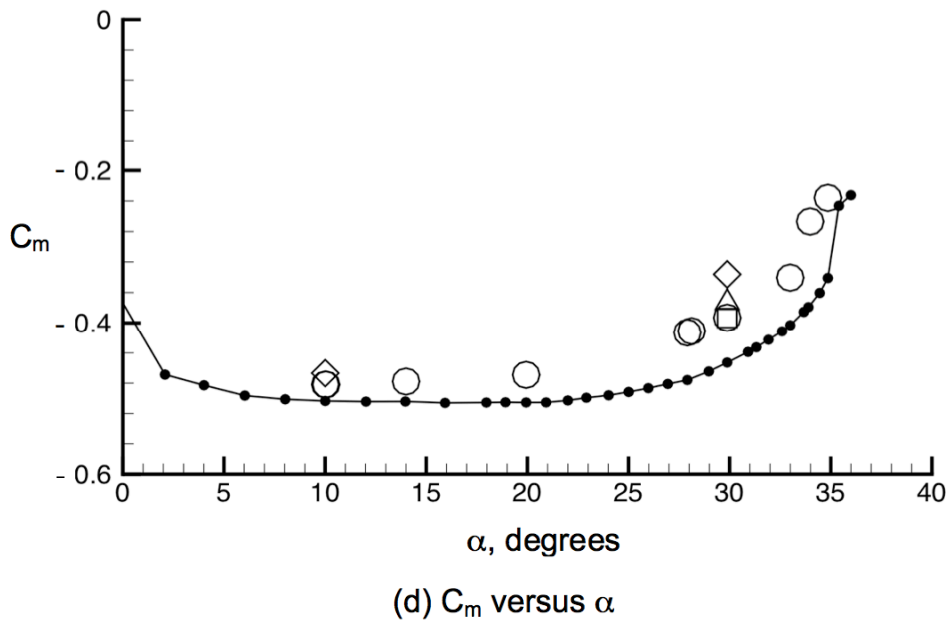
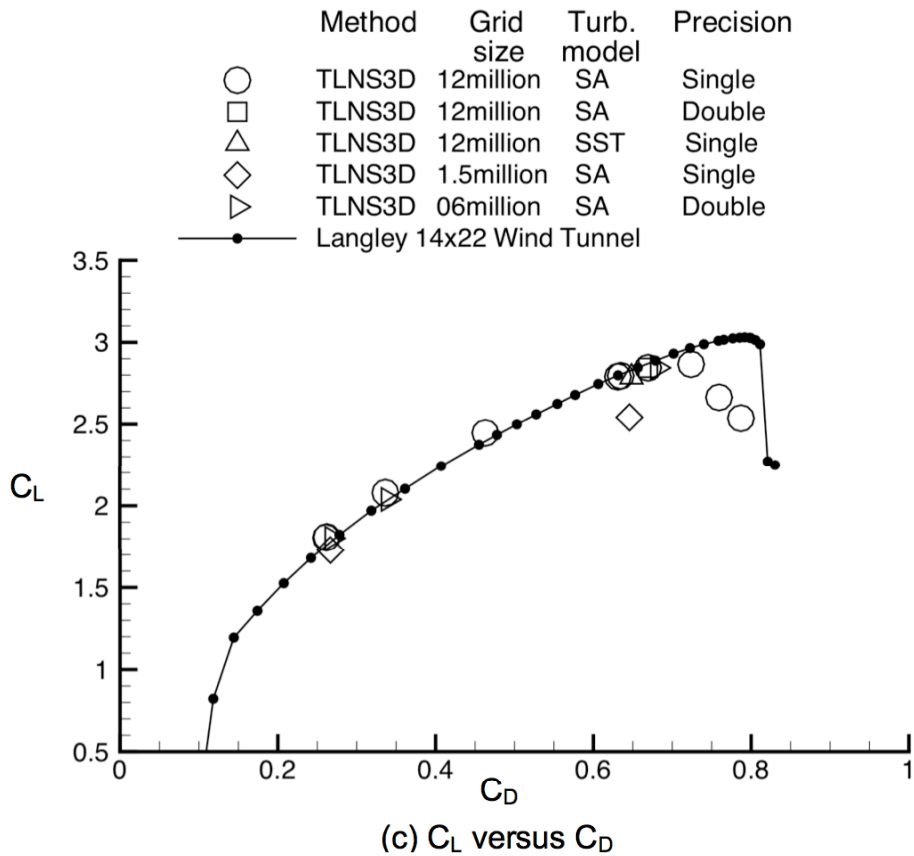
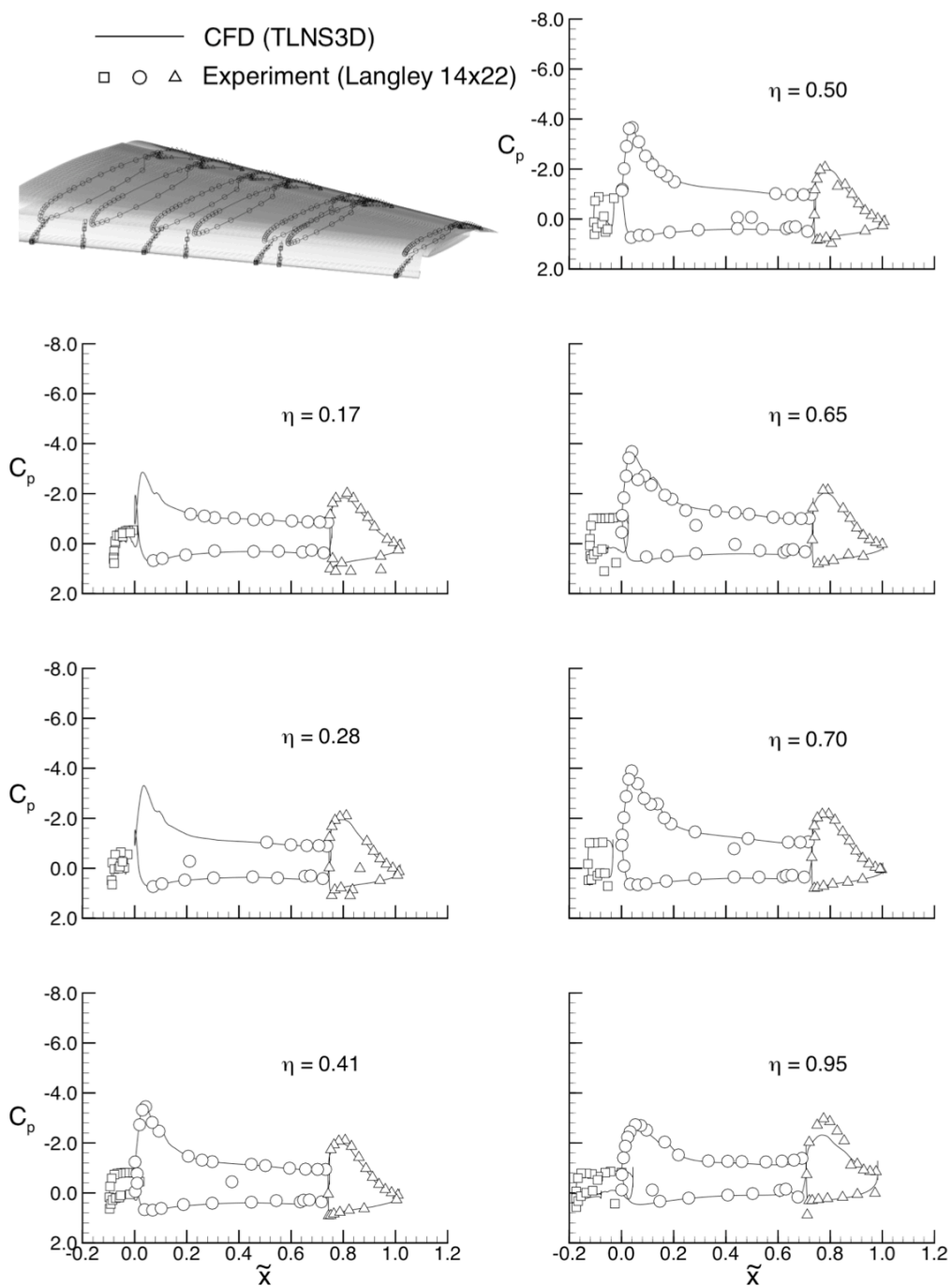
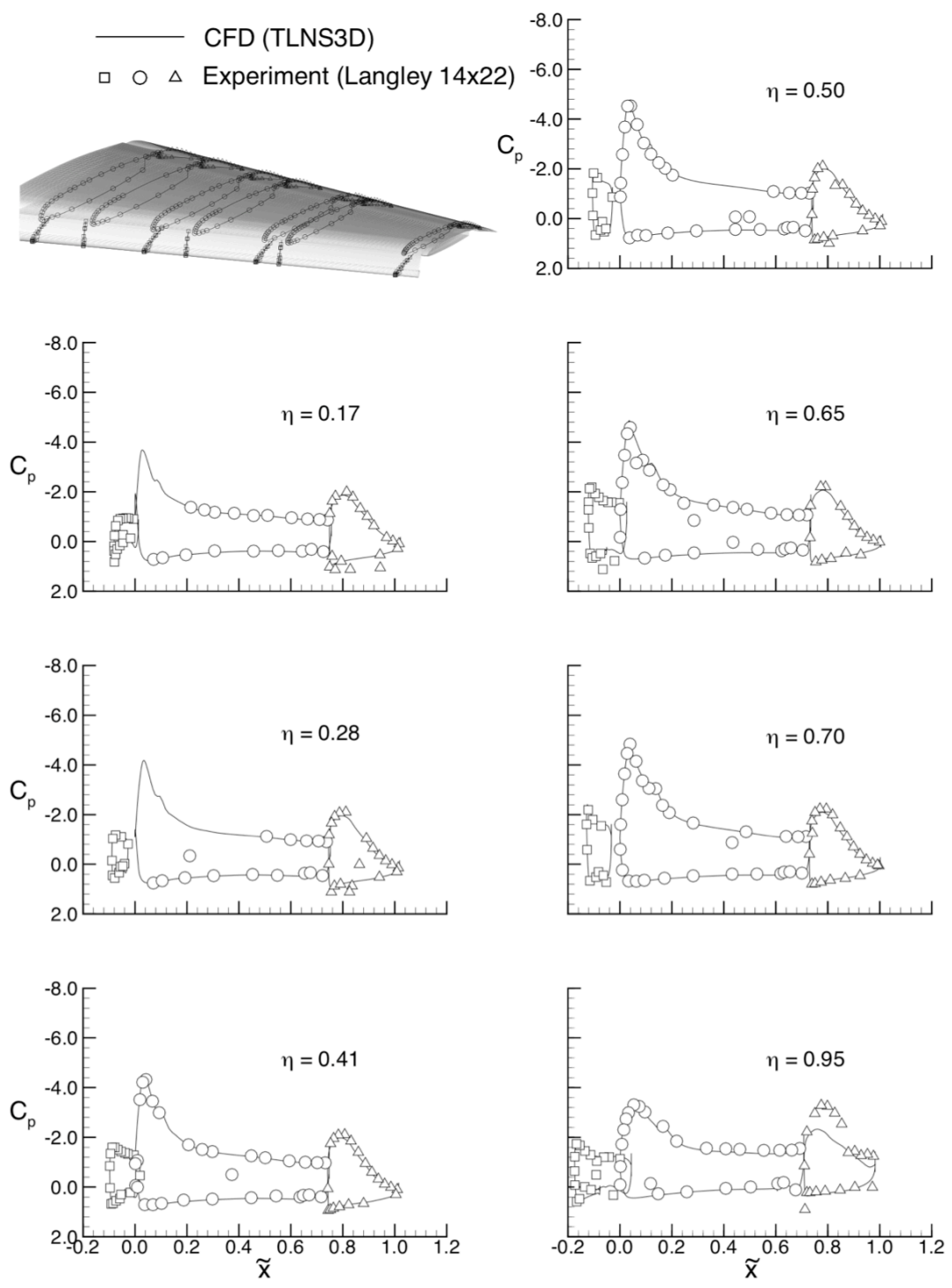


Figure 9. Concluded.



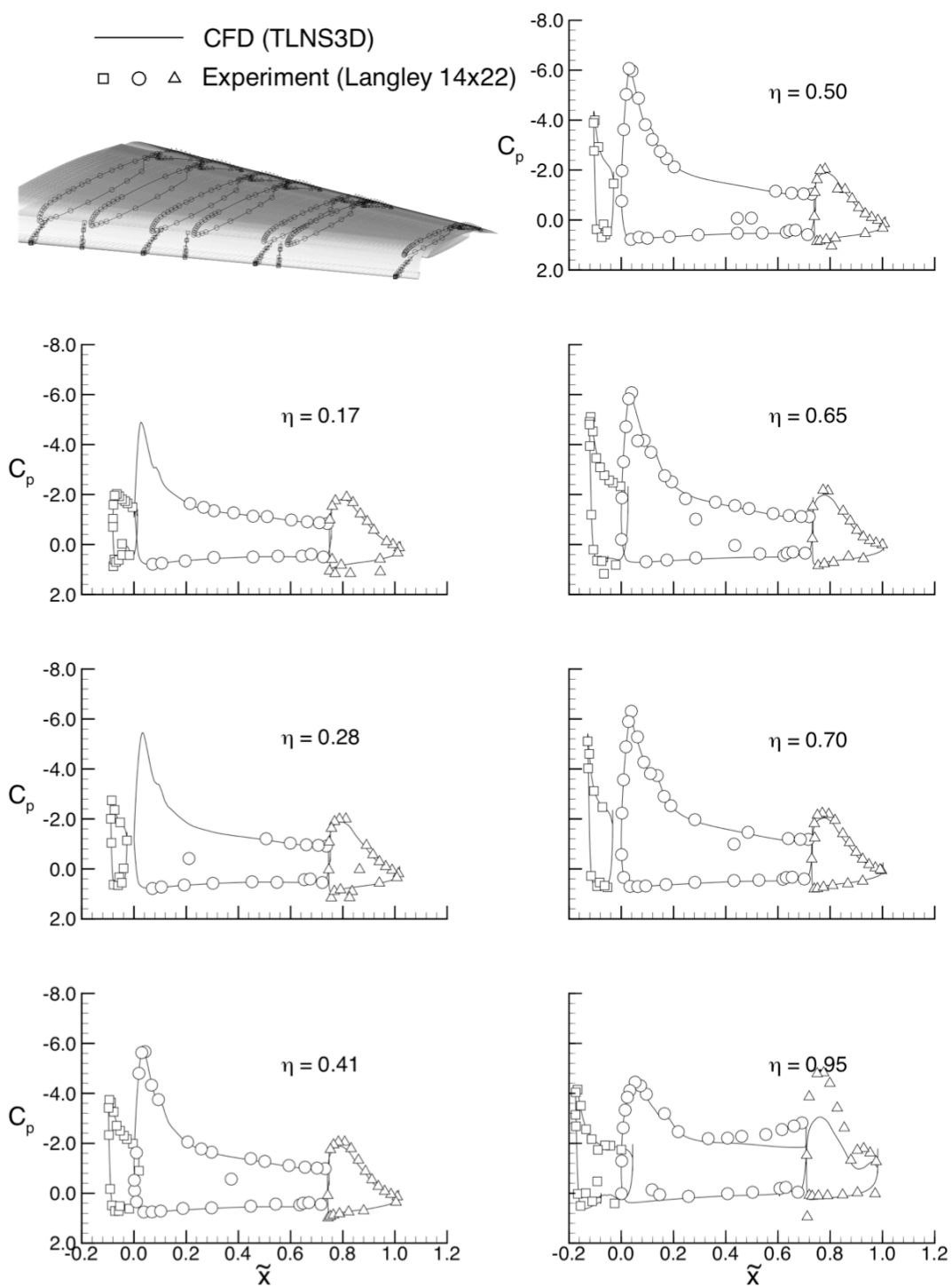
(a)  $\alpha = 10.004^\circ$

Figure 10. Pressure coefficient distributions on the wing. (CFD calculations were made with the Spalart-Almaras turbulence model.)



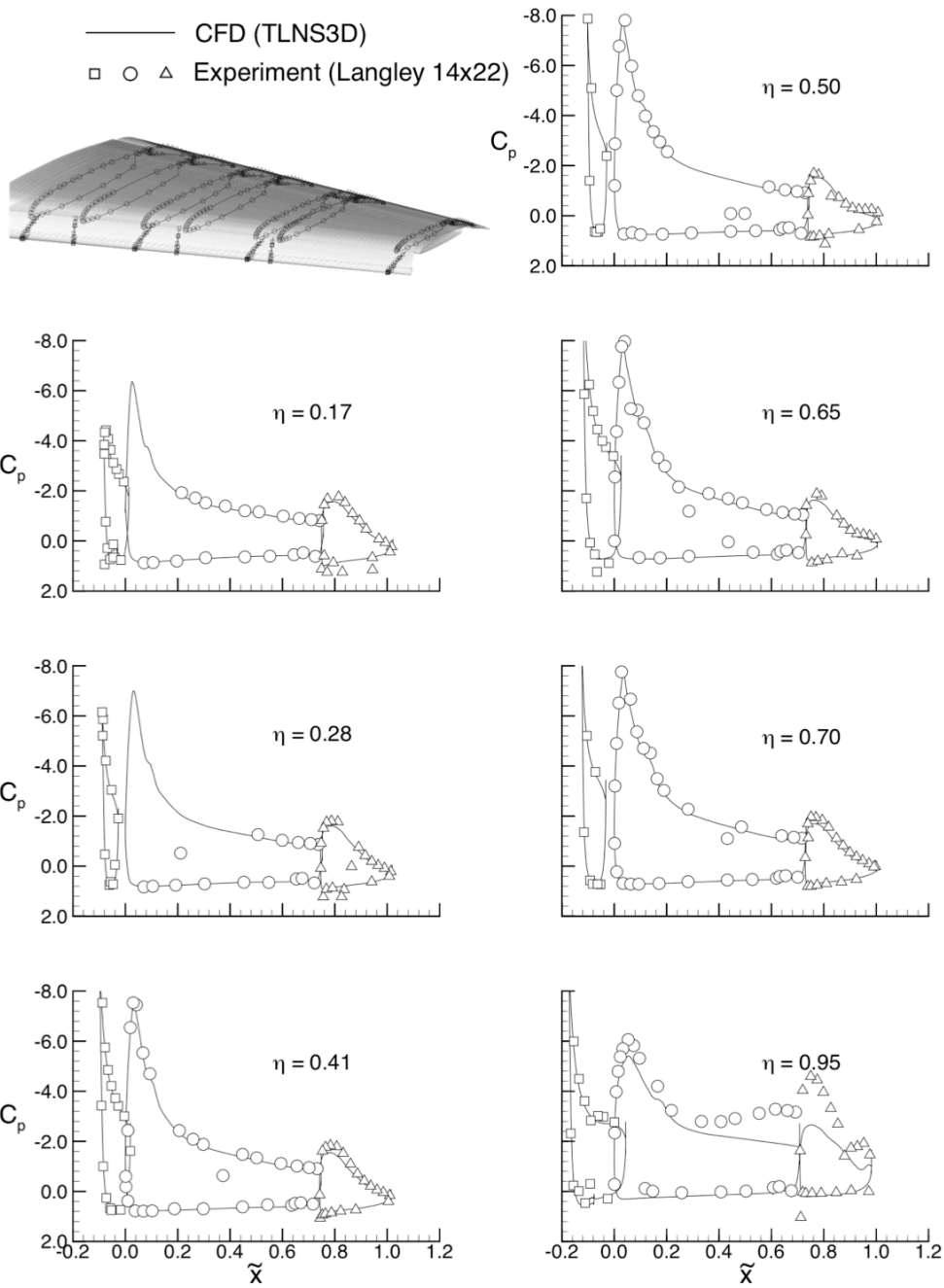
(b)  $\alpha = 14.000^\circ$

Figure 10. Continued.



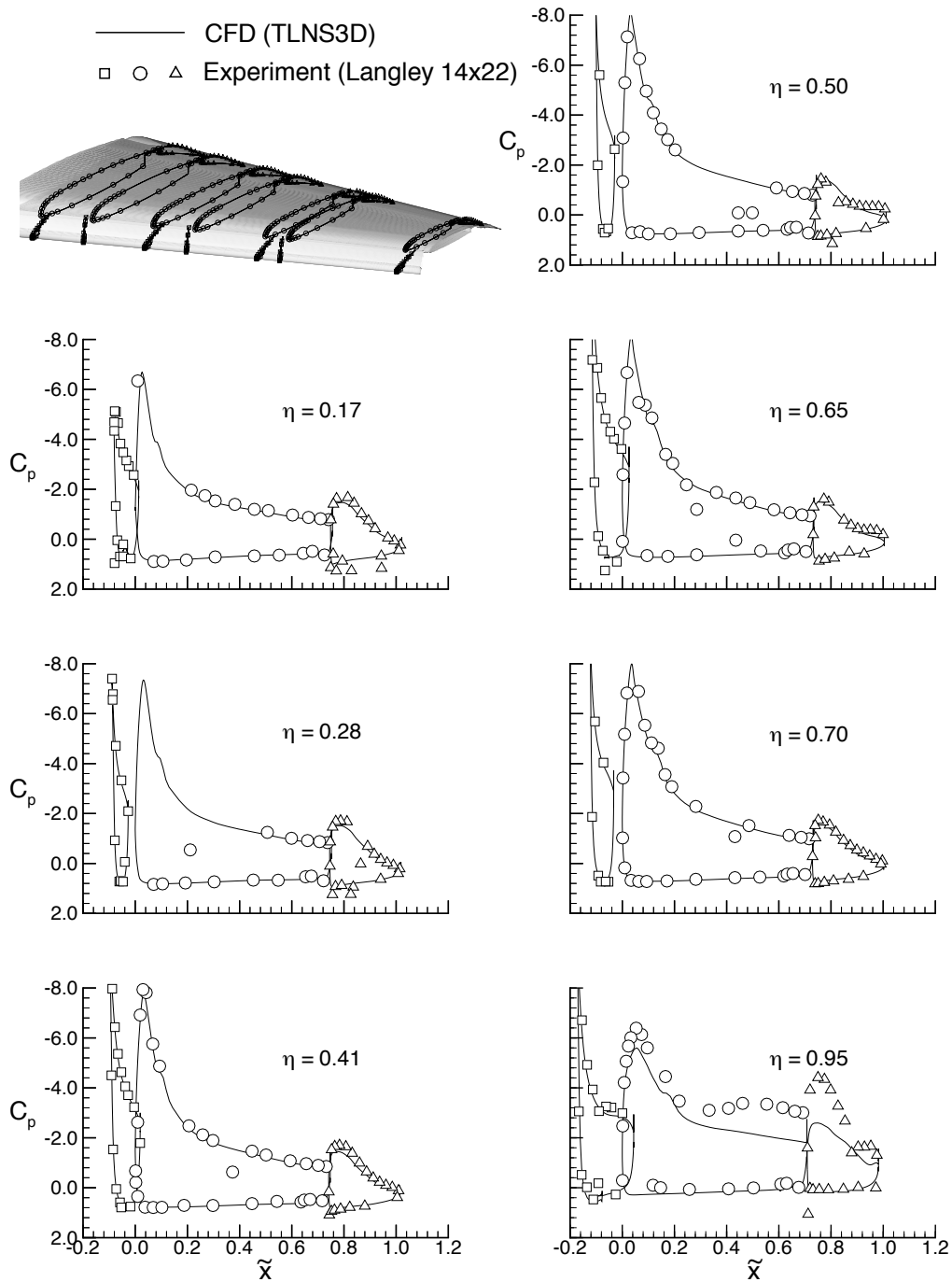
(c)  $\alpha = 19.937^\circ$

Figure 10. Continued.



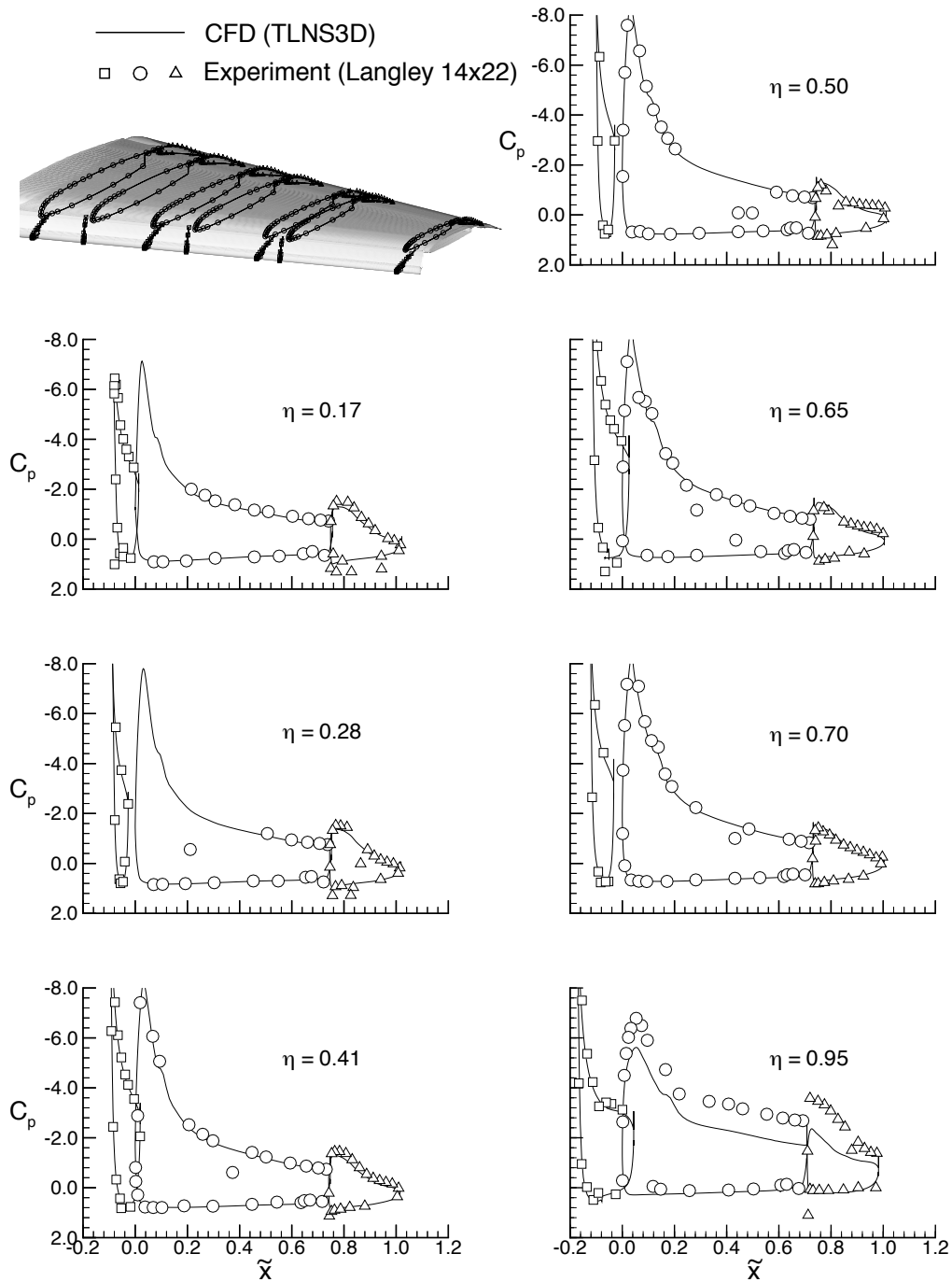
(d)  $\alpha = 28.120^\circ$

Figure 10. Continued.



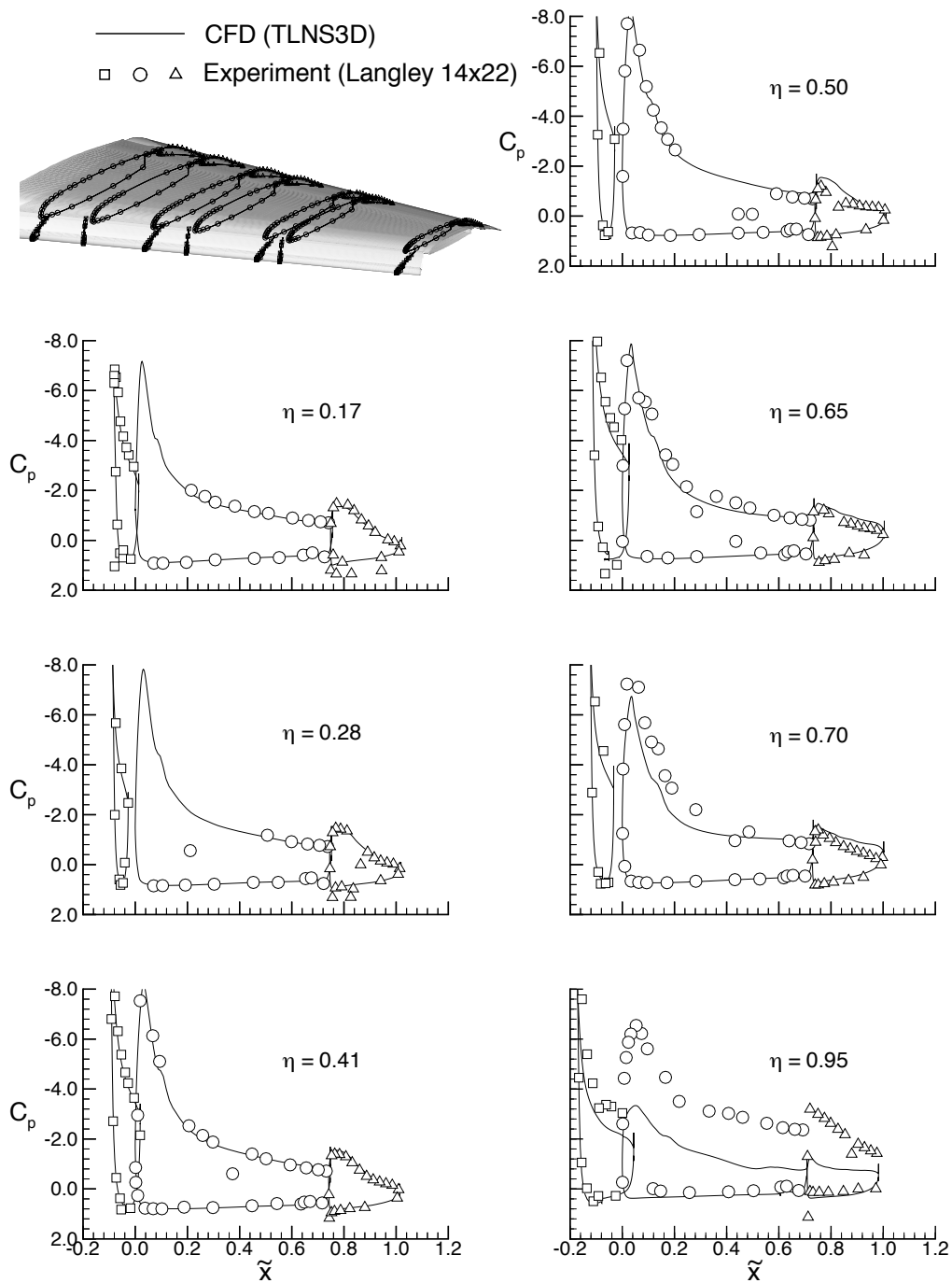
(e)  $\alpha = 29.877^\circ$

Figure 10. Continued.



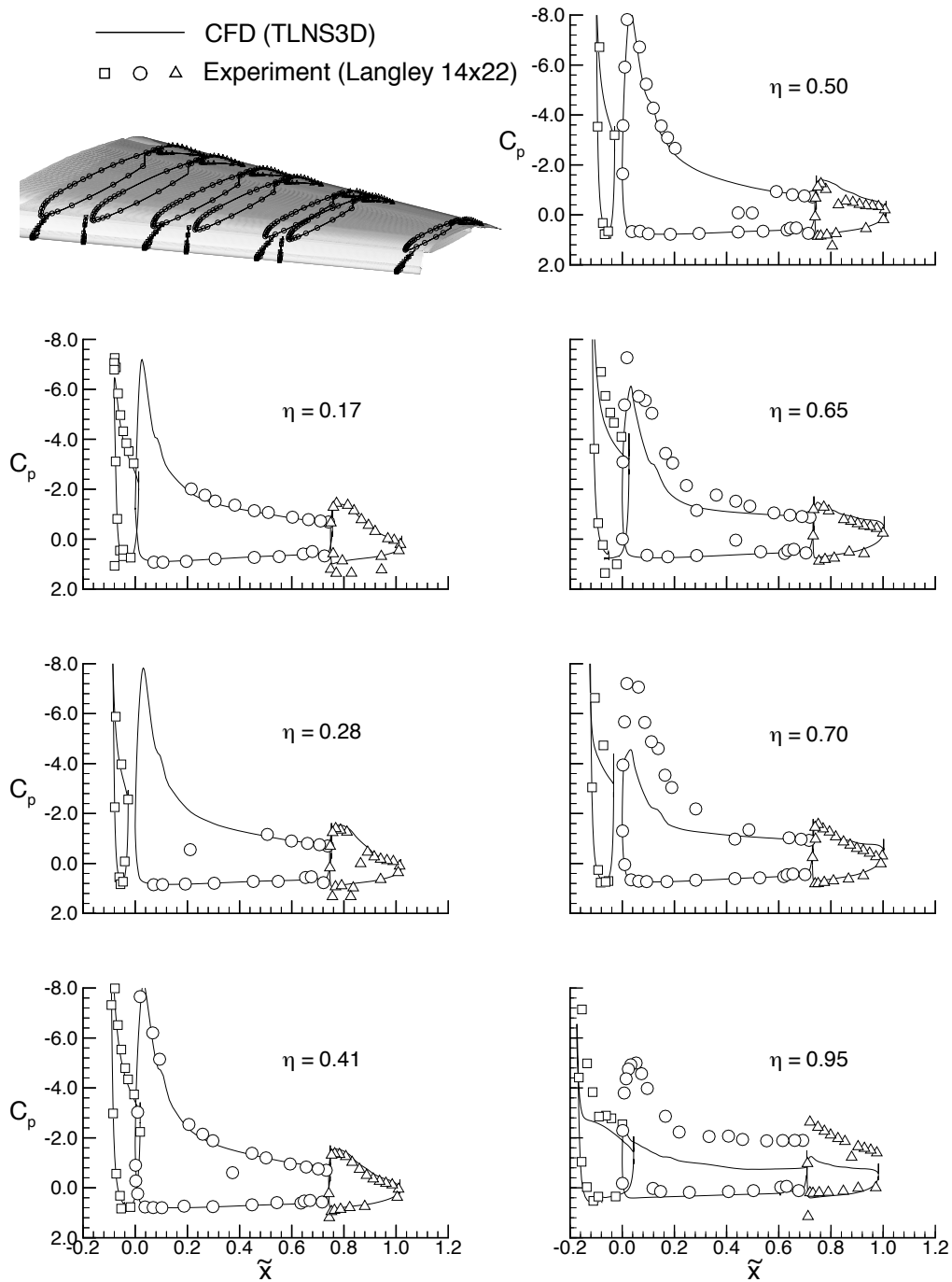
(f)  $\alpha = 32.993^\circ$

Figure 10. Continued.



(g)  $\alpha = 33.980^\circ$

Figure 10. Continued.



(h)  $\alpha = 34.858^\circ$

Figure 10. Concluded.

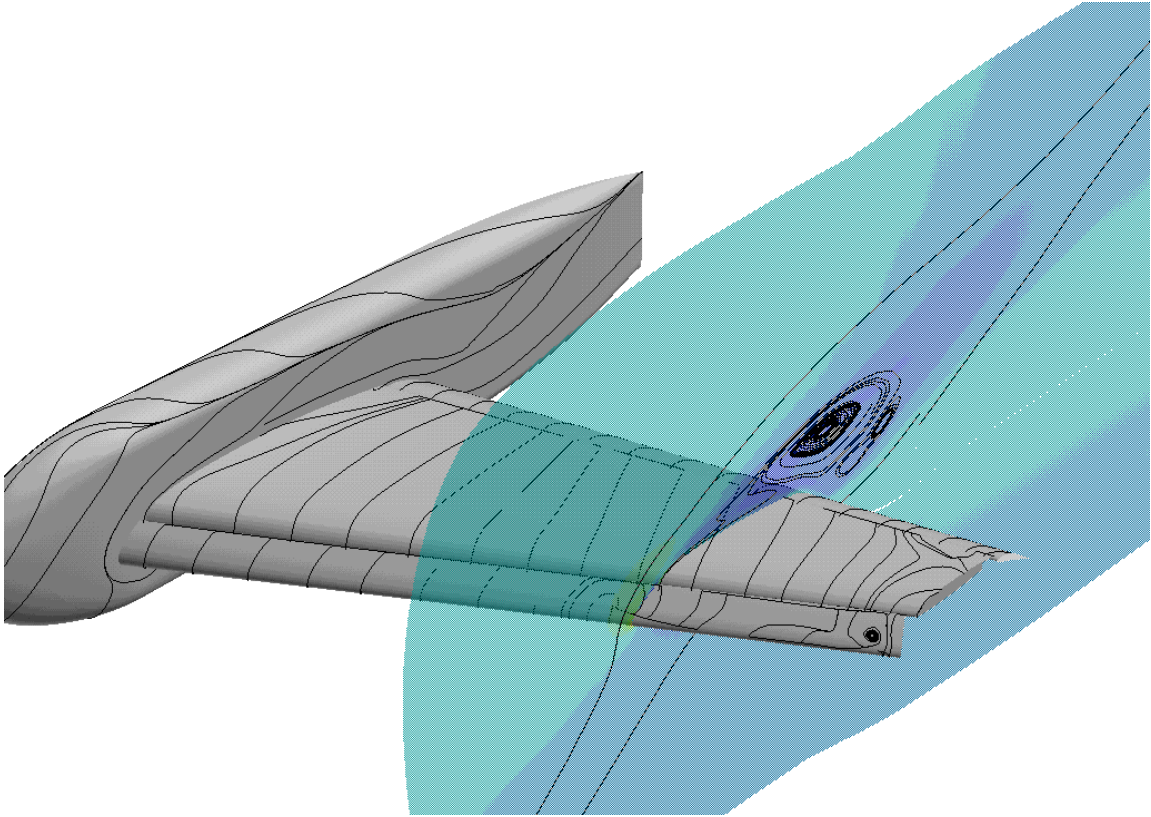
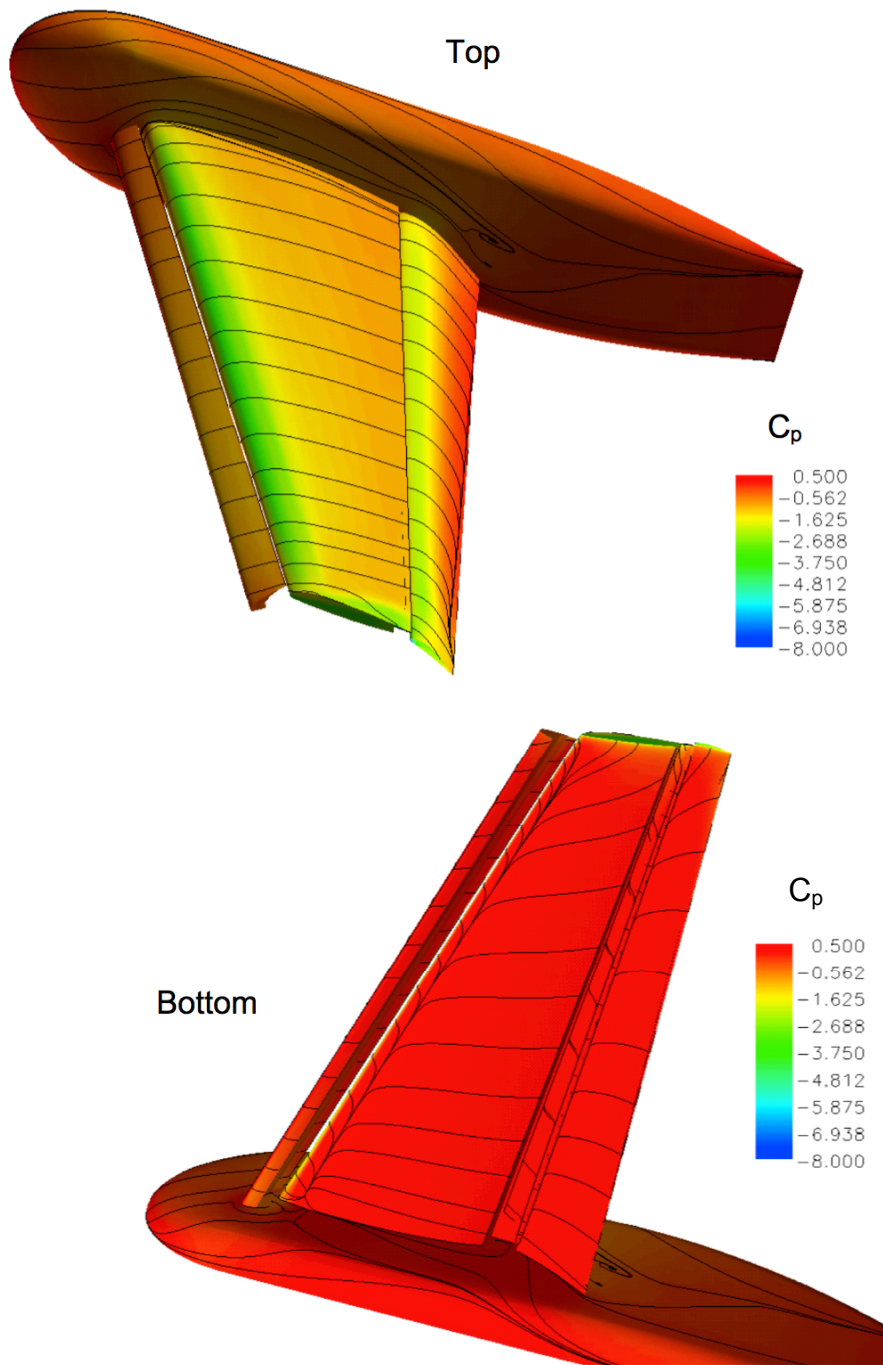
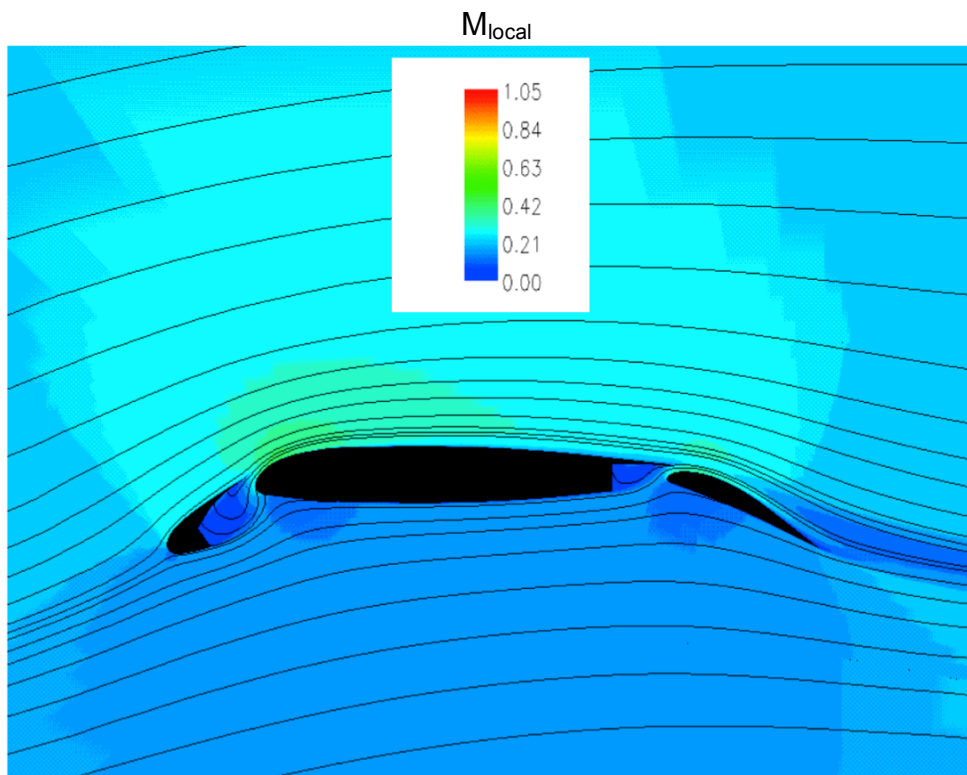


Figure 11. Sketch depicting simulated oil flows and streamlines constrained to a vertical plane with the model at a very high angle of attack. ( $M_\infty = 0.2$ ,  $\alpha \approx 35^\circ$ )

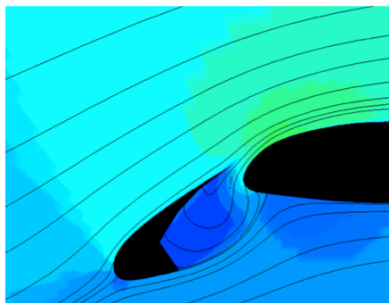


(a) Surface pressure-coefficient contours and constrained streamlines immediately above the surface.

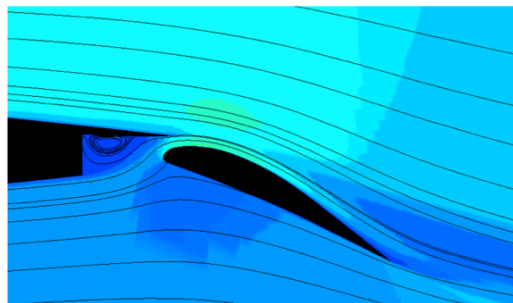
Figure 12. Model surface and flow-field parameters at  $\alpha = 10.004^\circ$ .  
(Spalart-Allmaras turbulence model)



Full wing



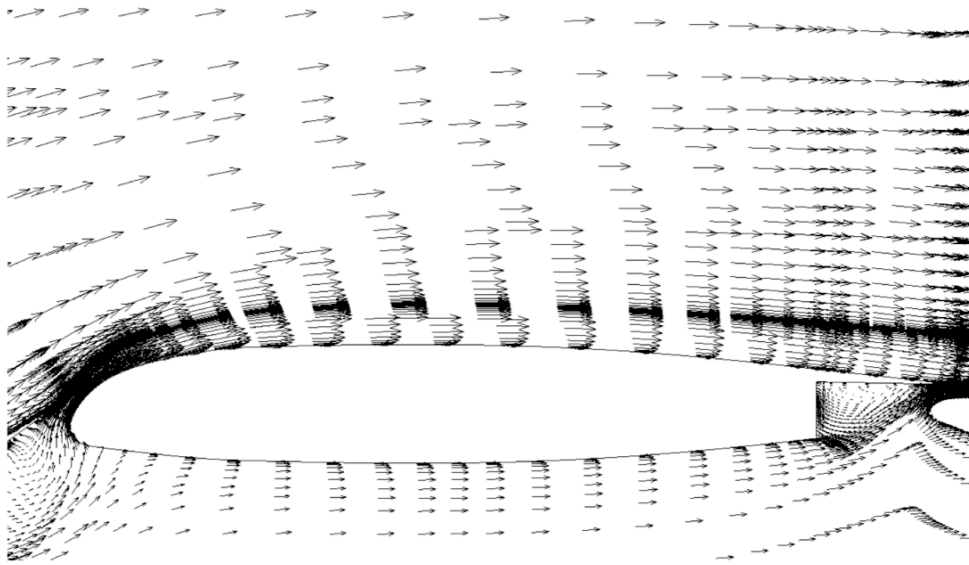
Leading edge region



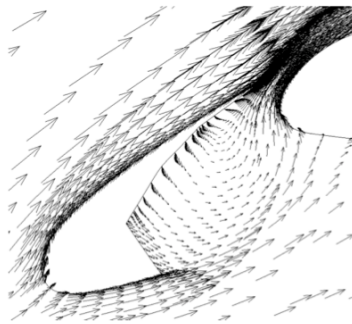
Trailing edge region

(b) Mach number contours and constrained streamline pattern for a stream-wise cut at  $\eta = 0.70$ .

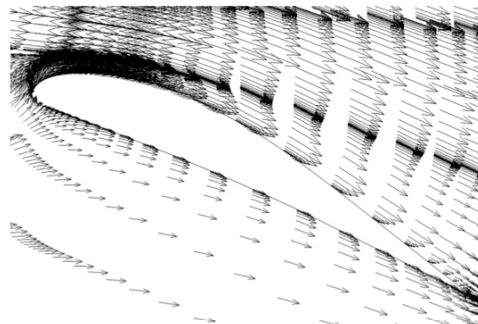
Figure 12. Continued.



Main wing element



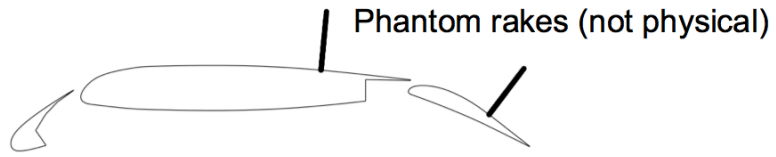
Leading edge region



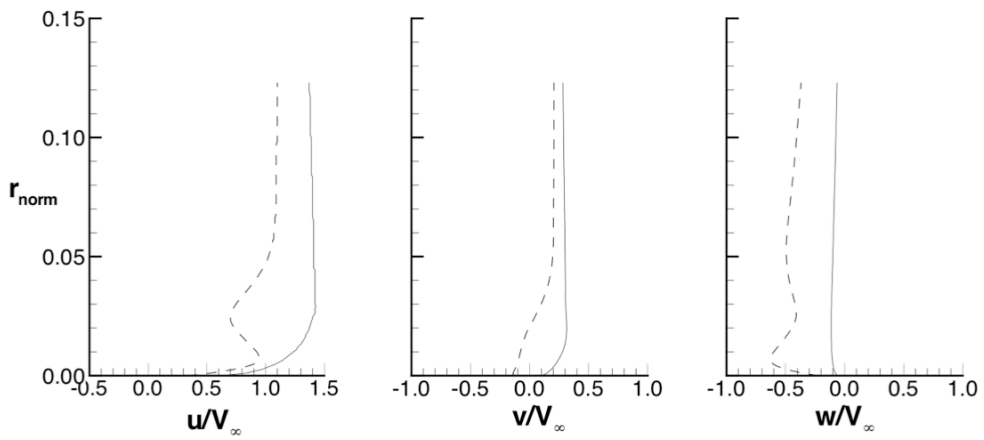
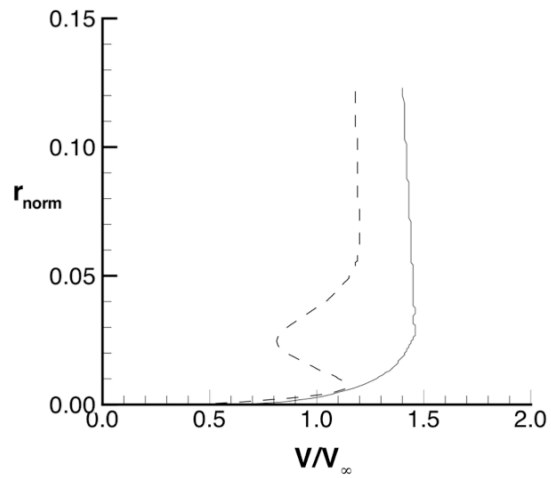
Trailing-edge flap

(c) Velocity vectors for a stream-wise cut at  $\eta = 0.70$ .

Figure 12. Continued.

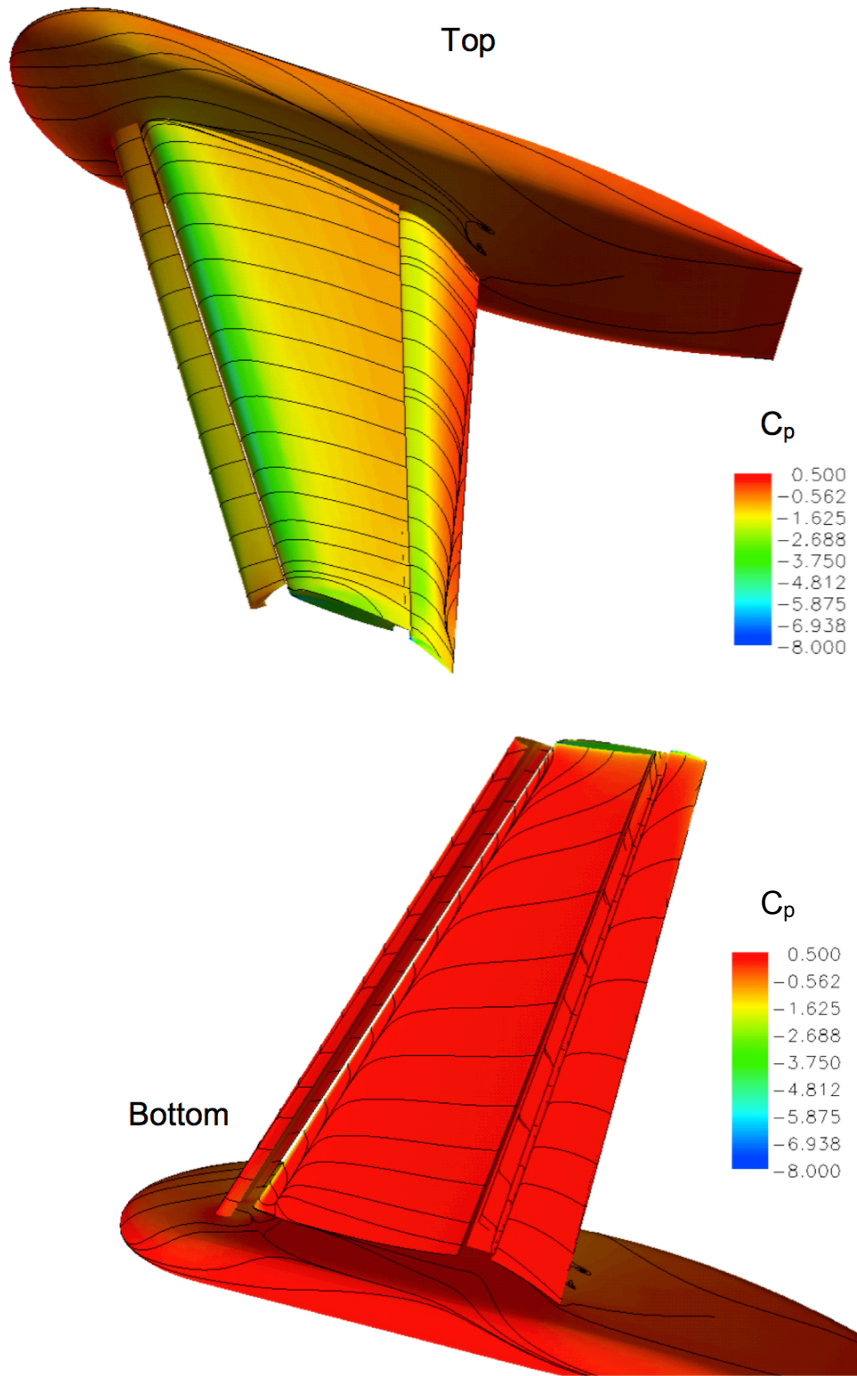


—  $\tilde{x} = 0.50$   
 - - -  $\tilde{x} = 0.85$



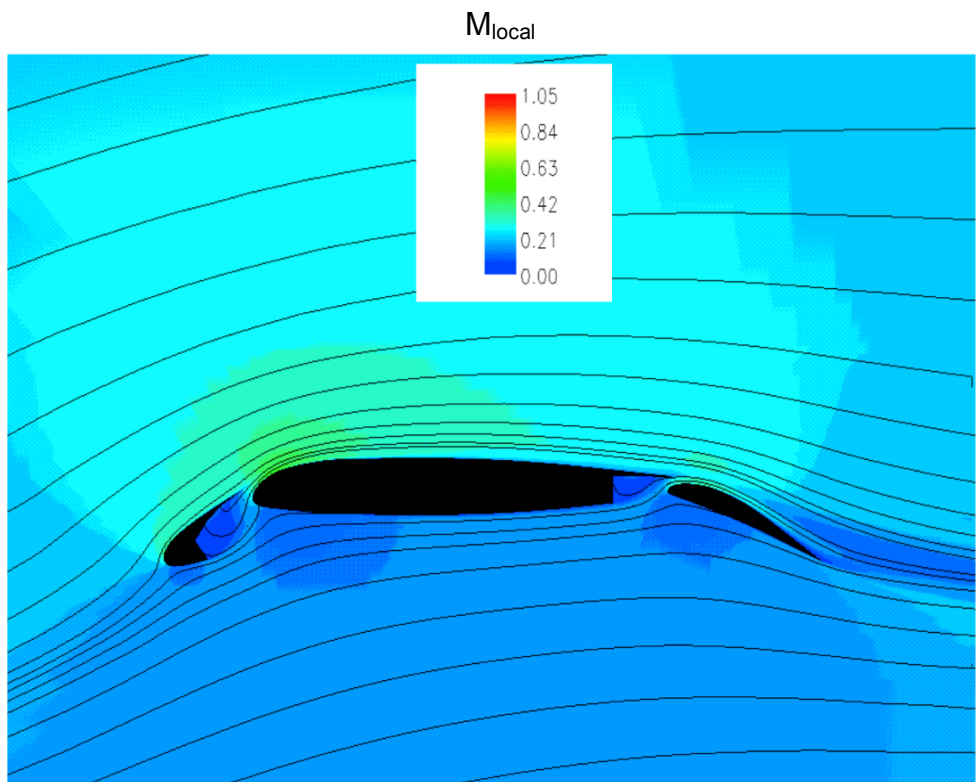
(d) Computed velocity profiles near the model surface at  $\eta = 0.70$ .

Figure 12. Concluded.

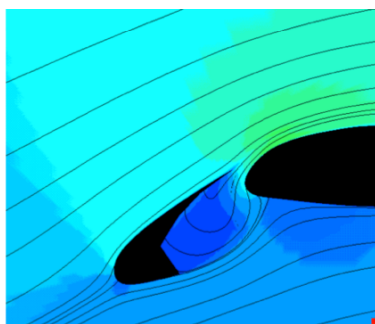


(a) Surface pressure-coefficient contours and constrained streamlines immediately above the surface.

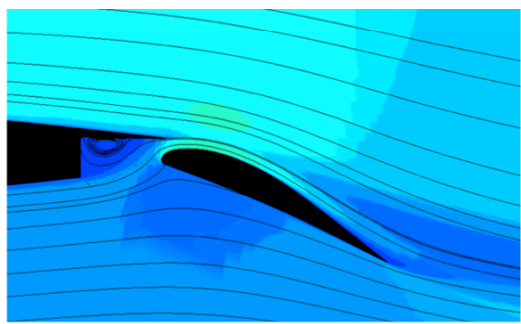
Figure 13. Model surface and flow-field parameters at  $\alpha = 14.000^\circ$ .  
(Spalart-Allmaras turbulence model)



Full wing



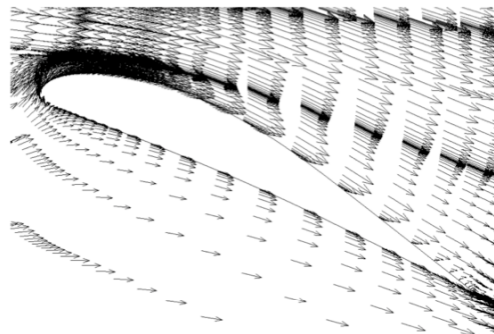
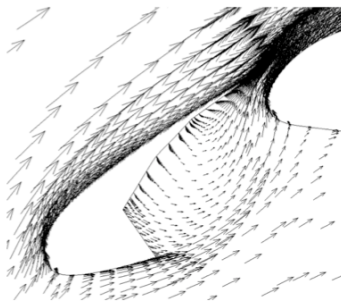
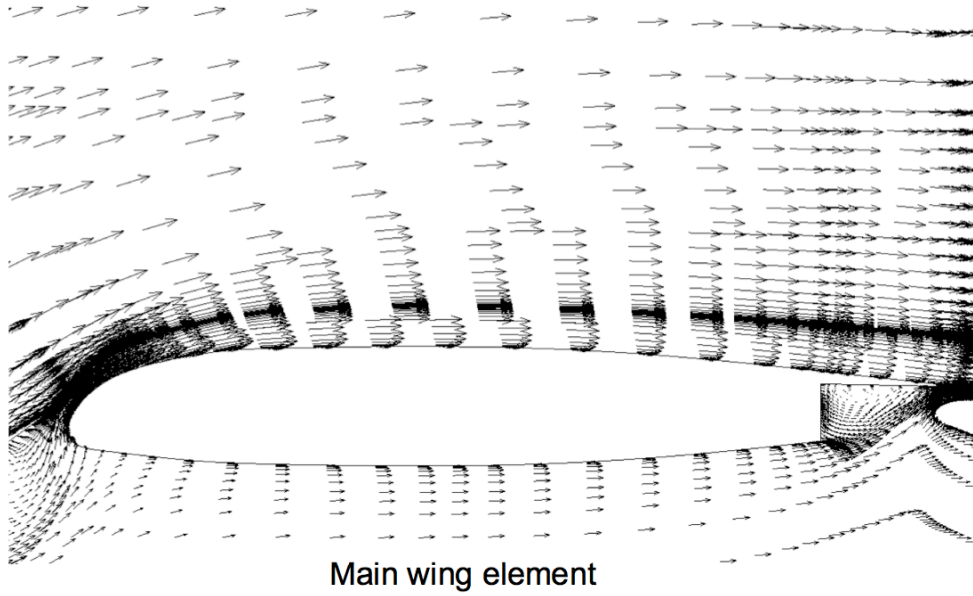
Leading edge region



Trailing edge region

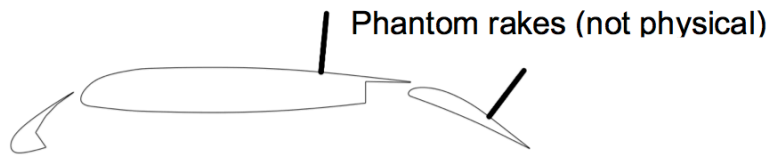
(b) Mach number contours and constrained streamline pattern for a stream-wise cut at  $\eta = 0.70$ .

Figure 13. Continued.

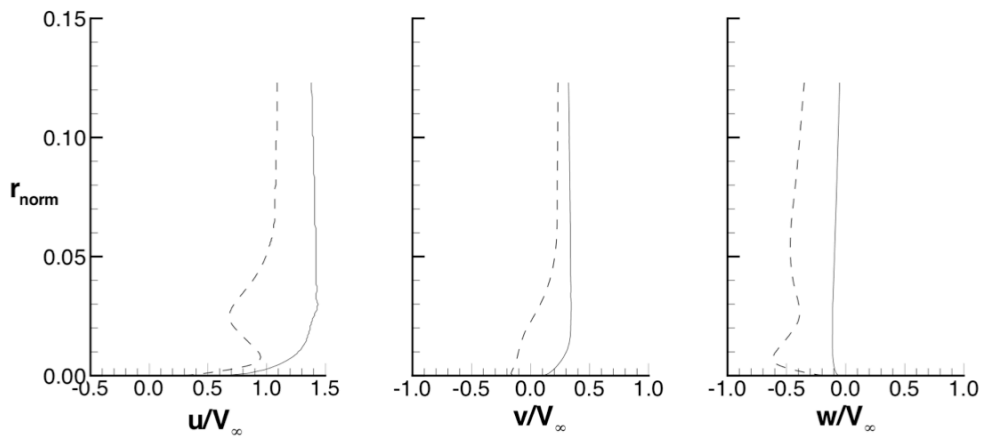
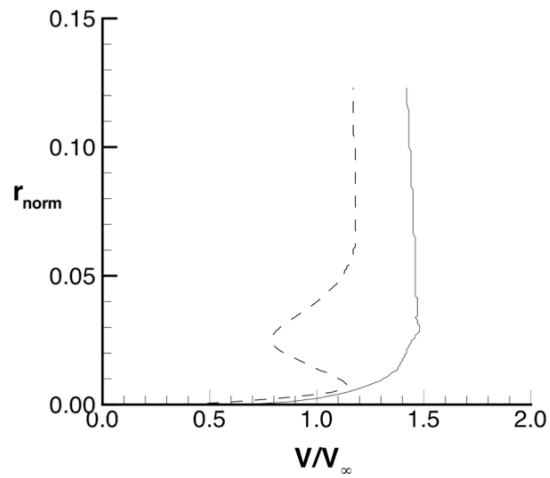


(c) Velocity vectors for a stream-wise cut at  $\eta = 0.70$ .

Figure 13. Continued.

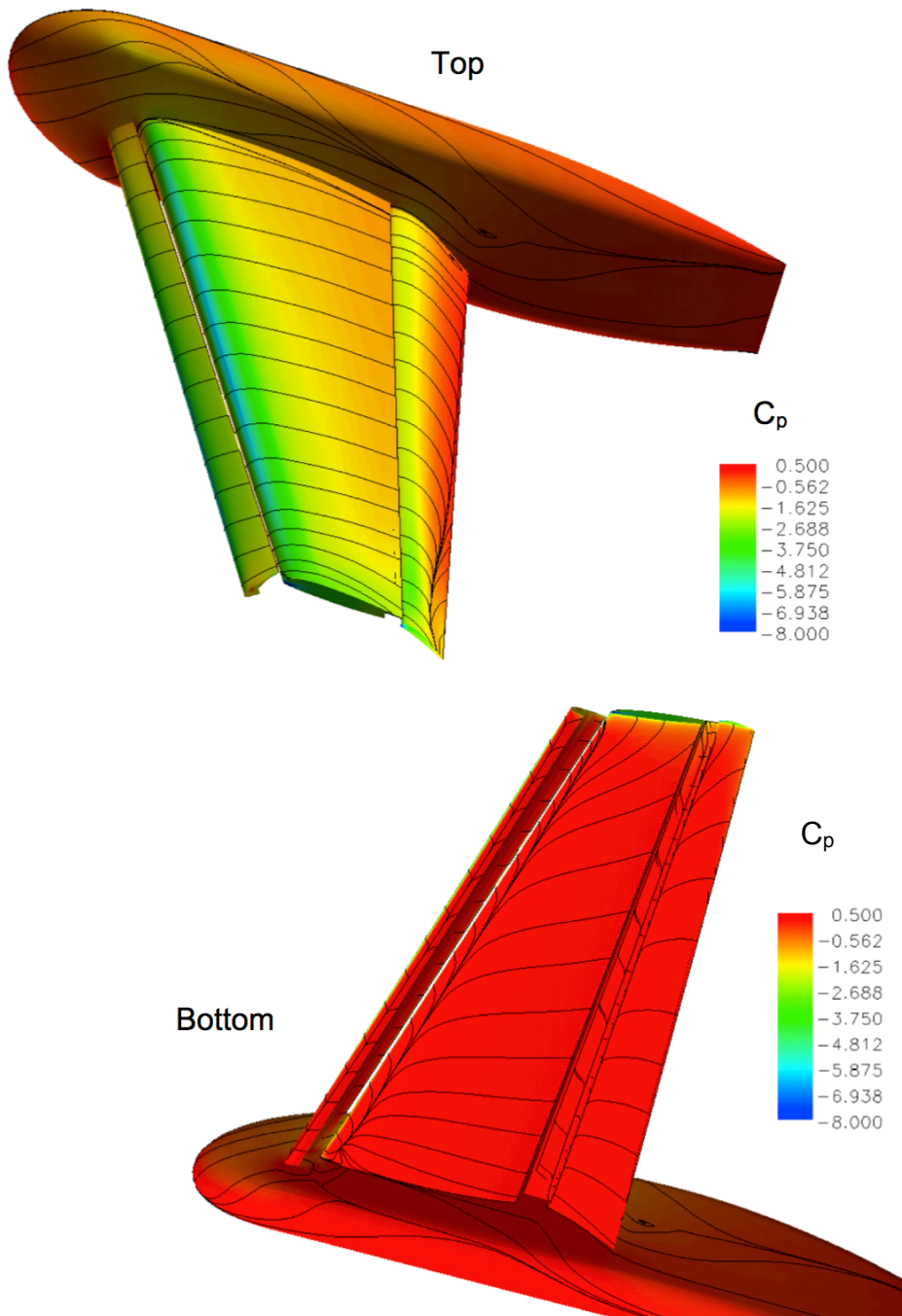


—  $\tilde{x} = 0.50$   
 - - -  $\tilde{x} = 0.85$



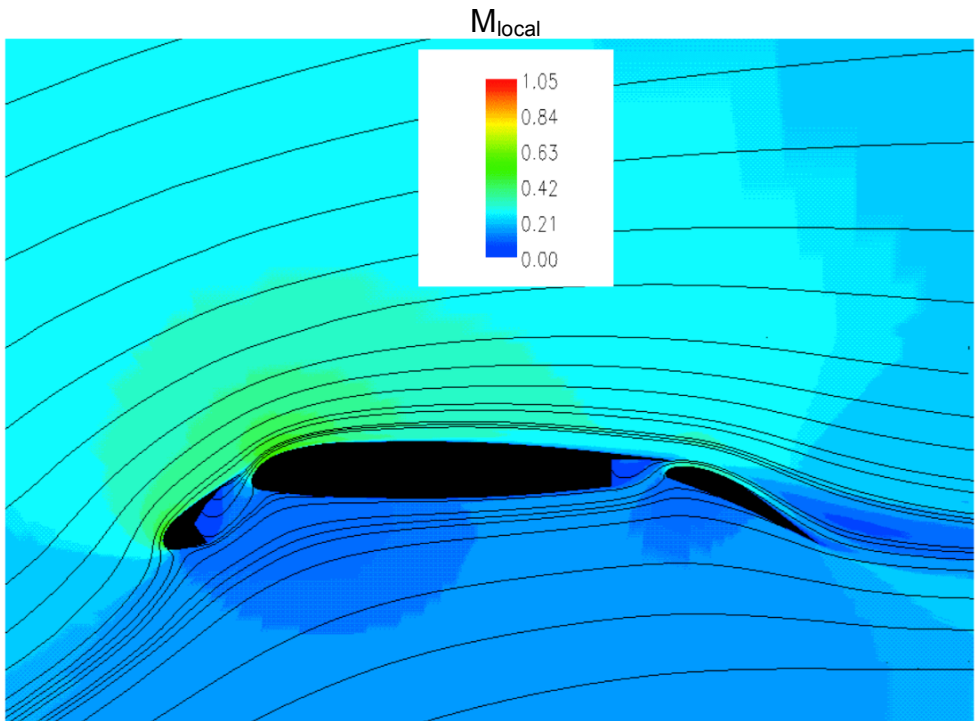
(d) Computed velocity profiles near the model surface at  $\eta = 0.70$ .

Figure 13. Concluded.

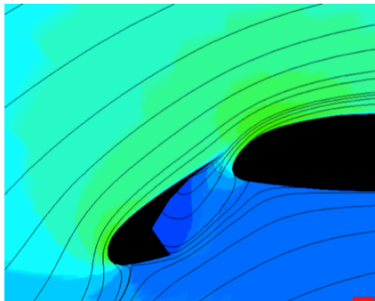


(a) Surface pressure-coefficient contours and constrained streamlines immediately above the surface.

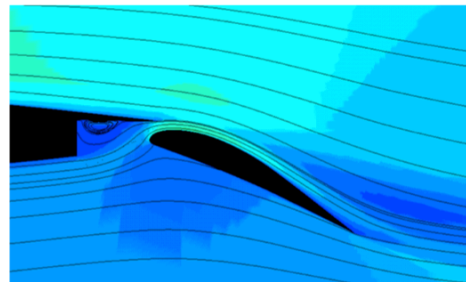
Figure 14. Model surface and flow-field parameters at  $\alpha = 19.937^\circ$ .  
(Spalart-Allmaras turbulence model)



Full wing



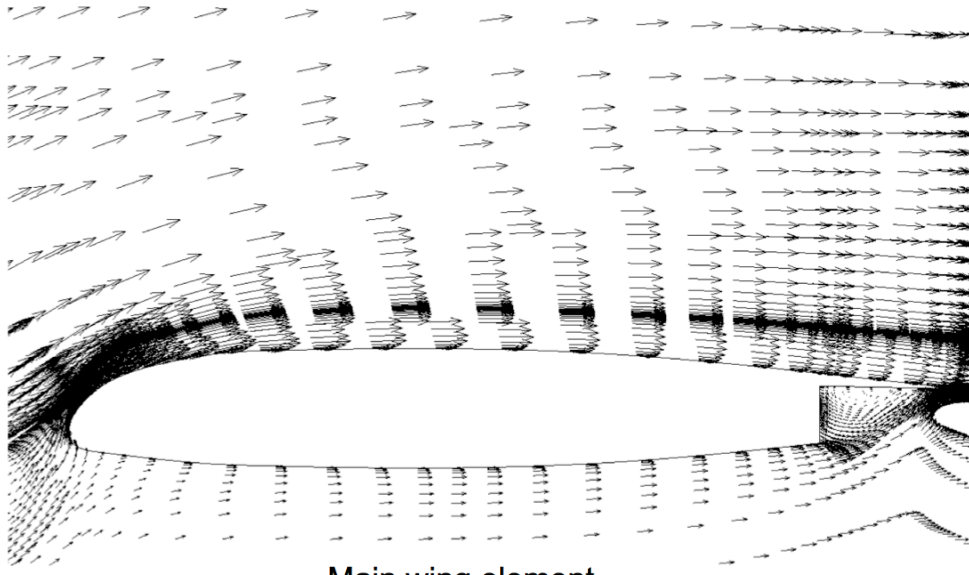
Leading edge region



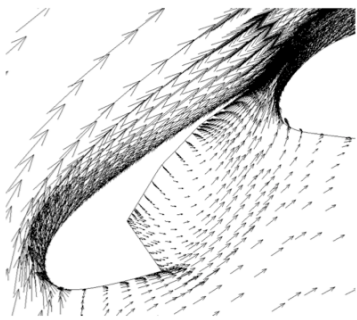
Trailing edge region

(b) Mach number contours and constrained streamline pattern for a stream-wise cut at  $\eta = 0.70$ .

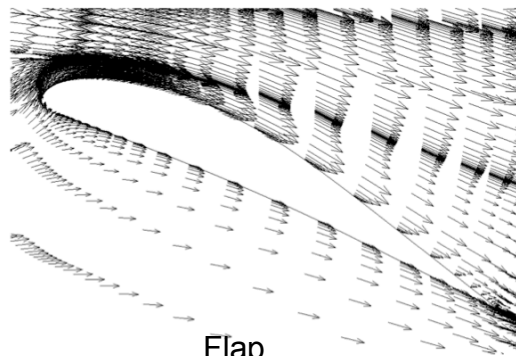
Figure 14. Continued.



Main wing element



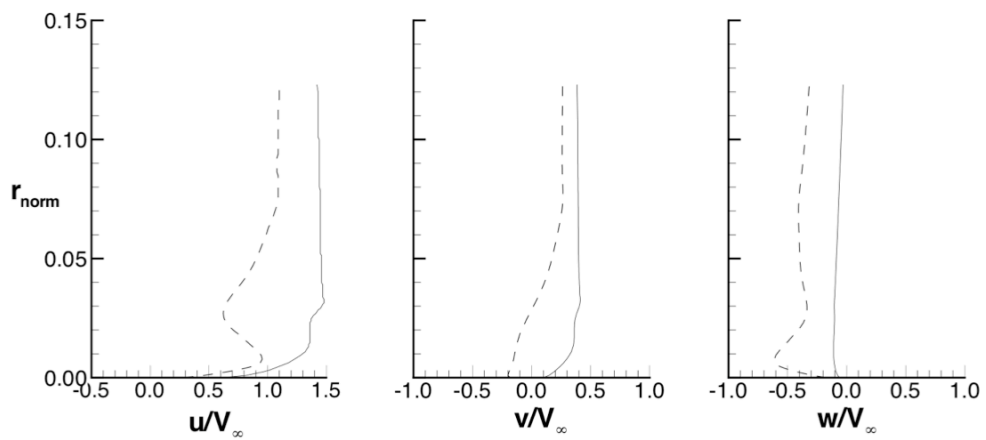
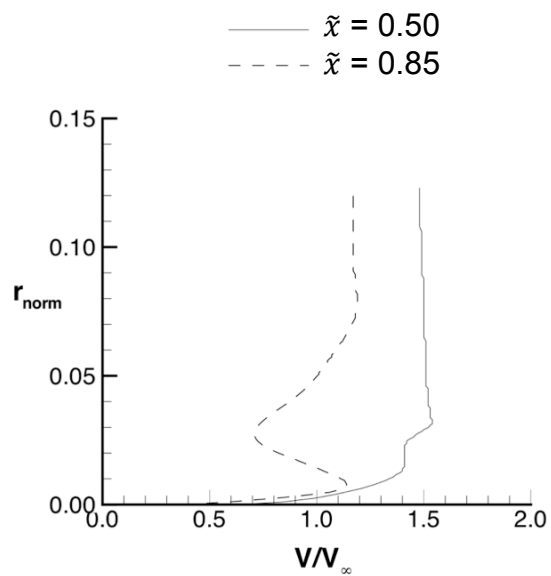
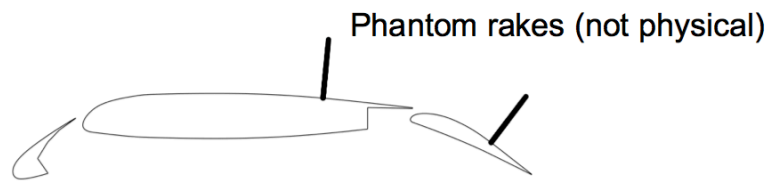
Leading edge region



Flap

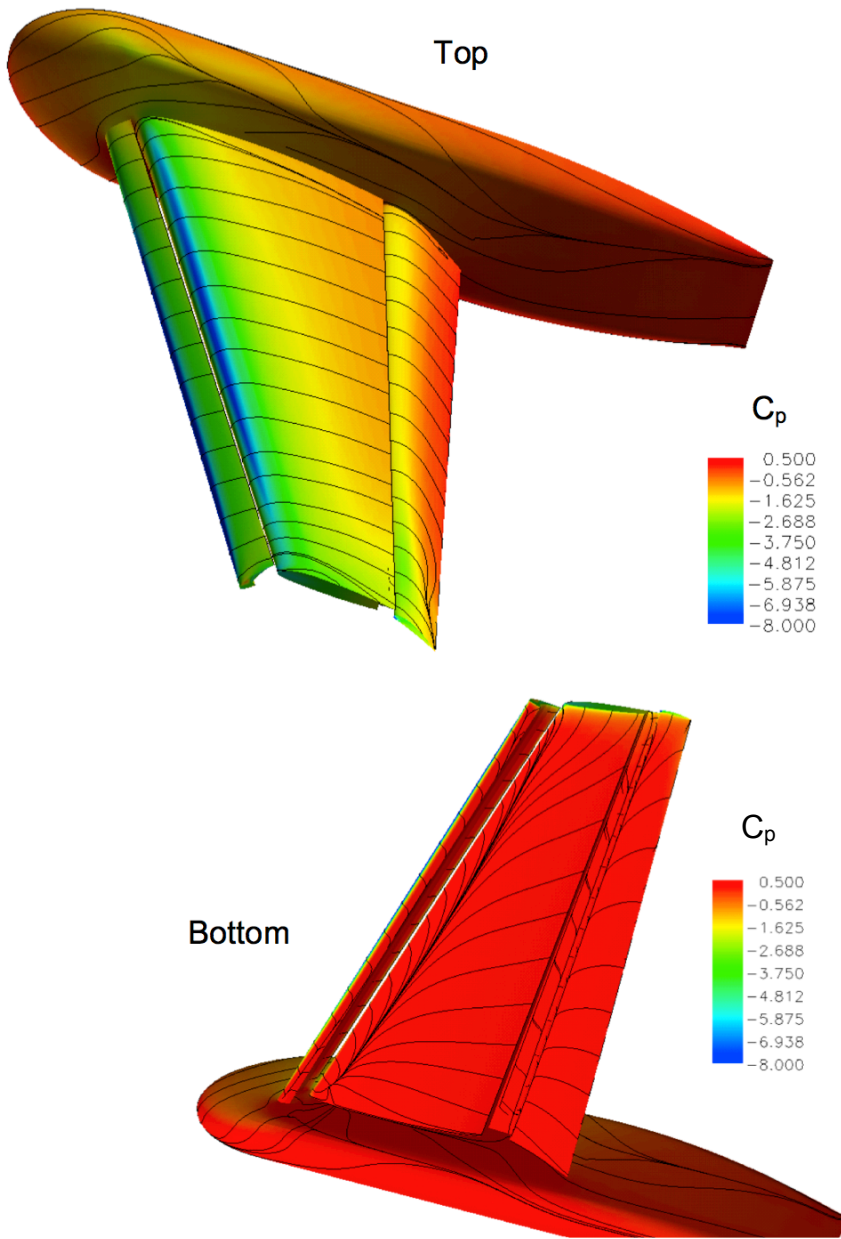
(c) Velocity vectors for a stream-wise cut at  $\eta = 0.70$ .

Figure 14. Continued.



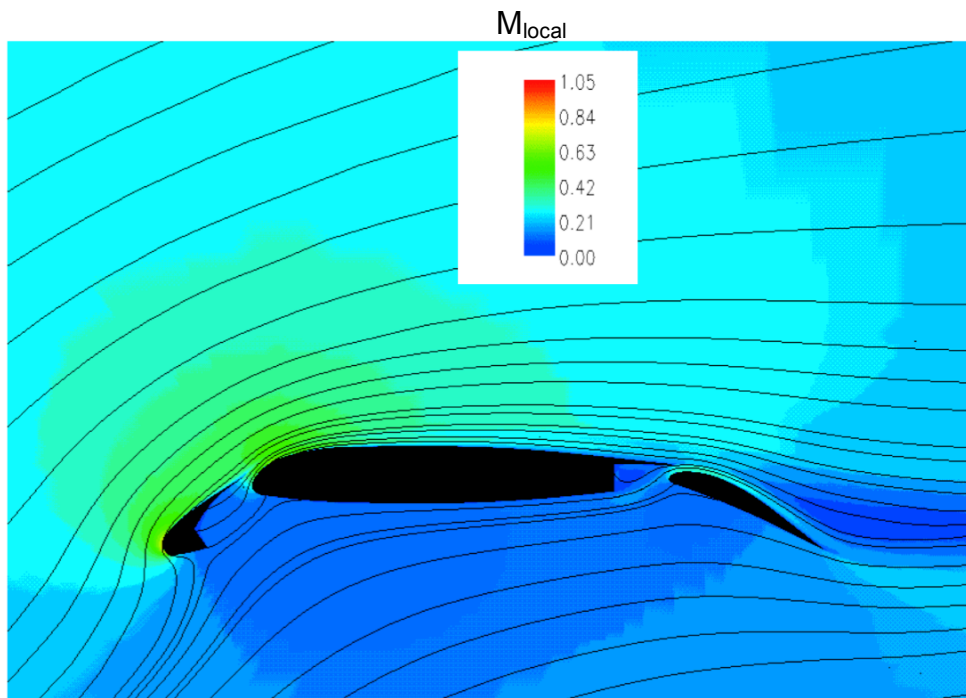
(d) Computed velocity profiles near the model surface at  $\eta = 0.70$ .

Figure 14. Concluded.

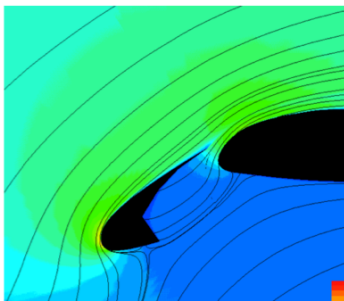


(a) Surface pressure-coefficient contours and constrained streamlines immediately above the surface.

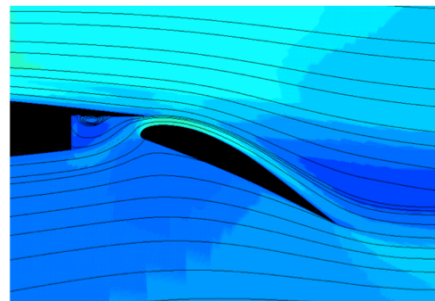
Figure 15. Model surface and flow-field parameters at  $\alpha = 28.120^\circ$ .  
(Spalart-Allmaras turbulence model)



Full wing



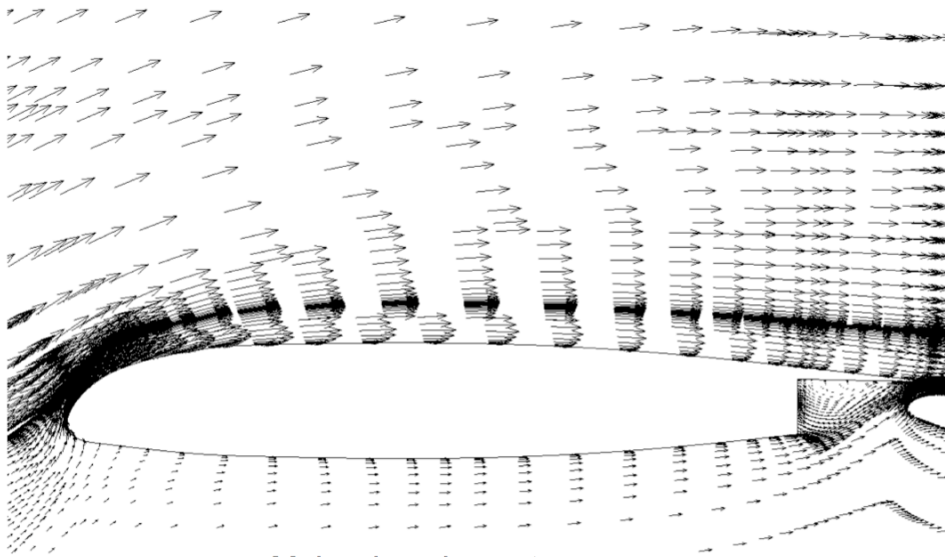
Leading edge region



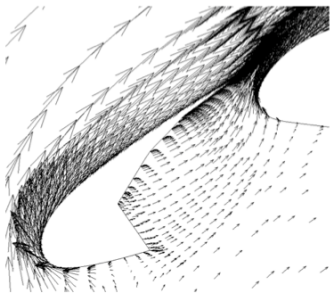
Trailing edge region

(b) Mach number contours and constrained streamline pattern for a stream-wise cut at  $\eta = 0.70$ .

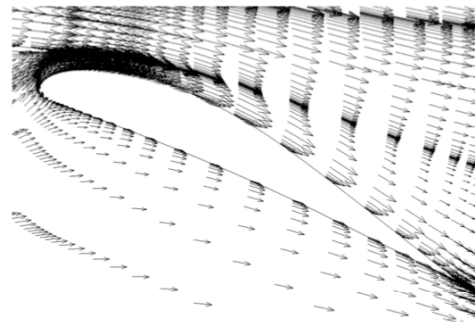
Figure 15. Continued.



Main wing element



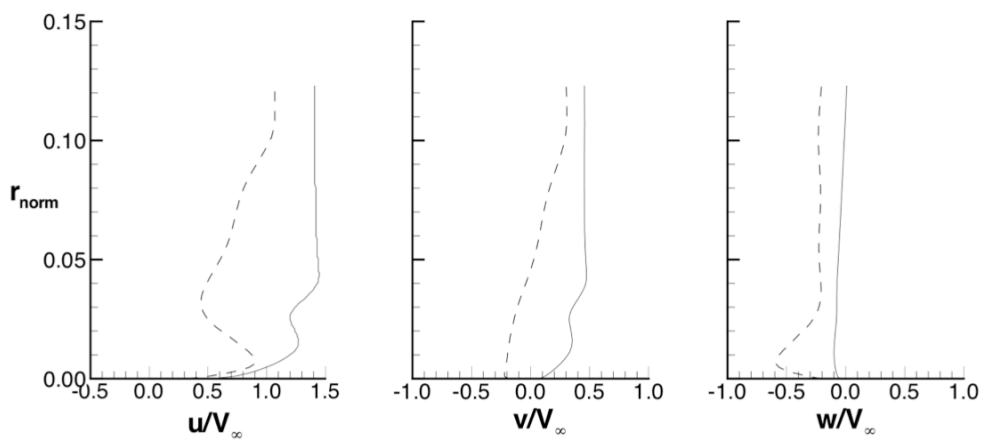
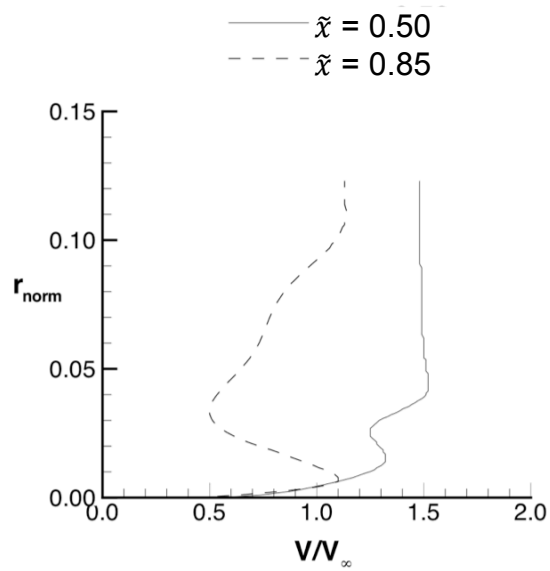
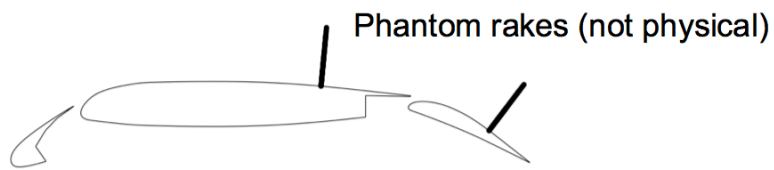
Leading edge region



Flap

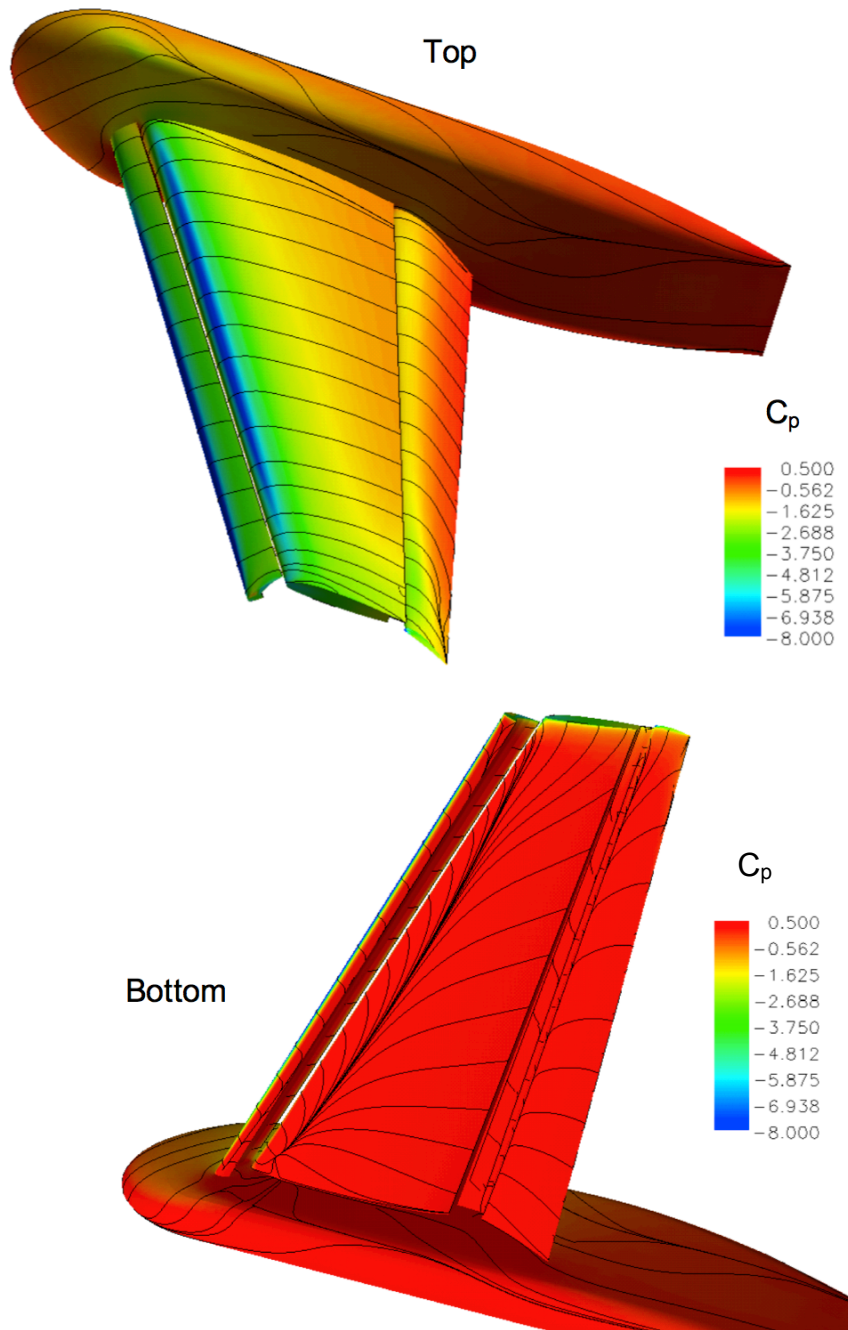
(c) Velocity vectors for a stream-wise cut at  $\eta = 0.70$ .

Figure 15. Continued.



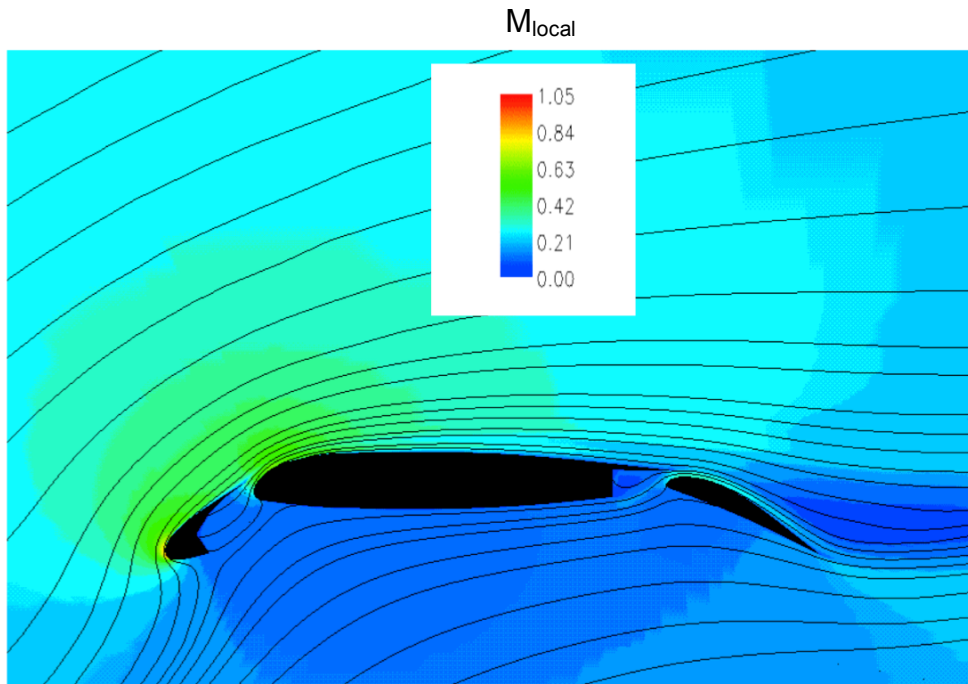
(d) Computed velocity profiles near the model surface at  $\eta = 0.70$ .

Figure 15. Concluded.

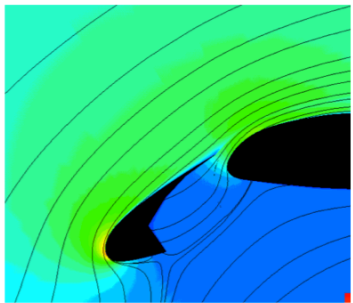


(a) Surface pressure-coefficient contours and constrained streamlines immediately above the surface.

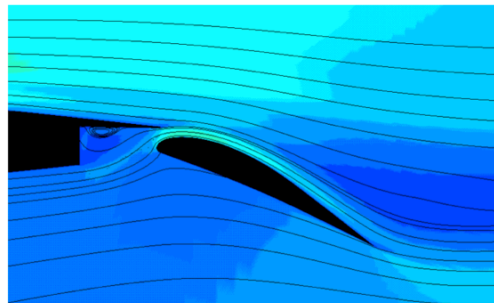
Figure 16. Model surface and flow-field parameters at  $\alpha = 29.877^\circ$ .  
(Spalart-Allmaras turbulence model)



Full wing



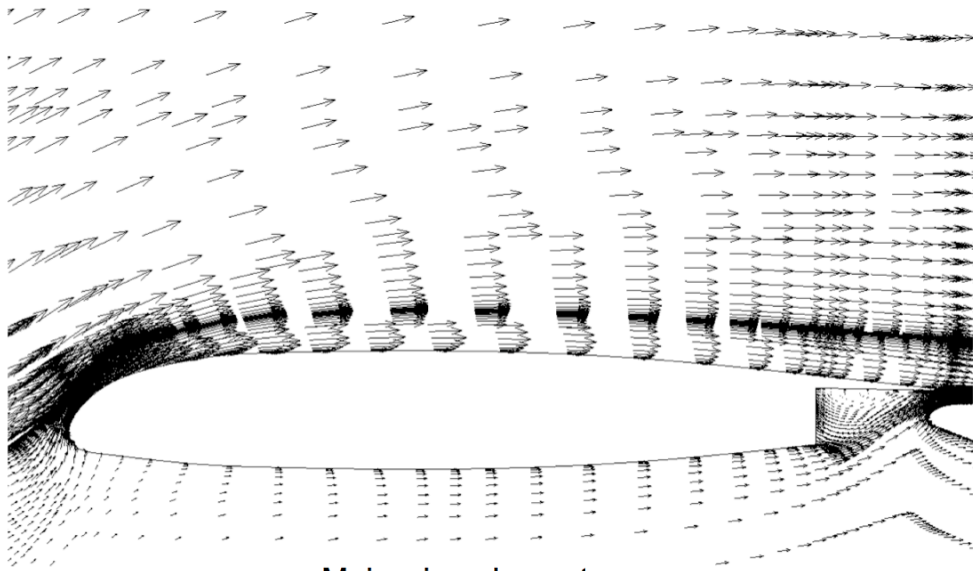
Leading edge region



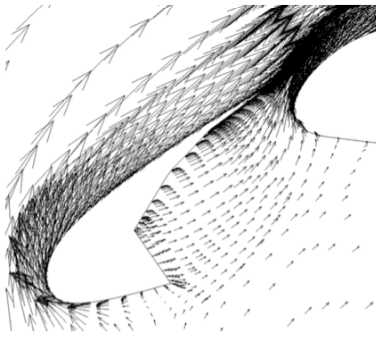
Trailing edge region

(b) Mach number contours and constrained streamline pattern for a stream-wise cut at  $\eta = 0.70$ .

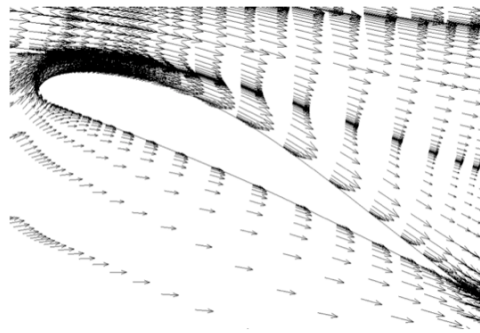
Figure 16. Continued.



Main wing element



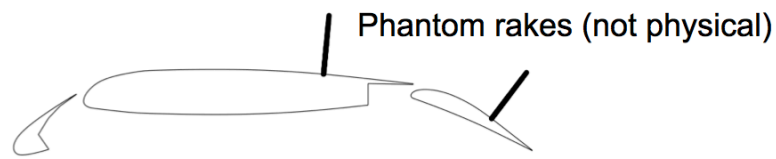
Leading edge region



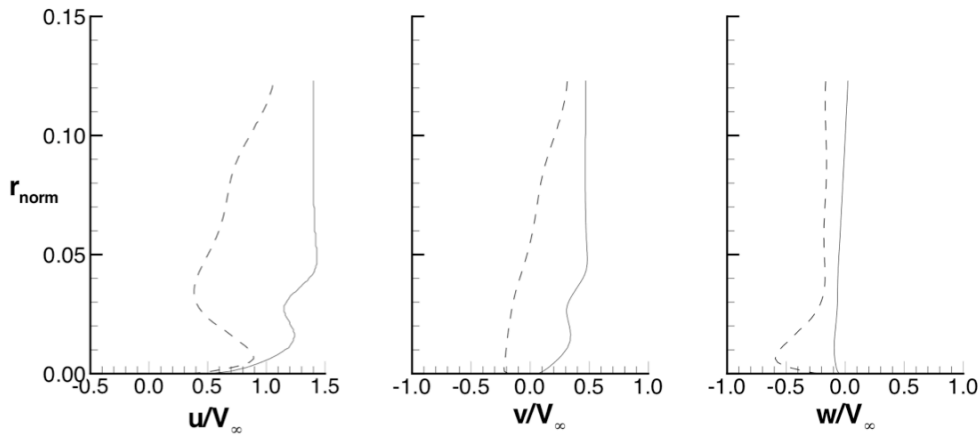
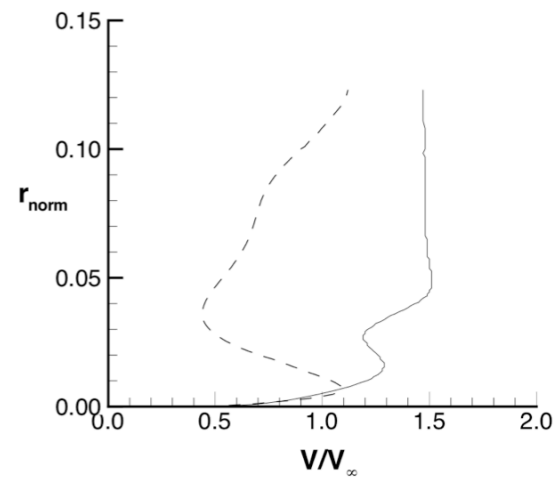
Flap

(c) Velocity vectors for a stream-wise cut at  $\eta = 0.70$ .

Figure 16. Continued.

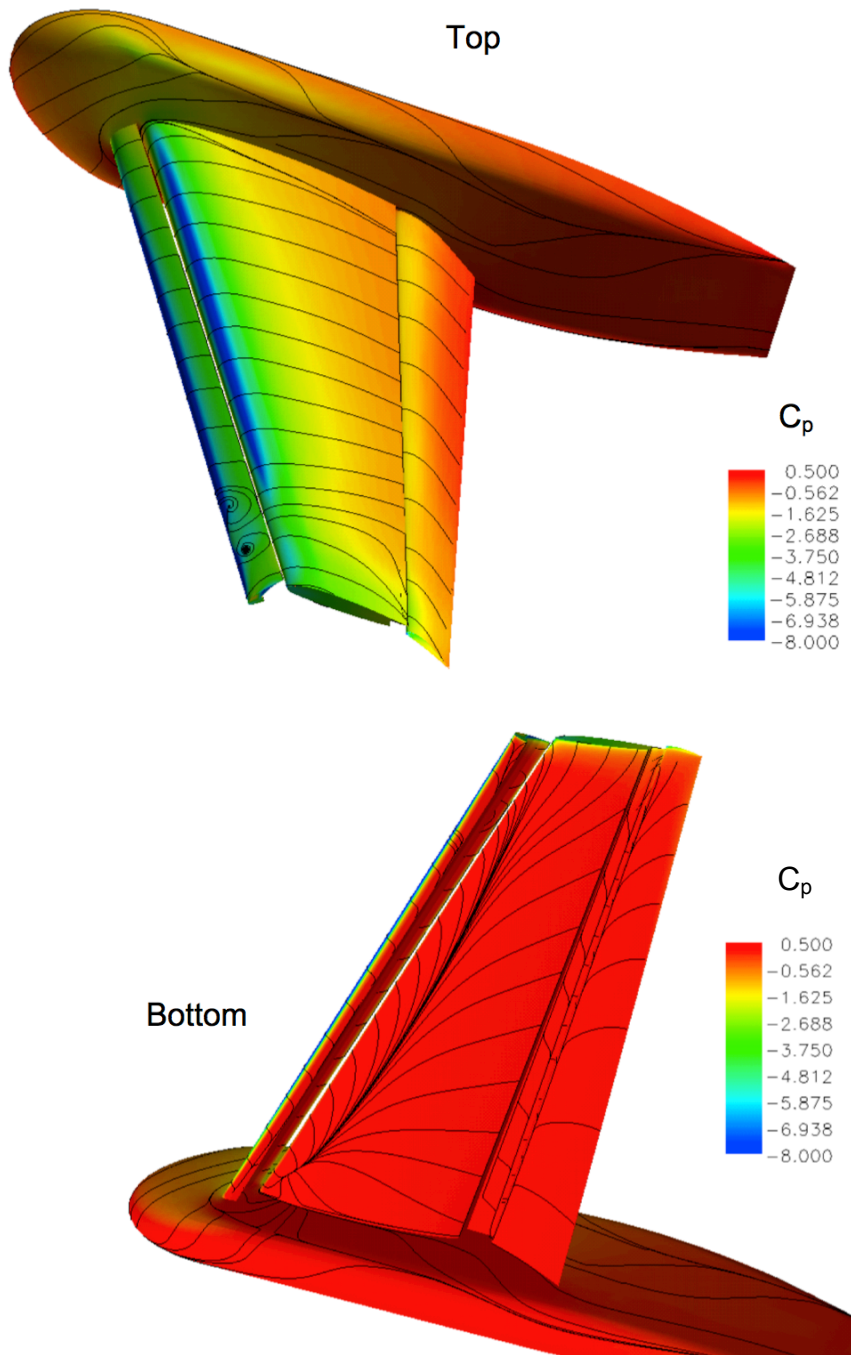


—  $\tilde{x} = 0.50$   
 - - -  $\tilde{x} = 0.85$



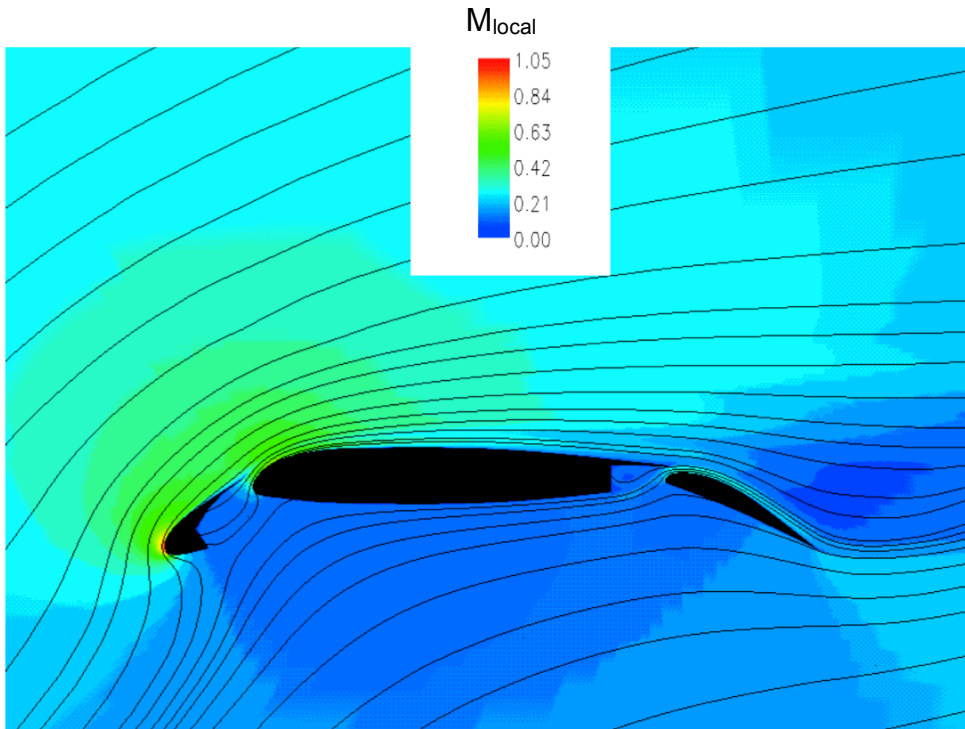
(d) Computed velocity profiles near the model surface at  $\eta = 0.70$ .

Figure 16. Concluded.

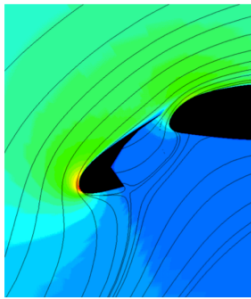


(a) Surface pressure-coefficient contours and constrained streamlines immediately above the surface.

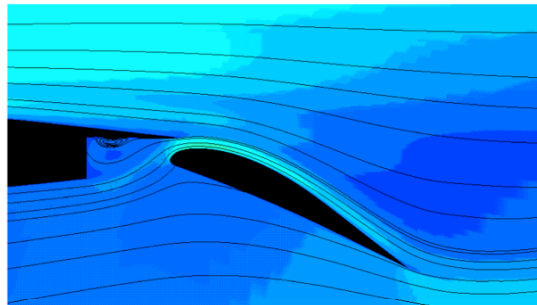
Figure 17. Model surface and flow-field parameters at  $\alpha = 32.993^\circ$ .  
(Spalart-Allmaras turbulence model)



Full wing



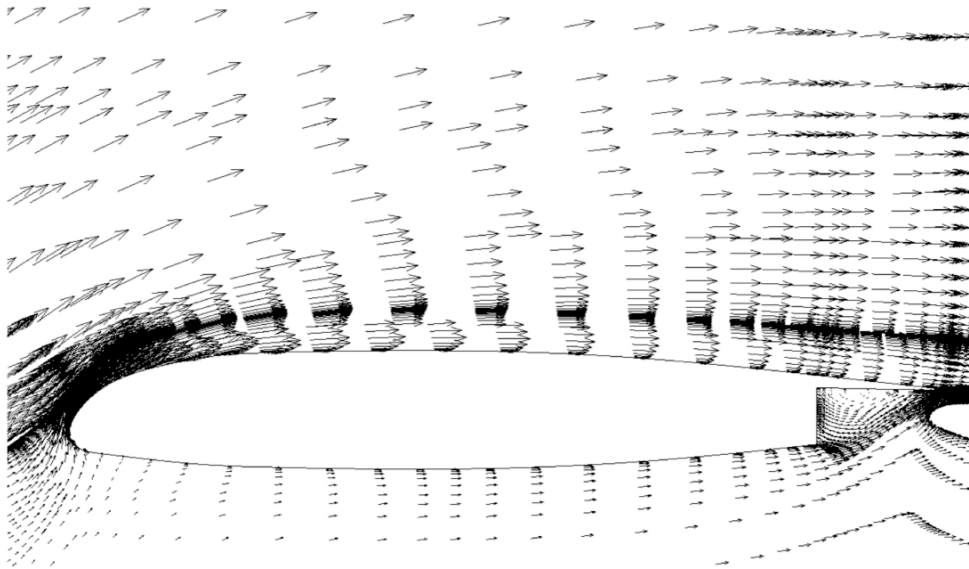
Leading edge region



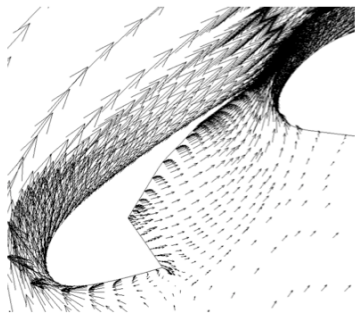
Trailing edge region

(b) Mach number contours and constrained streamline pattern at  $\eta = 0.70$ .

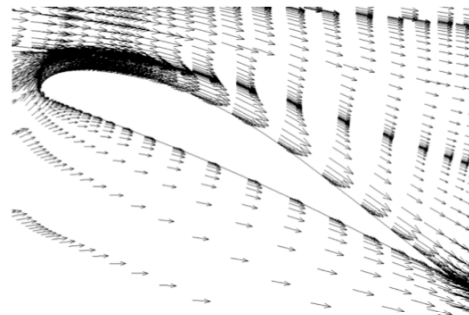
Figure 17. Continued.



Main wing element



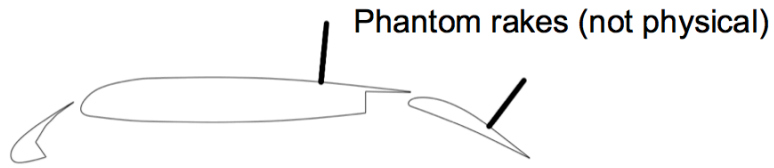
Leading edge region



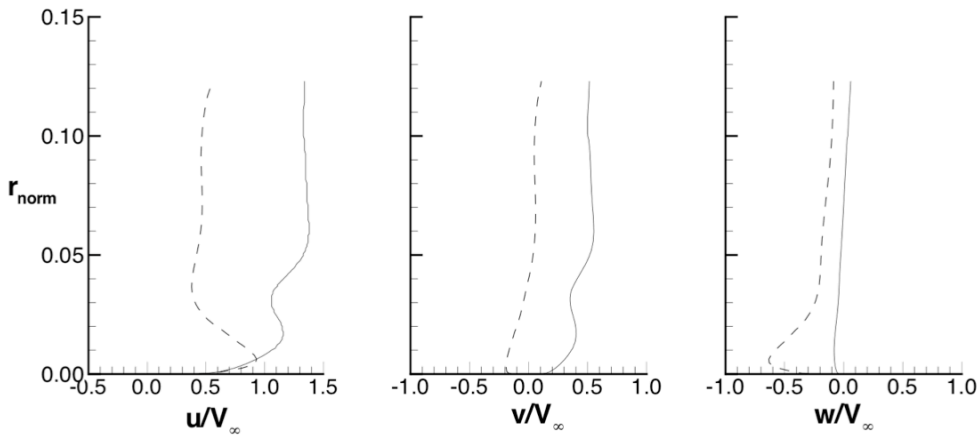
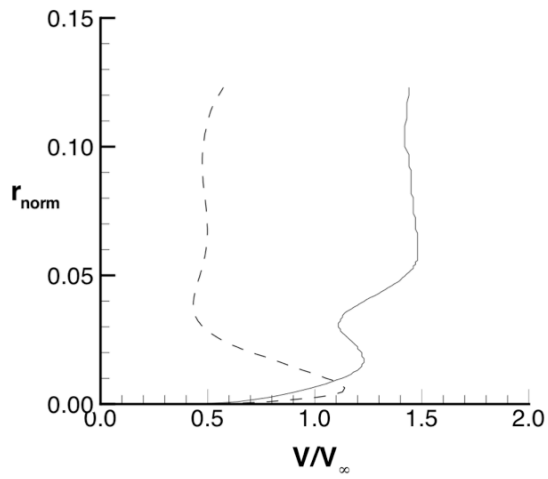
Flap

(c) Velocity vectors for a stream-wise cut at  $\eta = 0.70$ .

Figure 17. Continued.

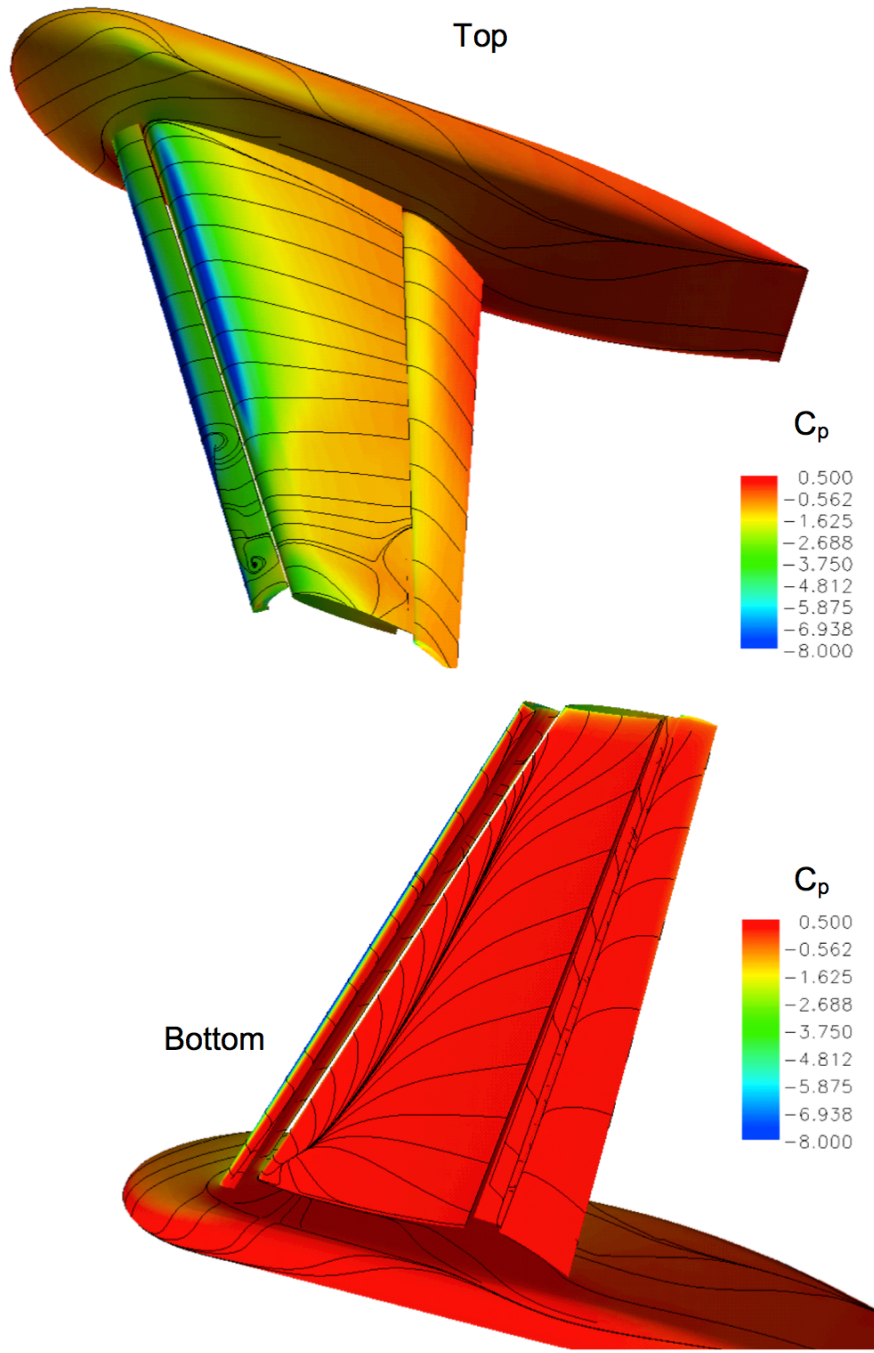


—  $\tilde{x} = 0.50$   
 - - -  $\tilde{x} = 0.85$



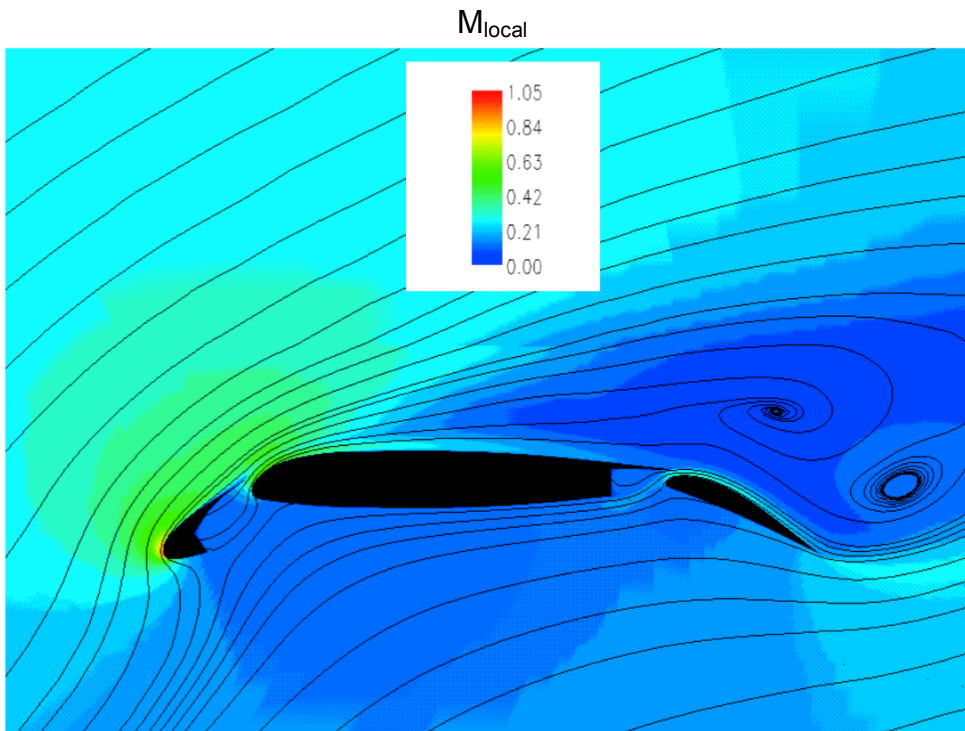
(d) Computed velocity profiles near the model surface at  $\eta = 0.70$ .

Figure 17. Concluded.

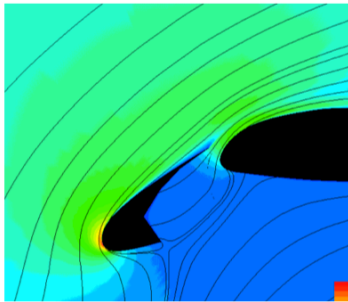


(a) Surface pressure-coefficient contours and constrained streamlines immediately above the surface.

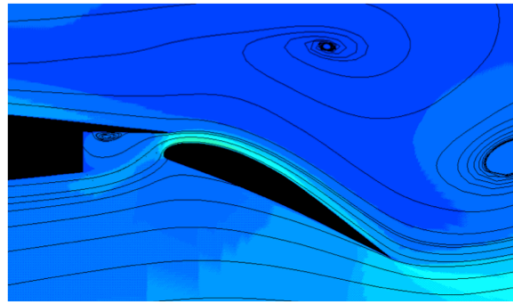
Figure 18. Model surface and flow-field parameters at  $\alpha = 33.980^\circ$ .  
(Spalart-Allmaras turbulence model)



Full wing



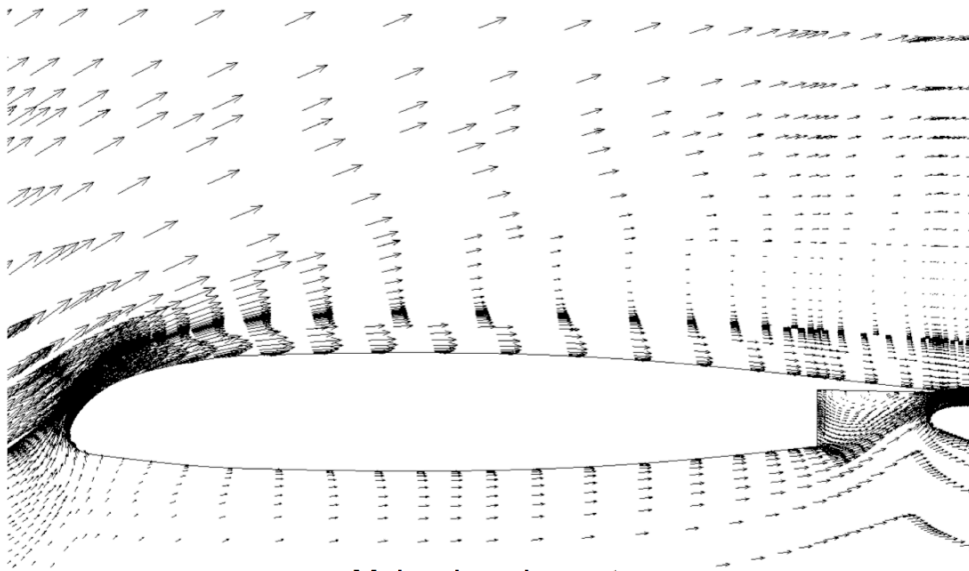
Leading edge region



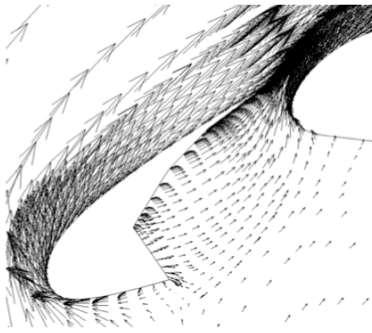
Trailing edge region

(b) Mach number contours and constrained streamline pattern for a stream-wise cut at  $\eta = 0.70$ .

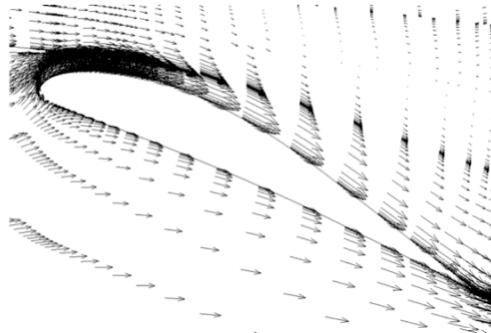
Figure 18. Continued.



Main wing element



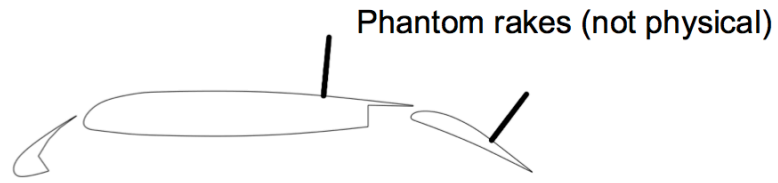
Leading edge region



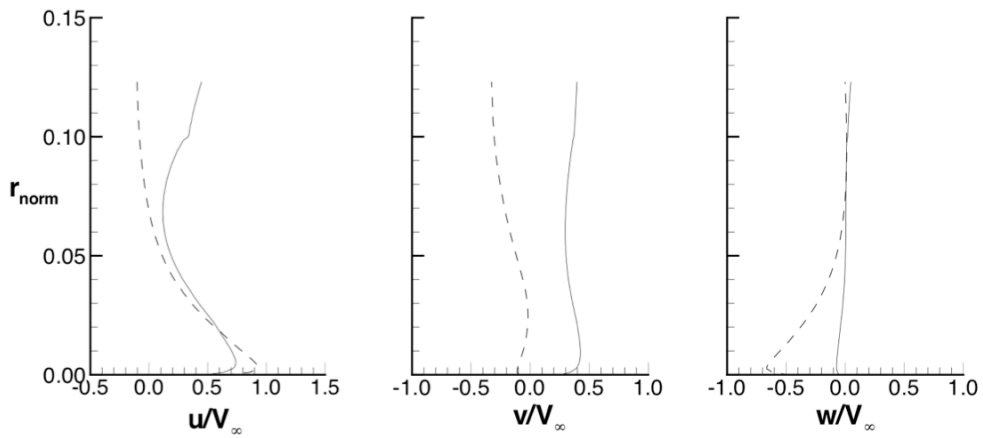
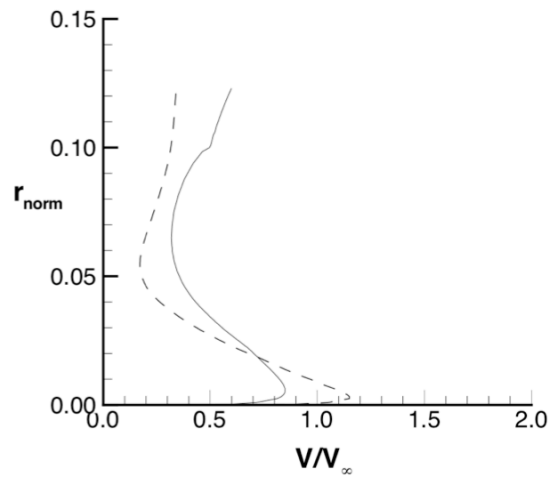
Flap

(c) Velocity vectors for a stream-wise cut at  $\eta = 0.70$ .

Figure 18. Continued

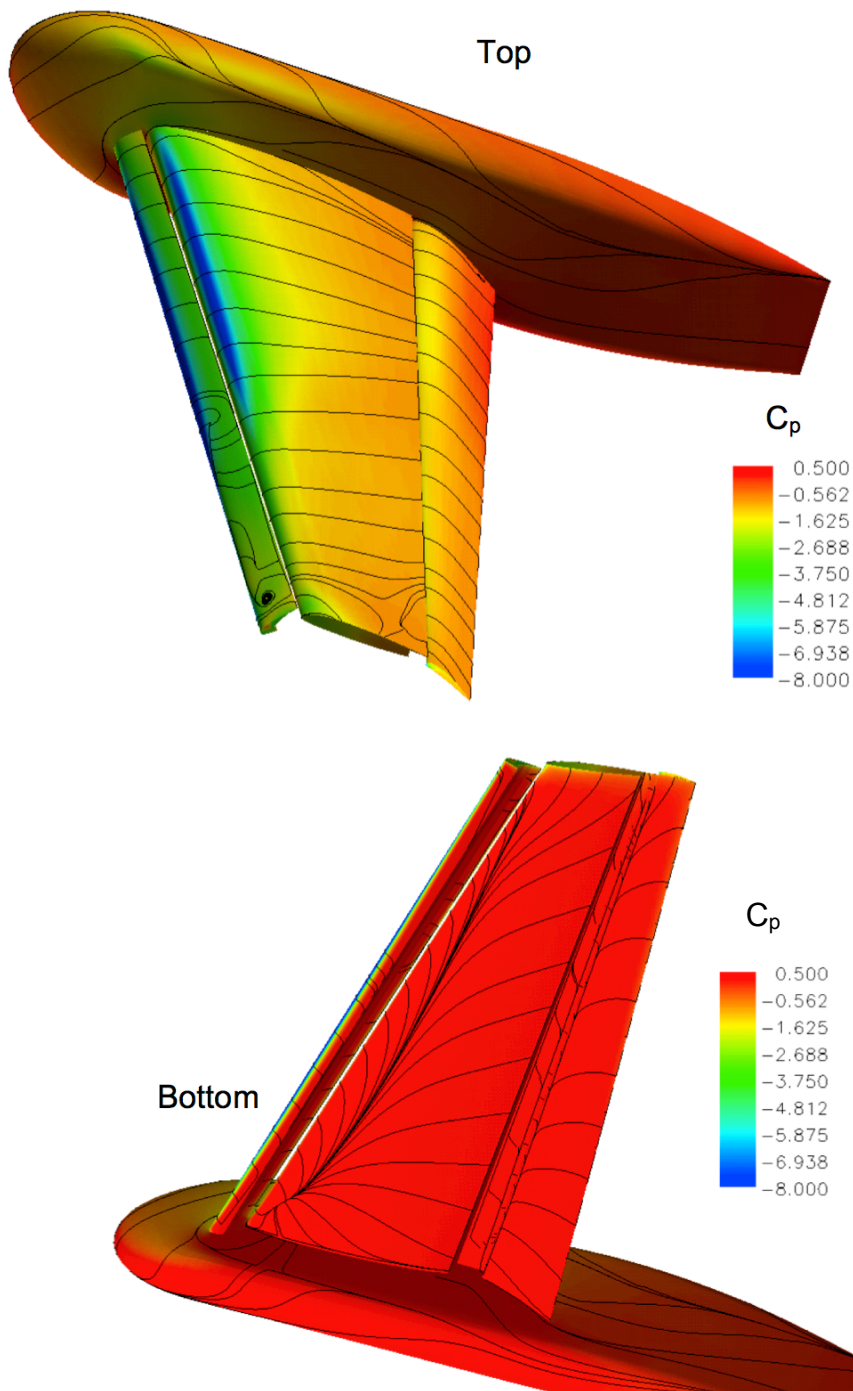


—  $\tilde{x} = 0.50$   
 - - -  $\tilde{x} = 0.85$



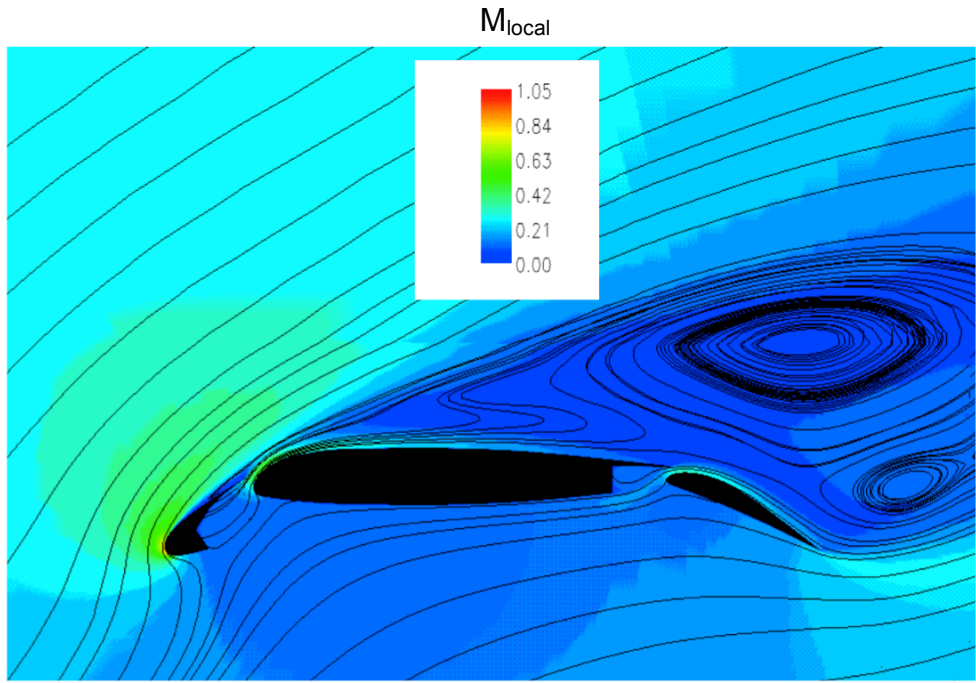
(d) Computed velocity profiles near the model surface at  $\eta = 0.70$ .

Figure 18. Concluded.

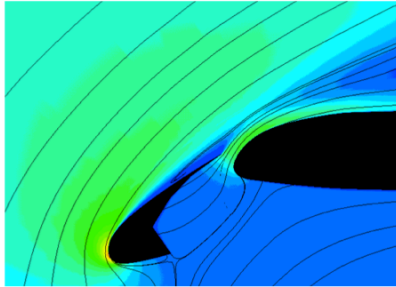


(a) Surface pressure-coefficient contours and constrained streamlines immediately above the surface.

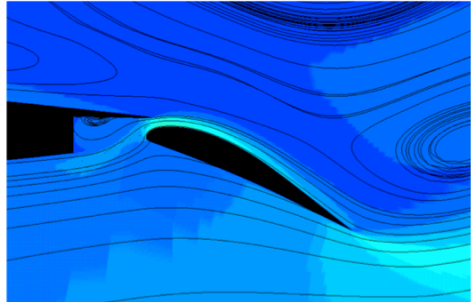
Figure 19. Model surface and flow-field parameters at  $\alpha = 34.858^\circ$ .  
(Spalart-Allmaras turbulence model)



Full wing



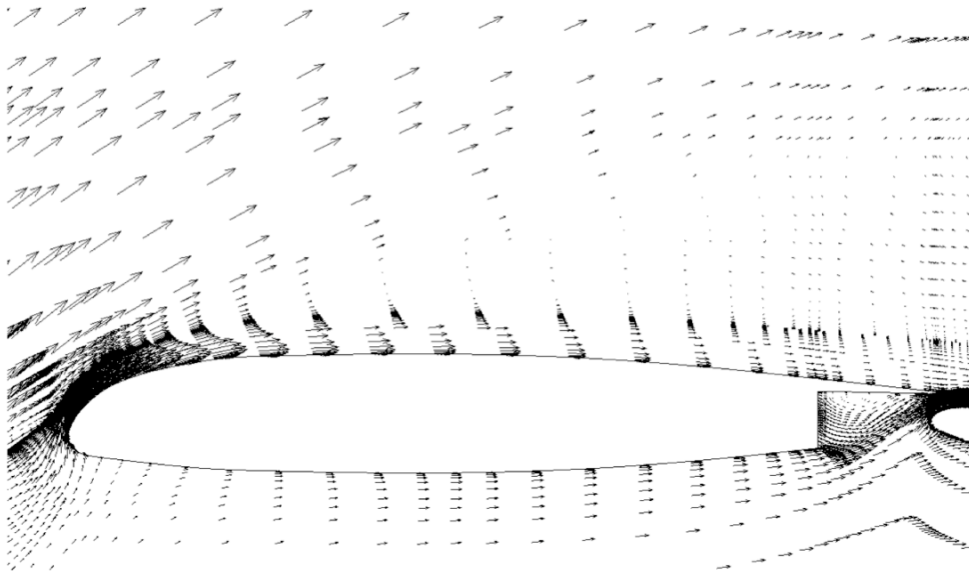
Leading edge region



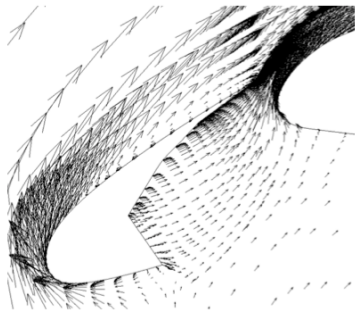
Trailing edge region

(b) Mach number contours and constrained streamline pattern for a stream-wise cut at  $\eta = 0.70$ .

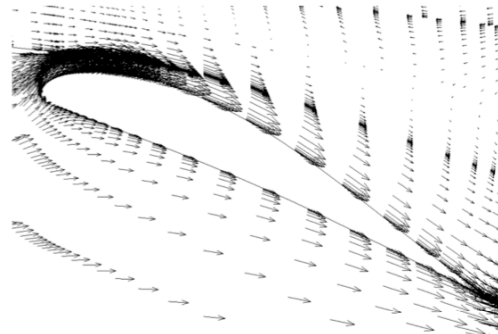
Figure 19. Continued.



Main wing element



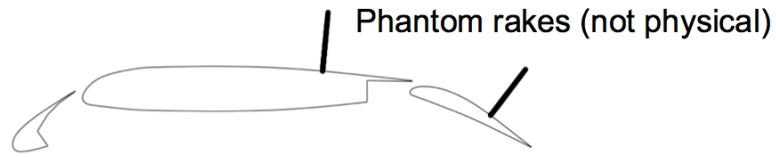
Leading edge region



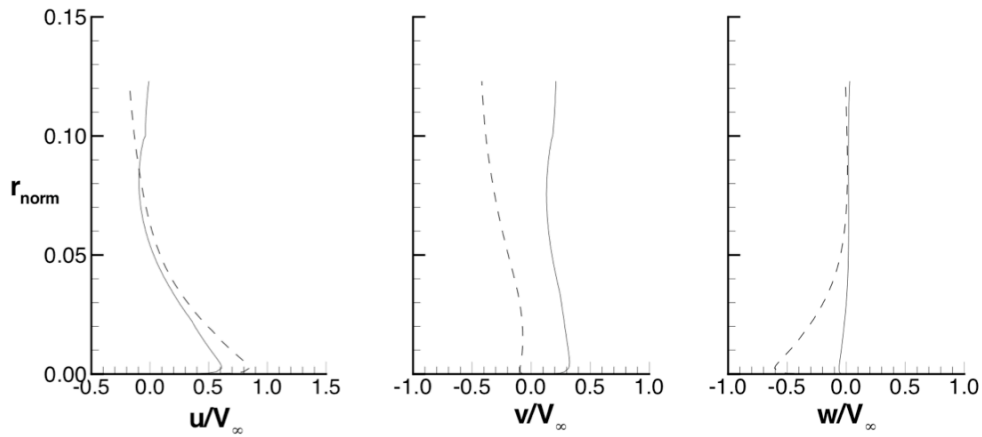
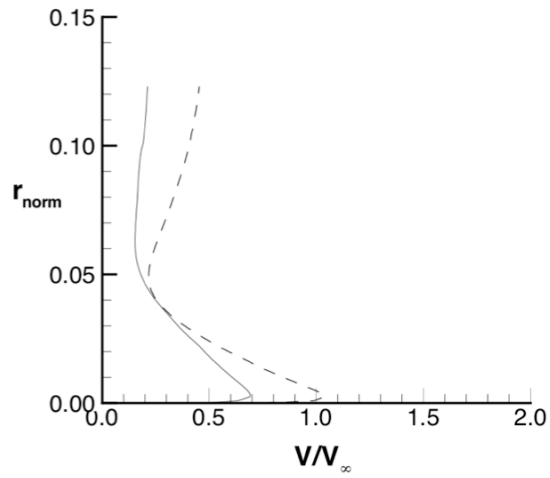
Flap

(c) Velocity vectors for a stream-wise cut at  $\eta = 0.70$ .

Figure 19. Continued.

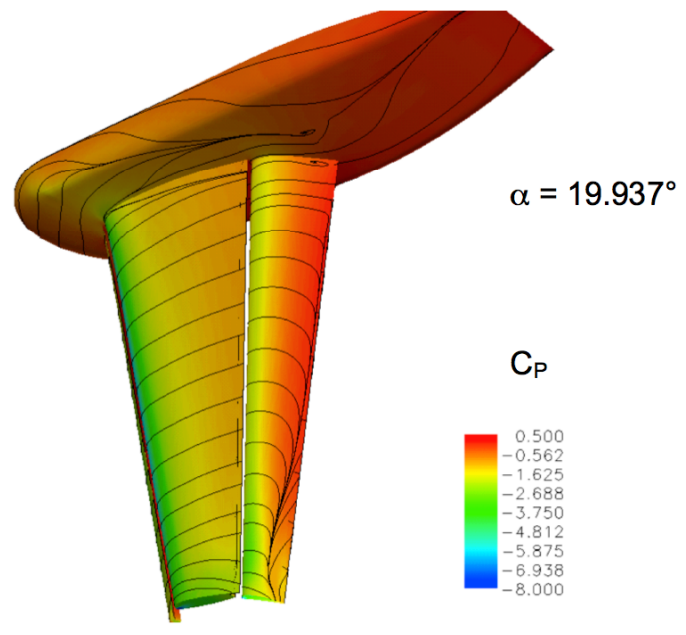
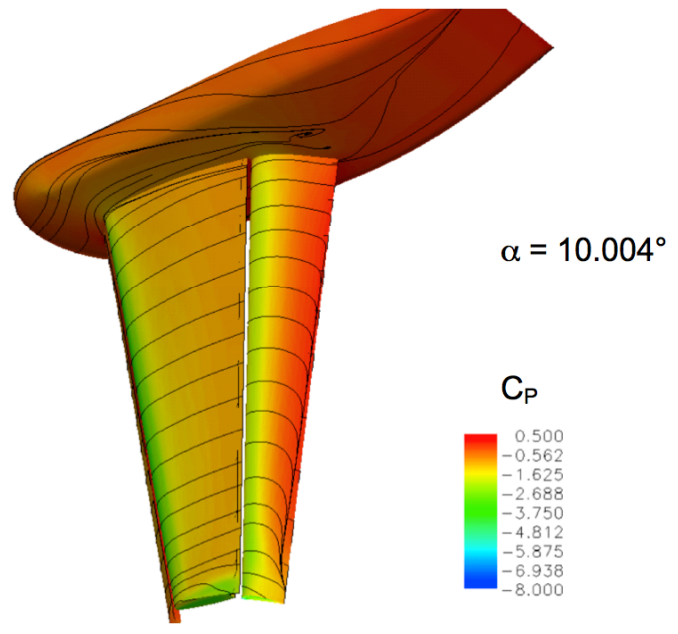


—  $\tilde{x} = 0.50$   
 - - -  $\tilde{x} = 0.85$



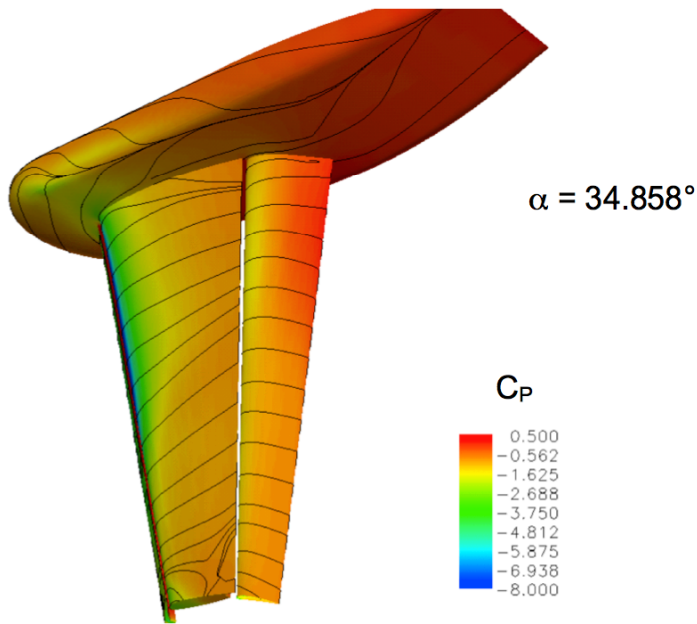
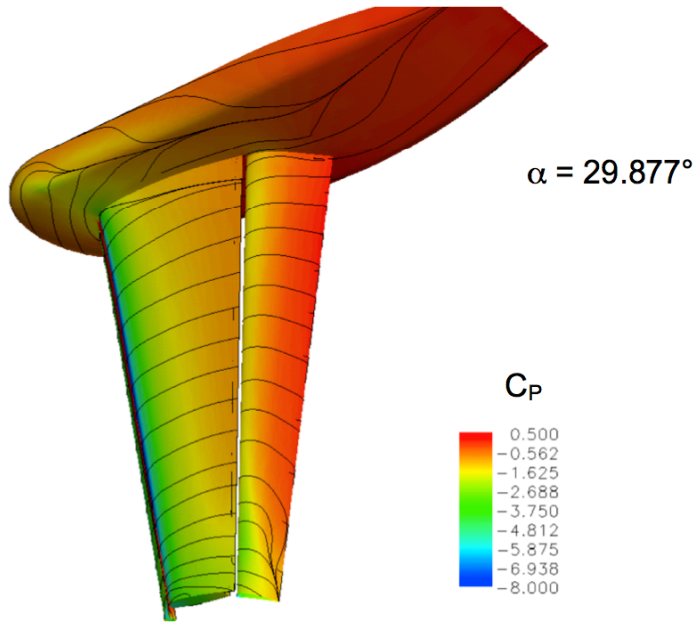
(d) Computed velocity profiles near the model surface at  $\eta = 0.70$ .

Figure 19. Concluded.



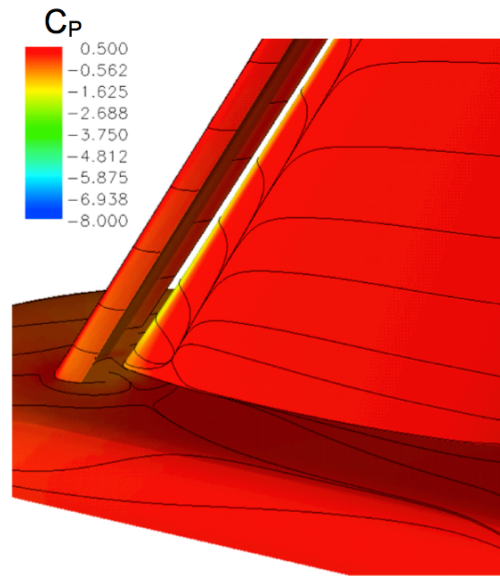
(a)  $\alpha = 10.004^\circ$  and  $19.937^\circ$

Figure 20. Effect of angle of attack on the trailing-edge flap.  
(Spalart-Allmaras turbulence model)

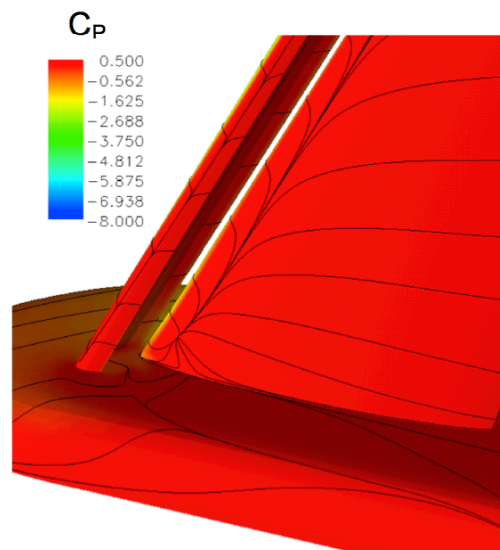


(b)  $\alpha = 29.877^\circ$  and  $34.858^\circ$

Figure 20. Concluded.



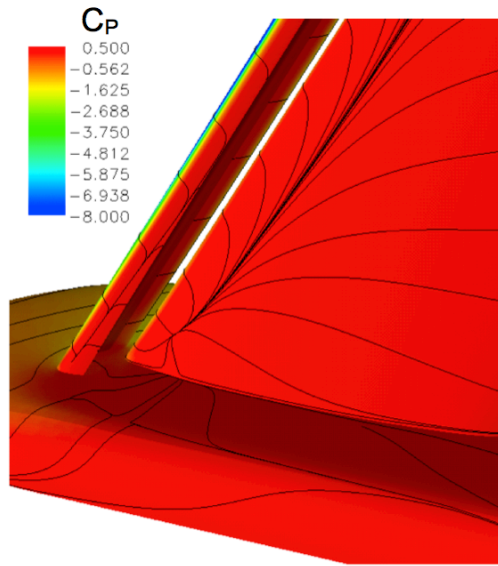
$\alpha = 10.004^\circ$



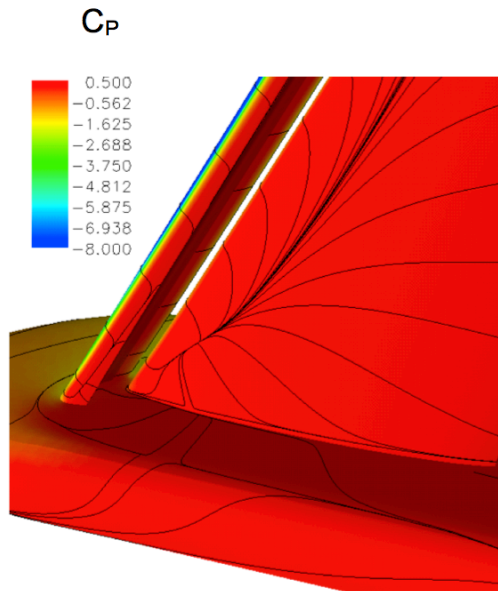
$\alpha = 19.937^\circ$

(a)  $\alpha = 10.004^\circ$  and  $19.937^\circ$

Figure 21. Effect of angle of attack at the juncture of the leading edge of the wing and the fuselage. (Spalart-Allmaras turbulence model)



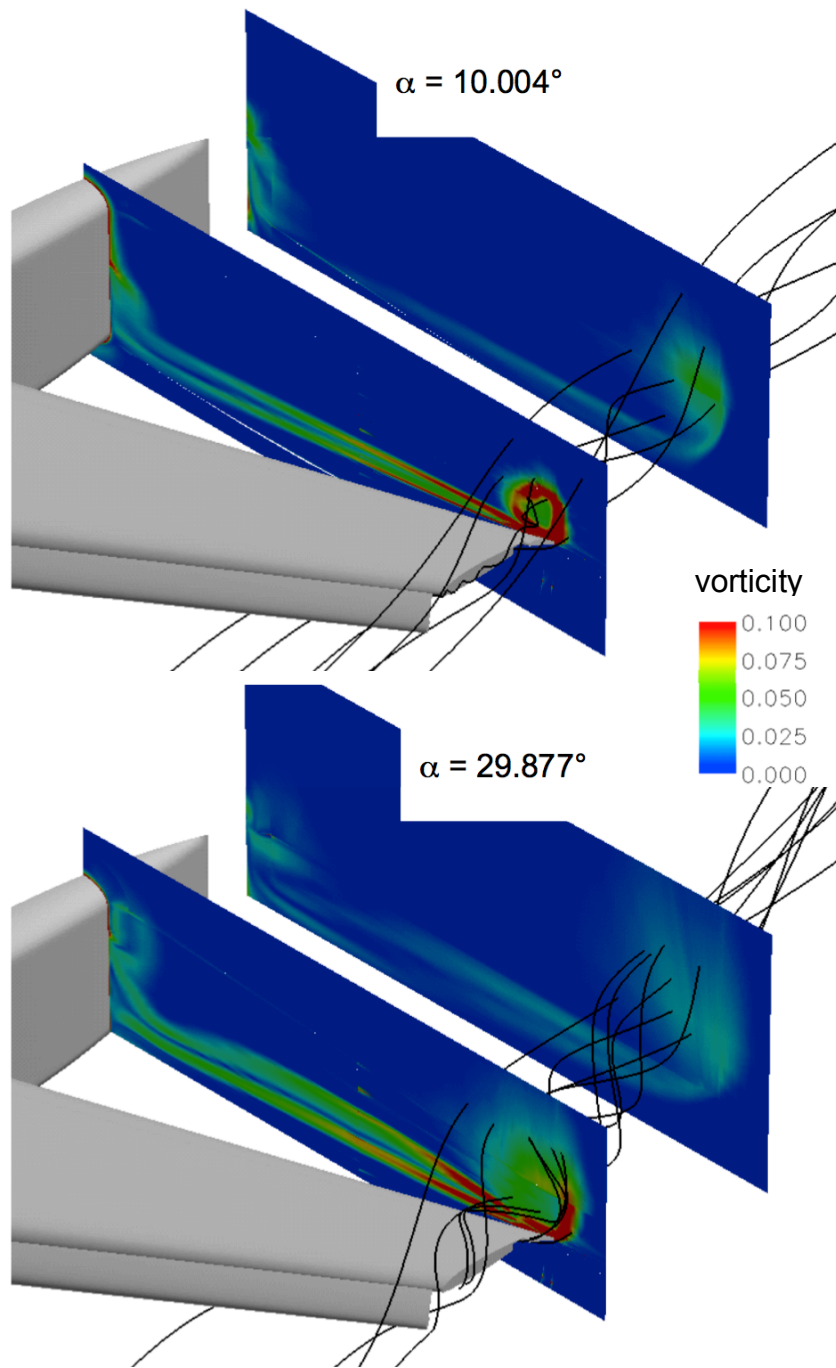
$\alpha = 29.877^\circ$



$\alpha = 34.858^\circ$

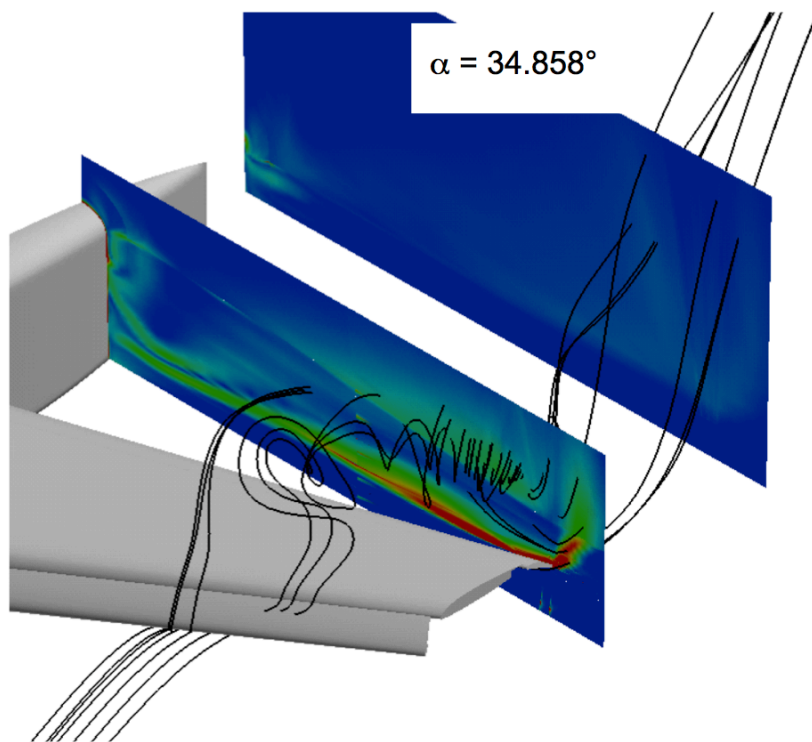
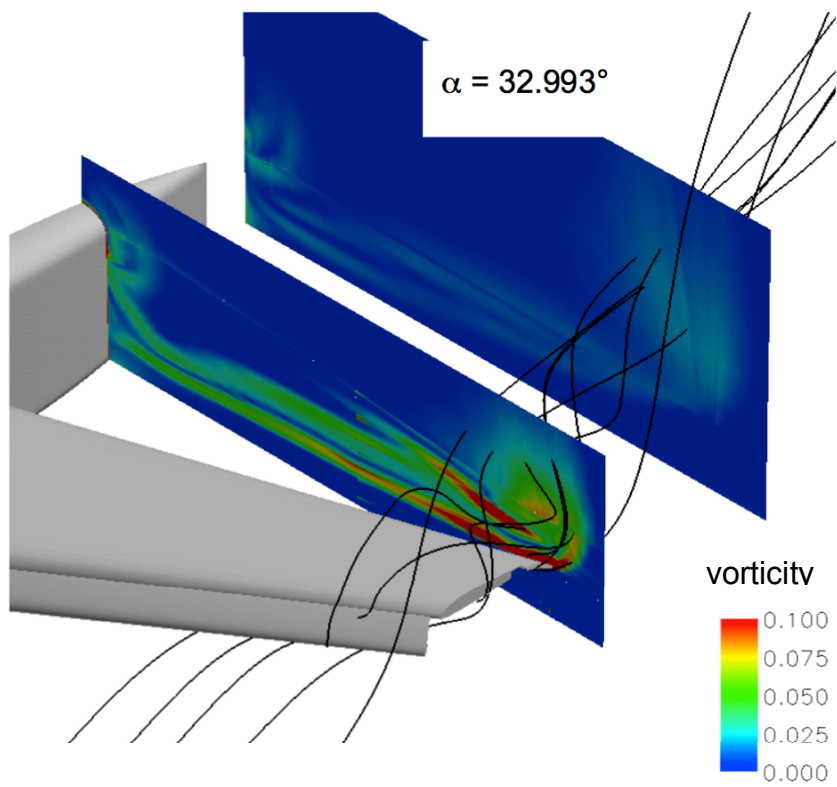
(b)  $\alpha = 29.877^\circ$  and  $34.858^\circ$

Figure 21. Concluded.



(a)  $\alpha = 10.004^\circ$  and  $29.877^\circ$

Figure 22. Effect of angle of attack on the wing tip vortices.  
(Spalart-Allmaras turbulence model)



(b)  $\alpha = 32.993^\circ$  and  $34.858^\circ$

Figure 22. Concluded.

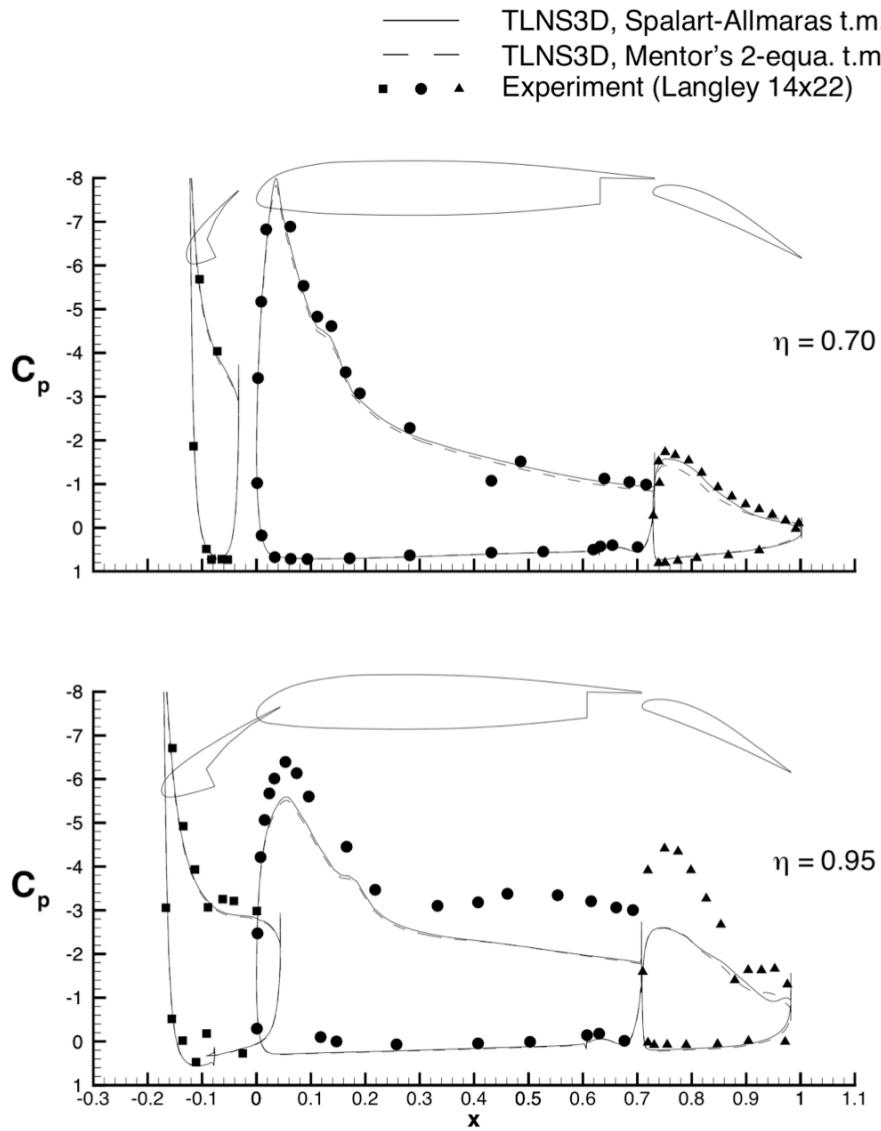
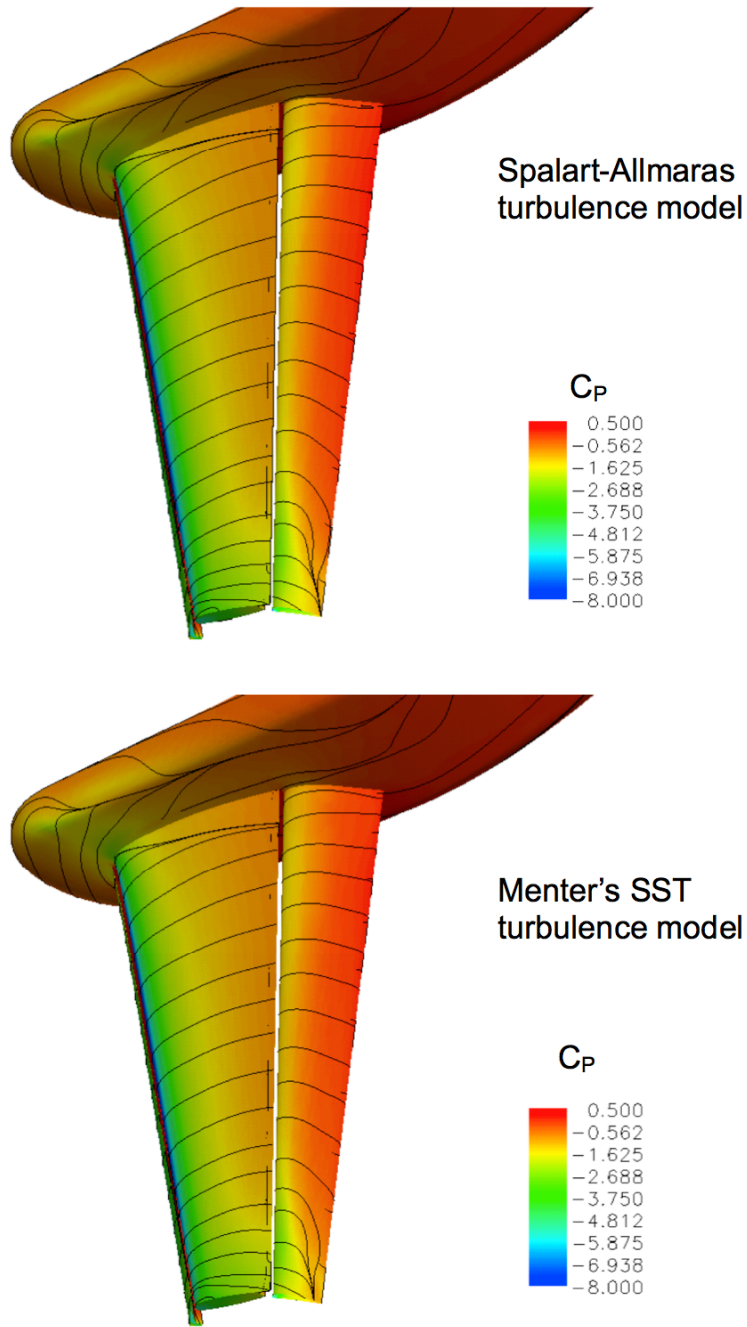
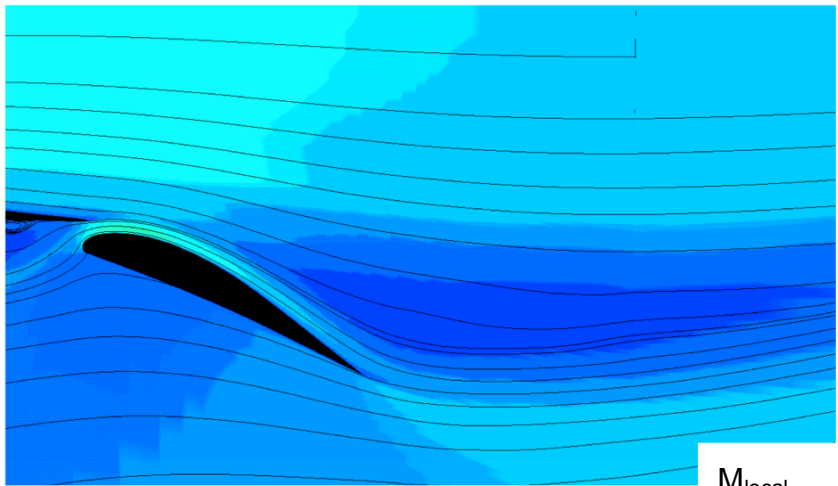


Figure 23. Effect of turbulence model on the wing pressure coefficients. ( $\alpha = 29.877^\circ$ )



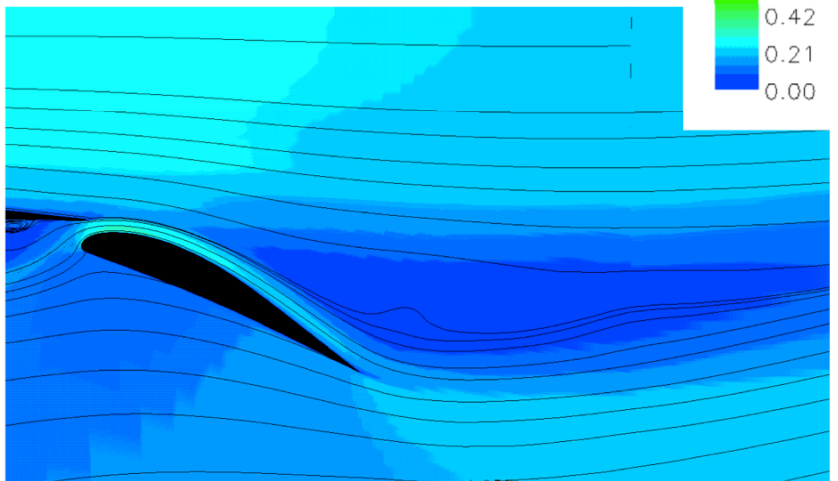
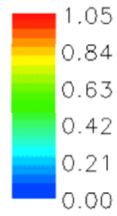
(a) Surface pressure-coefficient contours and constrained streamlines immediately above the surface.

Figure 24. Effect of the turbulence model on the flow field in the vicinity of the flap. ( $\alpha = 29.877^\circ$ )



Spalart-Allmaras turbulence model

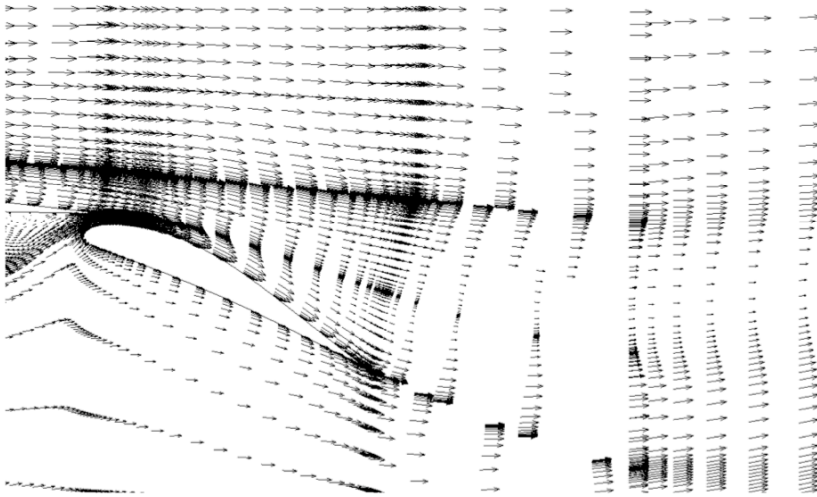
$M_{local}$



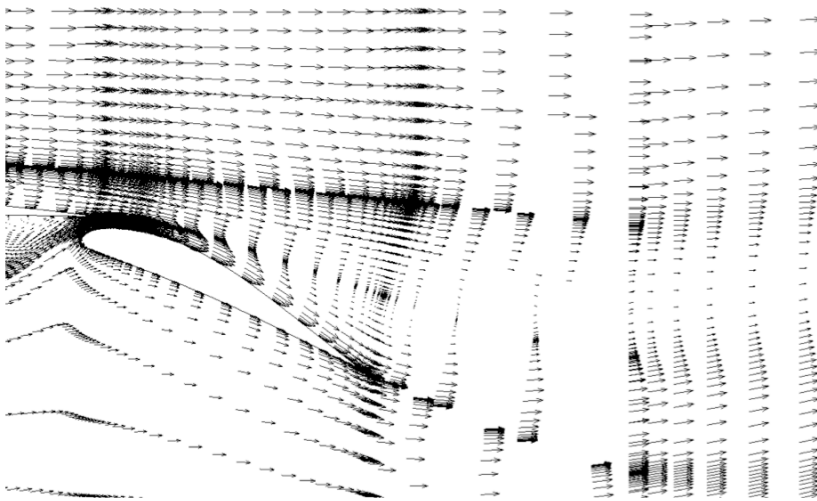
Menter's SST turbulence model

(b) Mach number contours and constrained streamlines for a stream-wise cut at  $\eta = 0.70$ .

Figure 24. Continued.



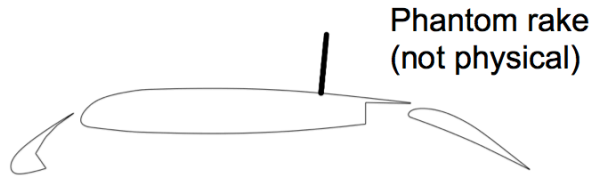
Spalart-Allmaras turbulence model



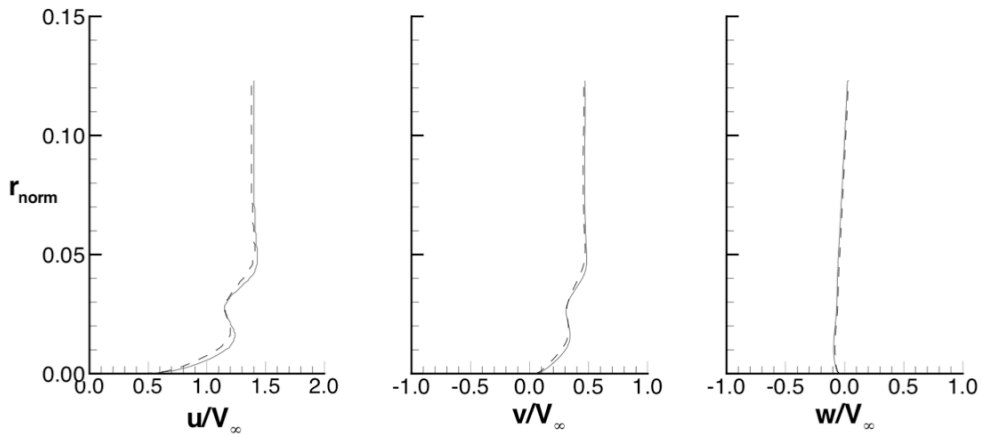
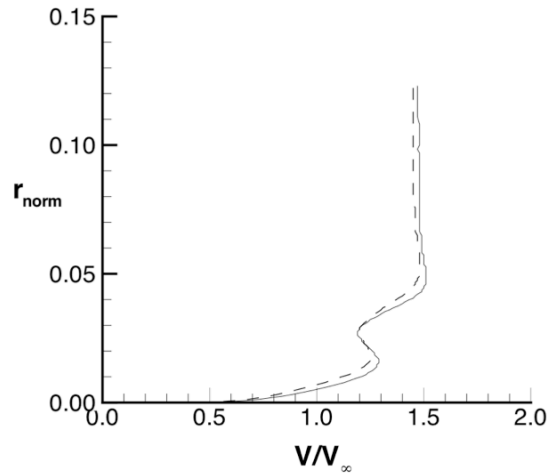
Menter's SST turbulence model

(c) Velocity vectors for a stream-wise cut at  $\eta = 0.70$

Figure 24. Concluded.

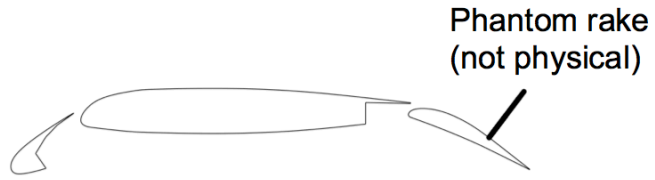


— Spalart – Allmaras turbulence model  
 - - - - - Menter's SST turbulence model

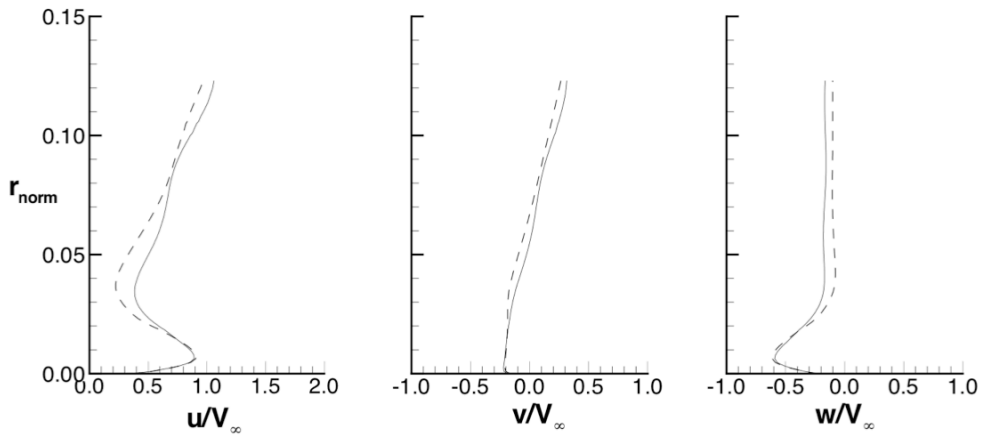
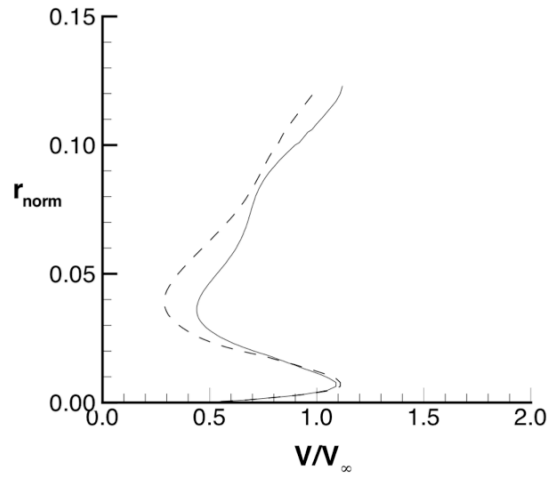


(a)  $\eta = 0.70$ ,  $\tilde{x} = 0.50$

Figure 25. Effect of the turbulence model on the velocity profiles near the wing surface. ( $\alpha = 29.877^\circ$ )

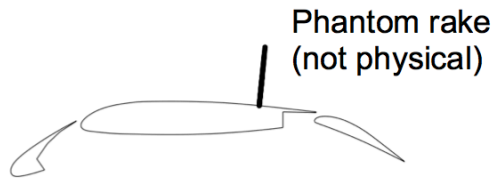


— Spalart – Allmaras turbulence model  
 - - - Menter's SST turbulence model

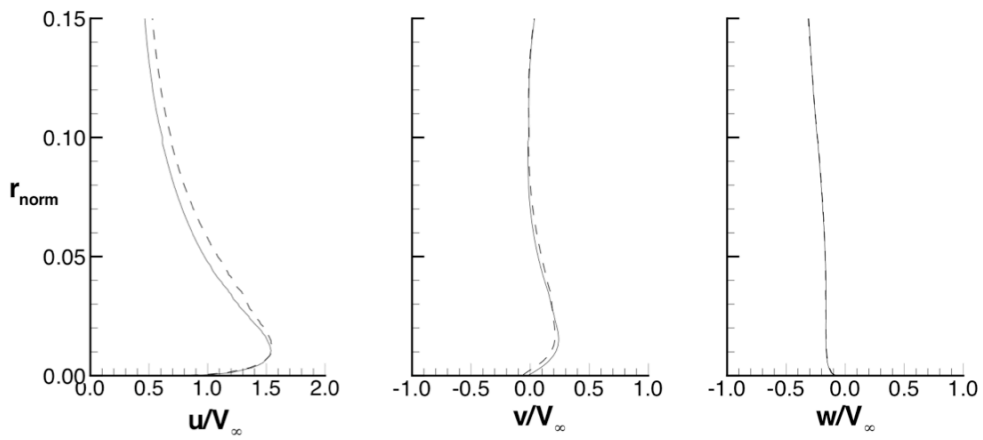
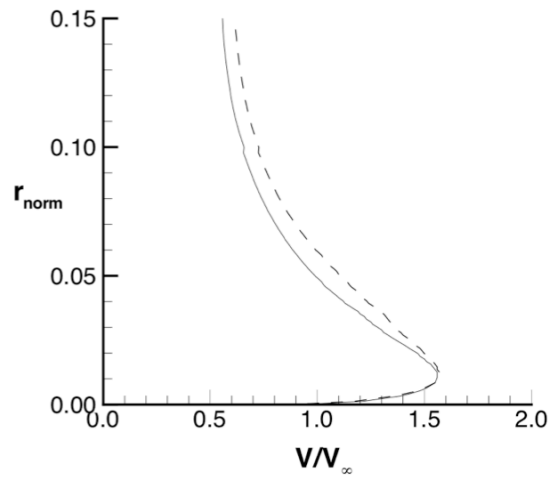


(b)  $\eta = 0.70, \tilde{x} = 0.85$

Figure 25. Continued.

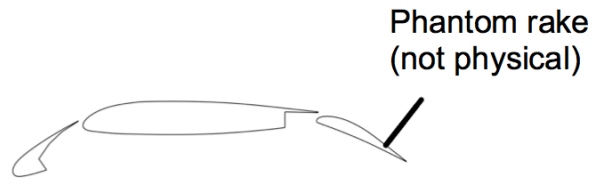


— Spalart – Allmaras turbulence model  
 - - - Menter's SST turbulence model

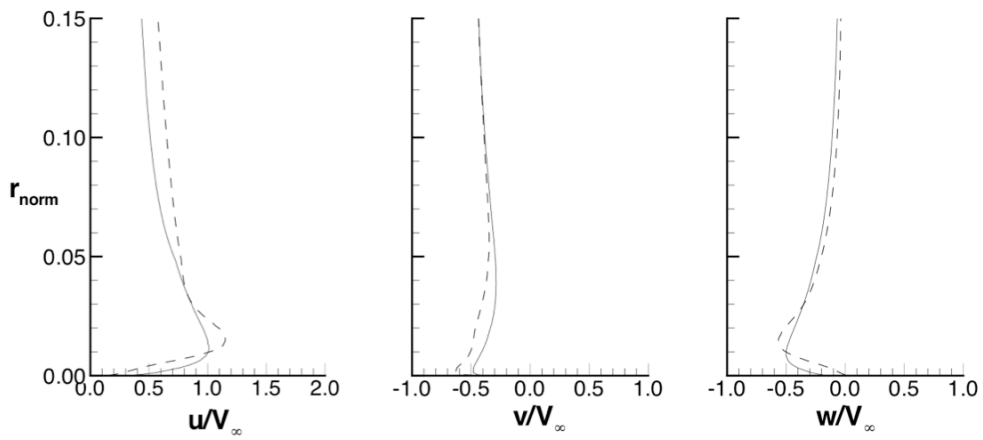
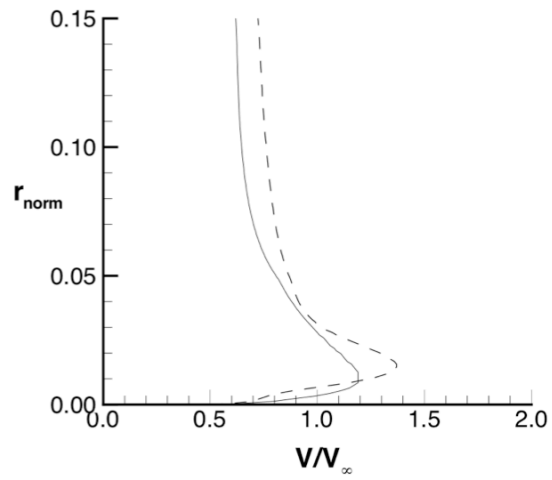


(c)  $\eta = 0.95$ ,  $\tilde{x} = 0.50$

Figure 25. Continued.



— Spalart – Allmaras turbulence model  
 - - - Menter's SST turbulence model



(d)  $\eta = 0.95$ ,  $\tilde{x} = 0.85$

Figure 25. Concluded.

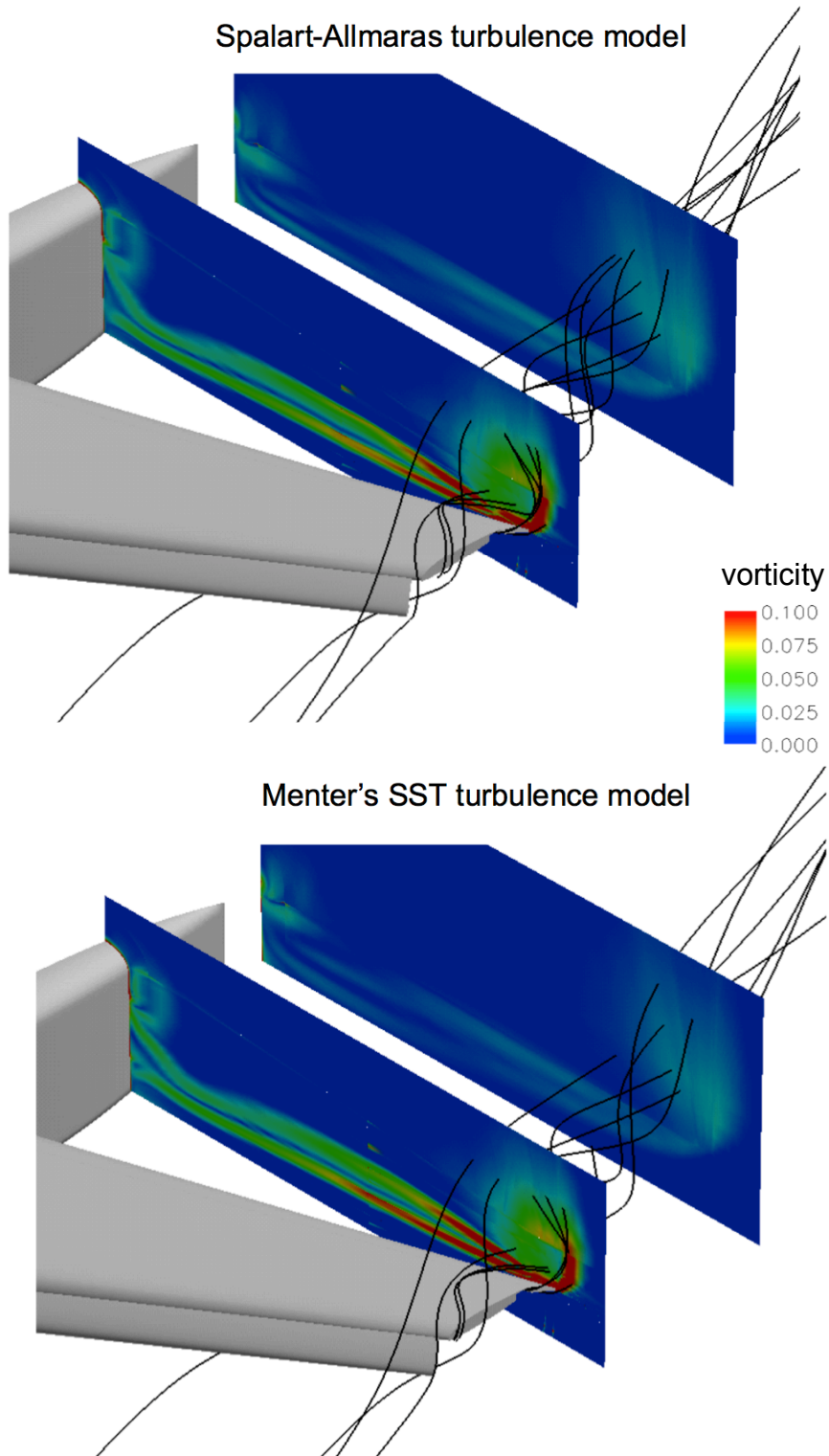


Figure 26. Effect of the turbulence model on the wing vortices. ( $\alpha = 29.877^\circ$ )

**REPORT DOCUMENTATION PAGE**

*Form Approved  
OMB No. 0704-0188*

The public reporting burden for this collection of information is estimated to average 1 hour per response, including the time for reviewing instructions, searching existing data sources, gathering and maintaining the data needed, and completing and reviewing the collection of information. Send comments regarding this burden estimate or any other aspect of this collection of information, including suggestions for reducing this burden, to Department of Defense, Washington Headquarters Services, Directorate for Information Operations and Reports (0704-0188), 1215 Jefferson Davis Highway, Suite 1204, Arlington, VA 22202-4302. Respondents should be aware that notwithstanding any other provision of law, no person shall be subject to any penalty for failing to comply with a collection of information if it does not display a currently valid OMB control number.  
**PLEASE DO NOT RETURN YOUR FORM TO THE ABOVE ADDRESS.**

<b>1. REPORT DATE (DD-MM-YYYY)</b> 01-02-2015		<b>2. REPORT TYPE</b> Technical Memorandum		<b>3. DATES COVERED (From - To)</b>	
<b>4. TITLE AND SUBTITLE</b>  Numerical Calculations of 3-D High-Lift Flows and Comparison With Experiment				<b>5a. CONTRACT NUMBER</b>	
				<b>5b. GRANT NUMBER</b>	
				<b>5c. PROGRAM ELEMENT NUMBER</b>	
				<b>5d. PROJECT NUMBER</b>	
				<b>5e. TASK NUMBER</b>	
<b>6. AUTHOR(S)</b>  Compton, William B., III				<b>5f. WORK UNIT NUMBER</b>	
<b>7. PERFORMING ORGANIZATION NAME(S) AND ADDRESS(ES)</b> NASA Langley Research Center Hampton, VA 23681-2199				<b>8. PERFORMING ORGANIZATION REPORT NUMBER</b>  L-20524	
<b>9. SPONSORING/MONITORING AGENCY NAME(S) AND ADDRESS(ES)</b> National Aeronautics and Space Administration Washington, DC 20546-0001				<b>10. SPONSOR/MONITOR'S ACRONYM(S)</b>  NASA	
				<b>11. SPONSOR/MONITOR'S REPORT NUMBER(S)</b>  NASA-TM-2015-218686	
<b>12. DISTRIBUTION/AVAILABILITY STATEMENT</b> Unclassified - Unlimited Subject Category 02 Availability: NASA STI Program (757) 864-9658					
<b>13. SUPPLEMENTARY NOTES</b>					
<b>14. ABSTRACT</b>  Solutions were obtained with the Navier-Stokes CFD code TLNS3D to predict the flow about The NASA Trapezoidal Wing, a high-lift wing composed of three elements: the main-wing element, a deployed leading-edge slat, and a deployed trailing-edge flap. Turbulence was modeled by the Spalart-Allmaras one-equation turbulence model. One case with massive separation was repeated using Menter's two-equation SST k-w turbulence model in an attempt to improve the agreement with experiment. The investigation was conducted at a free stream Mach number of 0.2, and at angles of attack ranging from 10.004° to 34.858°. The Reynolds number based on the mean aerodynamic chord of the wing was 4.3x10 <sup>6</sup> . Compared to experiment, the numerical procedure predicted the surface pressures very well at angles of attack in the linear range of the lift. However, computed maximum lift was 5% low. Drag was mainly under predicted. The procedure correctly predicted several well-known trends and features of high-lift flows, such as off-body separation. The two turbulence models yielded significantly different solutions for the repeated case.					
<b>15. SUBJECT TERMS</b>  Angle of attack; Computational fluid dynamics; High-Lift; Leading-edge slat; Navier-Stokes equations; Surface pressures; Trailing-edge flap; Trapezoidal wings; Turbulence models; Wings					
<b>16. SECURITY CLASSIFICATION OF:</b>			<b>17. LIMITATION OF ABSTRACT</b>	<b>18. NUMBER OF PAGES</b>	<b>19a. NAME OF RESPONSIBLE PERSON</b>
<b>a. REPORT</b>	<b>b. ABSTRACT</b>	<b>c. THIS PAGE</b>			STI Help Desk (email: help@sti.nasa.gov)
U	U	U	UU	124	<b>19b. TELEPHONE NUMBER (Include area code)</b>  (757) 864-9658